NASA CR-54675
HRL-6270S

SURFACE IONIZATION STUDIES ON REFRACTORY METALS AND METAL ALLOYS

by

O.K. HUSMANN

prepared for

NATIONAL AERONAUTICS AND SPACE ADMINISTRATION

CONTRACT NAS 3-6270

HUGHES RESEARCH LABORATORIES
A DIVISION OF HUGHES AIRCRAFT COMPANY
MALIBU, CALIFORNIA

Requests for copies of this report should be referred to

National Aeronautics and Space Administration
Office of Scientific and Technical Information
Attention: AFSS-A
Washington, D C. 20546

NASA CR-54675
HRL-6270S

SUMMARY REPORT

SURFACE IONIZATION STUDIES ON REFRACTORY METALS AND METAL ALLOYS

by

O. K. Husmann

prepared for

NATIONAL AERONAUTICS AND SPACE ADMINISTRATION

December 1966

CONTRACT NAS 3-6270

Technical Management
NASA Lewis Research Center
Cleveland, Ohio

HUGHES RESEARCH LABORATORIES
A Division of Hughes Aircraft Company
Malibu, California

TABLE OF CONTENTS

LIST OF ILLUSTRATIONS

SURFACE IONIZATION STUDIES ON REFRACTORY METALS AND METAL ALLOYS

by O. K. Husmann

Hughes Research Laboratories
Malibu, California

SUMMARY

The use of high work function refractory metals and metal alloys for improvement of the ionization efficiency is of particular importance in connection with long term contact ion engine operation. Critical temperatures for cesium surface ionization and thermionic work functions on polycrystalline solid iridium, rhenium, and four tungsten-rhenium alloys were investigated under this contract. The critical temperatures are expressed by the equation $T_C = A/(B - \log j)$, with T in degrees Kelvin and j in amperes per square centimeter. The equation constants A and B, the work functions, and Richardson constants A' (all at zero E-field) are given in Table I. The minimum work functions for the cesiated tungsten-25% rhenium, rhenium, and iridium filaments are 1.3 eV, 1.1 eV and 1.3 eV, respectively.

TABLE I

Summary of Critical Temperature and Work Function Data

Material	A	B	ϕ, eV	A', A/deg2 cm2
Tungsten	14000	8.764	4.54	120
Tungsten-5% rhenium	13800	8.52	4.55	120
Tungsten-7% rhenium	13900	8.53	4.56	120
Tungsten-15% rhenium	13810	8.30	4.58	120
Tungsten-25% rhenium	14000	8.32	4.695	146
Rhenium	14910	8.59	4.88	164
Iridium	16810	9.1	5.40	140

The spectral emissivities of tungsten-25% rhenium and iridium at 1500°K and at 6650 Å are **0.44** and **0.33.** A guard ring diode was employed in these experiments. The temperature gradient of the filament inside the center electrode was less than 3°K; temperatures were pyrometer calibrated. Surface and bulk contaminants were removed by heating to temperatures exceeding 2300°K.

Ion microscope studies on clean porous tungsten yielded surface migration lengths on the order of 2 μ (emission center radius). Consequently the optimum pore density for tungsten is about 10^7 pores/cm^2 (by traverse technique). At pore densities of 2×10^6 pores/cm^2 and with 10 mA/cm^2 cesium ion current density, the neutral efflux, measured with the tungsten-25% rhenium alloy, is 2%. Under the same conditions it is 1%for rhenium and 1.5%for the iridium coated surface. The iridium was chemically deposited on a porous tungsten substrate.* Its work function was originally **4.8** eV; during the investigation it decreased to **4.7** eV. While these neutral fraction data are consistent with the measured work functions, they are not necessarily as low as can be obtained with these materials. Rhenium also was chemically deposited onto a tungsten substrate (of low pore density). Even though a somewhat lower work function has been measured here than that of the clean rhenium filament (**4.69** eV versus **4.88** eV), the neutral efflux is considerably lower than that measured with the same pore density on clean tungsten. This is expected, because the Saha equation predicts a strong dependence of the neutral efflux on the work function. Both neutral efflux and threshold temperature for cesium surface ionization reflect the low substrate pore density.

*This **work** was conducted under Contract NAS 3-6272.

SECTION I

INTRODUCTION

The use of high work function refractory metals and metal alloys to improve the ionization efficiency is particularly important in connection with long term contact ion engine operation, In the case of excessive neutral efflux, charge exchange ions sputter erode the accelerator and decel electrodes. Deterioration of the critical electrode geometries contributes to further erosion and breakdown of the propulsion unit. Increasing threshold temperature with the work function, as generally observed, is a less important factor; with increased ionization efficiency, the current density can also be increased.

For the solid metal, with alkali deposition from the vapor phase, the neutral efflux F is expressed by the Saha equation

$$F = \left[1 + 1/2 \exp \frac{e(\phi - I)}{kT} \right]^{-1}$$

with ϕ the work function and I the ionization potential, It was shown earlier' that porous rhenium yields a lower neutral efflux than porous tungsten of the same pore density. The refractory metals included in this investigation were chosen because of their high work function (polycrystalline surface) and high melting point; the latter is important in connection with the sintering characteristics. Consequently, platinum, for example, is not included here. Pure iridium is fairly soft and therefore a tungsten substrate with iridium coating was investigated. Iridium work functions are reported between 5.3 and 5.4 eV. According to Hayden and Brophy[2] the addition of iridium to tungsten improves the sintering stability of porous tungsten, but the small addition of a metal such as iridium may not necessarily result in a greatly increased work function.[3] According to the phase diagrams, the solid solution range for

most additives to tungsten does not exceed a few weight percent. An exception is rhenium. Tungsten-rhenium alloys with 5%, 7%, 15%, and 25% rhenium have been investigated in filament form; based on the good results of the tungsten-25% rhenium alloy (in connection with work function and threshold temperature), a porous pellet sintered from prealloyed tungsten-25% rhenium was investigated in connection with neutral efflux. For completeness, tungsten and rhenium filaments were also investigated.

All refractory metals and metal alloys were first investigated in filament form, considering electron work function and threshold temperature for surface ionization in an all metal guard ring diode with directly heated wire. The system was evacuated during baking by a mercury diffusion pump and after pinch-off by a 0.2 liter/sec ion pump. Vacuum in the low 10^{-8} Torr and 10^{-9} Torr range was maintained, and in this pressure range the ion pump did not interfere with the work function measurements. During critical temperature readings, the tube was not pumped. The filament, with uniform temperature in the central electrode section, was pyrometer calibrated. At 1500°K, the spectral emissivity of W-25% Re is close to that of rhenium, as measured by comparison with black body conditions. The measured spectral emissivity of polished iridium is in good agreement with data published by D. L, Goldwater and W. E. Danforth[4]; at the above temperature it is *0.33*. For the remaining tungsten-rhenium alloys, spectral emissivities interpolated between those of tungsten and rhenium were used.

In the beginning, Richardson plots usually yield high work function, and A exceeds 120 $A/deg^2\ cm^2$. The tungsten-rhenium alloys were cleaned up at high temperatures, in the 2600°K range. The filament resistance of the tungsten-rhenium alloys remained constant even with high temperature operation over extended periods of time. This is in contrast to the iridium and molybdenum filaments, which showed an appreciable increase in resistance because of material evaporation.

Although several iridium filaments were investigated, it was possible with only one of them to reach the published work function of 5.4 eV. Two filaments yielded a work function of 5.2 eV, while another one yielded only 5.0 eV. An analysis of the iridium filaments indicated that rhodium is the major contaminant. For its removal from the bulk, rhodium must diffuse to the filament surface and evaporate. Both processes are enhanced with increasing filament temperature. However, application of high temperature to the iridium filament is limited because of its high vapor pressure.' At reduced temperatures, cleanup is very slow. This explains why the published work function of 5.4 eV was reached with only one of the iridium filaments.

In agreement with Chaikovskii,[5] hysteresis bas been observed on the clean solid surfaces, with constant hysteresis width at a given ion current density, independent of the scanning speed. The hysteresis width decreases with increasing ion current density. Threshold temperature data given here belong to the high temperature slope and agree with T_c measured on the porous metal at ion current densities below about 1 mA/cm^2. In contrast to the solid metal, no hysteresis has been observed on the clean porous metal and metal alloys in the ion current density range between 0.1 and 10 mA/cm^2

The electric field E at the filament was in the range of a few kilovolts per centimeter, to avoid the Schottky effect,. with

$$E = U/(r \ln R/r)$$

and

$$dQ_i = (e^3 E)^{1/2}$$

The decrease in threshold temperature because of the E-field is related to the Frenkel equation

$$\tau = \tau_o \exp Q/kT$$

with

$$-dT = \left\{\left[1/2\,(T_1 \; t \; T_2)\right]^2 - dQ_i/Q_i(T_1 \times T_2)\right\}^{1/2} - 1/2\,(T_1 \times T_2) \quad .$$

For polycrystalline tungsten, the decrease in critical temperature at 10^4 V/cm is 10^{o}K.

Spectral analysis of the cesium used revealed only two alkalies (potassium and sodium) among the contaminants detected. The concentrations of all contaminants were in the low ppm range. The sodium vapor pressure is too low to affect cesium surface ionization data. The potassium vapor pressure is about 20% of the cesium vapor pressure under saturation conditions. With the small amount of potassium present, its vapor pressure was not saturated. Therefore, the threshold temperatures are correctly those of cesium.

For neutral efflux measurements, the iridium was chemically deposited onto a 2.4 μ spherical tungsten coat which was sintered on a Philips-Metalonics Mod E porous tungsten substrate. The work function of the iridium coated pellet first was 4.8 eV, decreasing to 4.7 eV during the neutral efflux measurements. The neutral efflux at 10 mA/cm^2 was 2%, and the critical temperatures exceed those measured on a fully oxygenated tungsten surface. The thermionic work function of the W-25% Re pellet was 4.64 eV, with A = 350 A/deg^2 cm^2, lower than that of the W-25% Re filament. At 0.1 mA/cm^2 the threshold temperature for this pellet was somewhat below that of the solid alloy; however, it exceeded the solid W-25% Re cesium threshold temperature with increasing ion current density. The neutral efflux at 10 mA/cm^2 was measured to be 3.5%. These data are consistent with the thermionic work function values measured on the pellets tested.

It should be emphasized that high work function surface ionizers will show considerable improvement in ionization efficiency over tungsten and consequently will improve the ion engine lifetime. For example, clean W-25% Re surfaces with pore densities (by the traverse technique) exceeding 2 x 10^6 pores/cm^2 should show a neutral efflux less than 2% at a cesium ion current density of 10 mA/cm^2; a lower neutral efflux is

expected for the clean surface of the iridium coated porous emitter. Both rhenium and iridium yield a lower neutral efflux than the W-25% Re alloy, but have a higher threshold temperature.

The results of Task IV (Ionizer Evaluation) and Task V (Engine Electrode Simulation Experiments) will be reported in the Summary Report on Contract NAS 3-6271; this policy was continued throughout the contract period because of the direct relationship of this subject to that contract effort.

SECTION II

IMPROVED SURFACE IONIZATION EFFICIENCY BY USE OF HIGH WORK FUNCTION REFRACTORY METALS AND METAL ALLOYS

A. INTRODUCTION

In order to establish the connection between the phase diagram and the emission properties of the'tungsten-rhenium alloys, electron work functions and critical temperatures for surface ionization were measured with cesium, The tungsten-rhenium alloys with a rhenium content below 26 wt. % are particularly interesting because of the solid solubility range of rhenium in tungsten up to 26 wt,%, and also because of the high melting point of these alloys. This high melting point is of interest in connection with the sintering characteristic and the cleanup of the bulk material and the surface from any contaminant.

The alloy filaments with 5%, 7%, 15%, and 25% rhenium in tungsten are available commercially. Originally we planned to investigate various other high temperature refractory metal alloys, but the tungsten-osmium and tungsten-iridium alloys were not available. Tungsten-10% tantalum (by weight) alloy was finally received from an outside vendor in the form of a single crystal with a 1/4 in. diameter It was impossible to draw wire from this single crystal, according to D. L. Keller.[6] Prior to drawing, this single crystal was molybdenum-enveloped; the assembly was then swaged in a hydrcgen atmosphere at 2550°F. During working, however, the alloy became fibrous and fragmented into many small pieces.

Alkali surface ionization on a variety of refractory metals has been reviewed extensively.[7-9] For efficient surface ionization, high work function substrates are particularly important. The ionization efficiency is expressed by the Saha-Langmuir equation, with

$$\beta = \left\{ 1 + 2 \exp \left[- (\phi - I) 11600/T \right] \right\}^{-1} \qquad (1)$$

Here ϕ is the work function, I is the ionization potential, and T is the emitter temperature.

Contaminants from the residual gas atmosphere and those diffusing from the bulk of the substrate may cause considerable changes in both work function and threshold temperature for surface ionization. Therefore, the data reported here, were obtained under clean surface conditions on the polycrystalline surface. For completeness, data measured on tungsten, rhenium, iridium, and molybdenum were added,

Critical temperatures for cesium surface ionization on tungsten were reported earlier by Taylor and Langmuir,[10] and these data (see Fig. 18 of Ref, 10) were extrapolated by Nottingham[11] to the 10 mA/cm^2 ion current density range; this is in contrast to measurements by Zandberg, et al.[12] Nottingham's extrapolation is in excellent agreement with our own data in this current density range, as measured on solid tungsten. G. F. Smith[13] published the thermionic work functions for a number of single crystal tungsten surfaces,[14] Rhenium work functions have been reported by a number of investigators.[15,16] According to our data, ϕ is 4, 88 eV €or the polycrystalline surface, which is in good agreement with both publications. Critical temperatures for cesium on porous rhenium were previously reported by Husmann[1] and Stavisskii, et al.[17] The secondary electron emission from tungsten-rhenium alloys was reported by Dyubua, et al,[18]

B. CRITICAL TEMPERATURES FOR SURFACE IONIZATION

The Frenkel equation relates the critical temperature for surface ionization with the ion desorption energy.

$$\tau = \tau_0 \exp Q_i/kT \qquad (2)$$

and with

$$j = e\theta\sigma_o/\tau_i \quad , \tag{3}$$

it follows that

$$Q_i = (k/e)(T_2 \times T_1/T_2 - T_1)(\ln j_2/j_1 - \ln \theta_2/\theta_1) \tag{4}$$

with $T_2 > T_1$, the critical temperature for j_2 or j_1, with j in amperes per square centimeter. θ is the surface coverage with regard to a monolayer, and σ_o is the maximum number of atoms adsorbed per square centimeter. Q_i is the ion desorption energy in electron volts.[19] The τ_i are the average surface lifetimes of the adsorbed atoms (or ions). With eq. (4) it is possible to compute the critical temperatures for surface ionization, if the ion desorption energy and the surface coverage are known. The critical temperature equation is of the general form:

$$T_c = A/(B - \log j) \tag{5}$$

In general, it is difficult to evaluate the surface coverage 8; therefore, Levine, et al.,[20] approached this problem by taking into account the sublimation energy and the dipole moment of the adsorbed atoms and ions (see also Razor and Warner[21]). The Levine-Gyftopoulos approach yields for cesium on tungsten anion desorption energy close to that published by Husmann[19] (on polycrystalline tungsten), however for rhenium, for example, the computed 1.62 eV ion desorption energy is far below the measured value of 2.2 eV[19] (see also Garvin, et al.[22]). In contrast to the measured electron work functions of the tungsten-rhenium alloys, in the range of up to W-25% Re the Levine-Gyftopoulos approach" predicts a work function exceeding that of pure rhenium. According to their work function measurements

on tungsten-hafnium alloys,[3] Dyubua, et al., found a noncontinuous change with increasing hafnium in tungsten. The maximum work function which they report is connected with the W_2Hf phase.

C. EXPERIMENTAL SETUP

A guard ring diode was employed in the experiments reported here; the electrodes rested on an all stainless steel 4 in. base plate (see Fig. 1). To avoid temperature gradients, the tube was made of stainless steel with the outside copper clad and with a window for the pyrometer readings. Tube and flange are sealed with copper gaskets. The diode outer electrode material is nickel. All electrodes, as well as the filament, are supported by Al_2O_3 ceramic bushings. During the experiments in cesium atmosphere, the 4 in. flange (including the bushings, ion pump, and cesium reservoir) is maintained at temperatures more than 100°C higher than those of the tube in order to avoid cesium condensation on critical surfaces. Insulator bypass currents under this condition were below any critical level.

Prior to ion pump operation, the tube was evacuated by a mercury-diffusion pump backed by a mechanical pump, with a zeolite trap between the pumps to avoid back-streaming hydrocarbons. The complete tube was baked for about 12 hours at temperatures in the 300°C range (with the magnet of the ion pump off) at pressures in the low 10^{-6} Torr range. Finally, after cooling to room temperature, the tube was disconnected from the pump stand and further evacuated with the ion pump (0.2 liter/sec). The final pressures were in the 10^{-9} Torr range. Before the cesium capsule was opened, the filament was degassed and the thermionic work function was measured. For tungsten, rhenium, and the tungsten-rhenium alloys, the filament cleanup temperature was in the 2600°K range. The iridium filament was handled at temperatures not exceeding 2200°K. Except for the iridium filament (which produced some deposits), no change in filament resistance was observed. It should be mentioned that the originally hard iridium filament became quite soft after heat treatment. All filaments were heat treated until the electron work function stabilized.

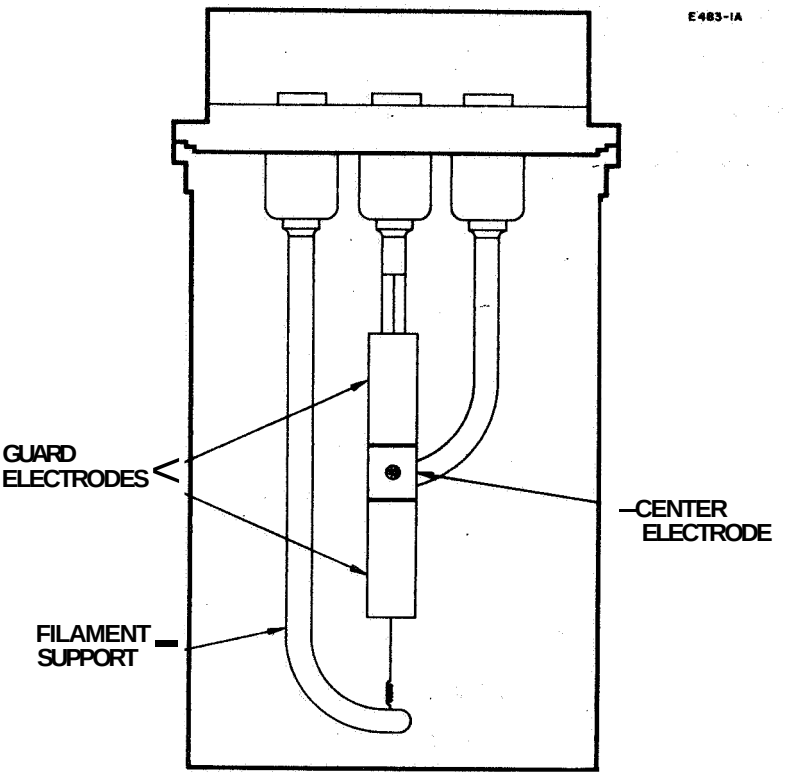

Fig. 1. Refractory metal and metal alloy testing tube.

The most interesting of these alloys, the W-25% Re alloy, was investigated at temperatures in the 2000°K range for more than a month after cleanup. The filament cleanup usually took more than 4 days (Fig. 2). If the filament seemed to contain small amounts of contaminants, such as carbon,[23] air in the 10^{-5} Torr pressure range was admitted to remove the carbon in the form of CO and CO_2. At 1500°K temperatures the solid solution of carbon in tungsten is negligible,[23] and only 0.5 atomic percent carbon in tungsten has been reported at 2400°K (Fig. 3). However, carbon combines easily with tungsten; Andrews[24] has shown that the carbon in tungsten evaporates at temperatures above 2450°C. To avoid filament evaporation, such high temperatures were not maintained here, and oxygen was admitted as an alternative cleanup technique.[25-26] Oxygen is easily desorbed from tungsten at temperatures exceeding 1800°K (Ref. 27) and from rhenium and the tungsten-rhenium alloys for certain temperatures in the 2600°K range.

The filament flashing technique was applied to test for gas adsorption from the residual gas atmosphere. The filament was operated at 1000°K for some time, and then suddenly flashed to above 2000°K. No gas desorption was indicated in this experiment, For this reason, we can assume that no oxygen was present. However, when the filament was maintained at room temperature for some time, gas desorption was observed. Hydrogen, CO, CO_2, and N_2 absorb only in the low temperature range, and their sticking probability at elevated temperatures is close to zero.[26]

Prior to the experiments, all filaments were checked spectroscopically; the contaminants detected are shown in Table II. The contaminants of the iridium and molybdenum filaments are included. The spectroscopic analysis is only semiquantitative. It is difficult to separate small amounts of rhodium from iridium.[28] The analysis provided by the iridium filament supplier describes 0.5% contaminants, mainly rhodium, in contrast to our spectral analysis. The vapor pressure of

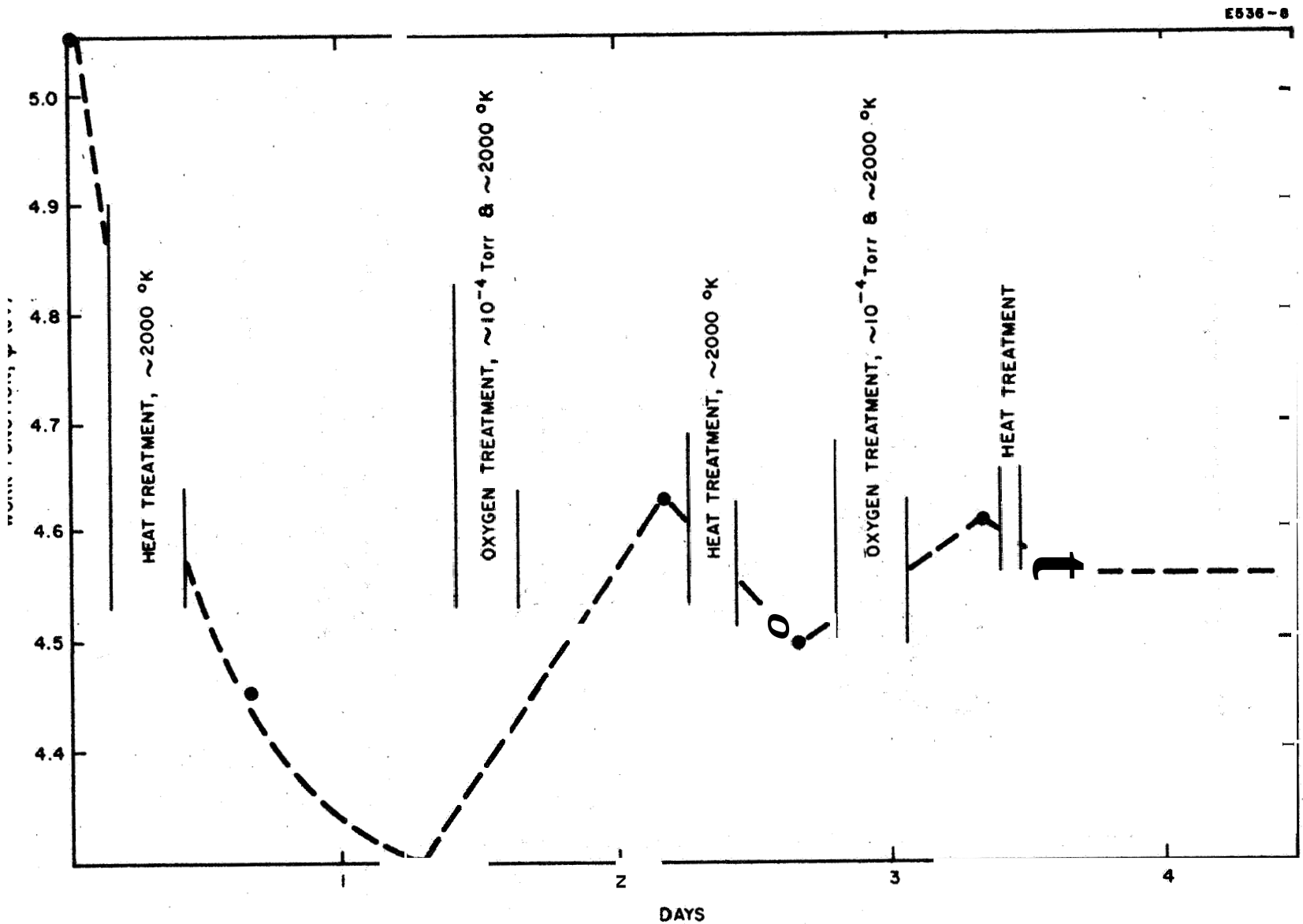

Fig. 2. Cleanup schedule for W-5% Re filament.

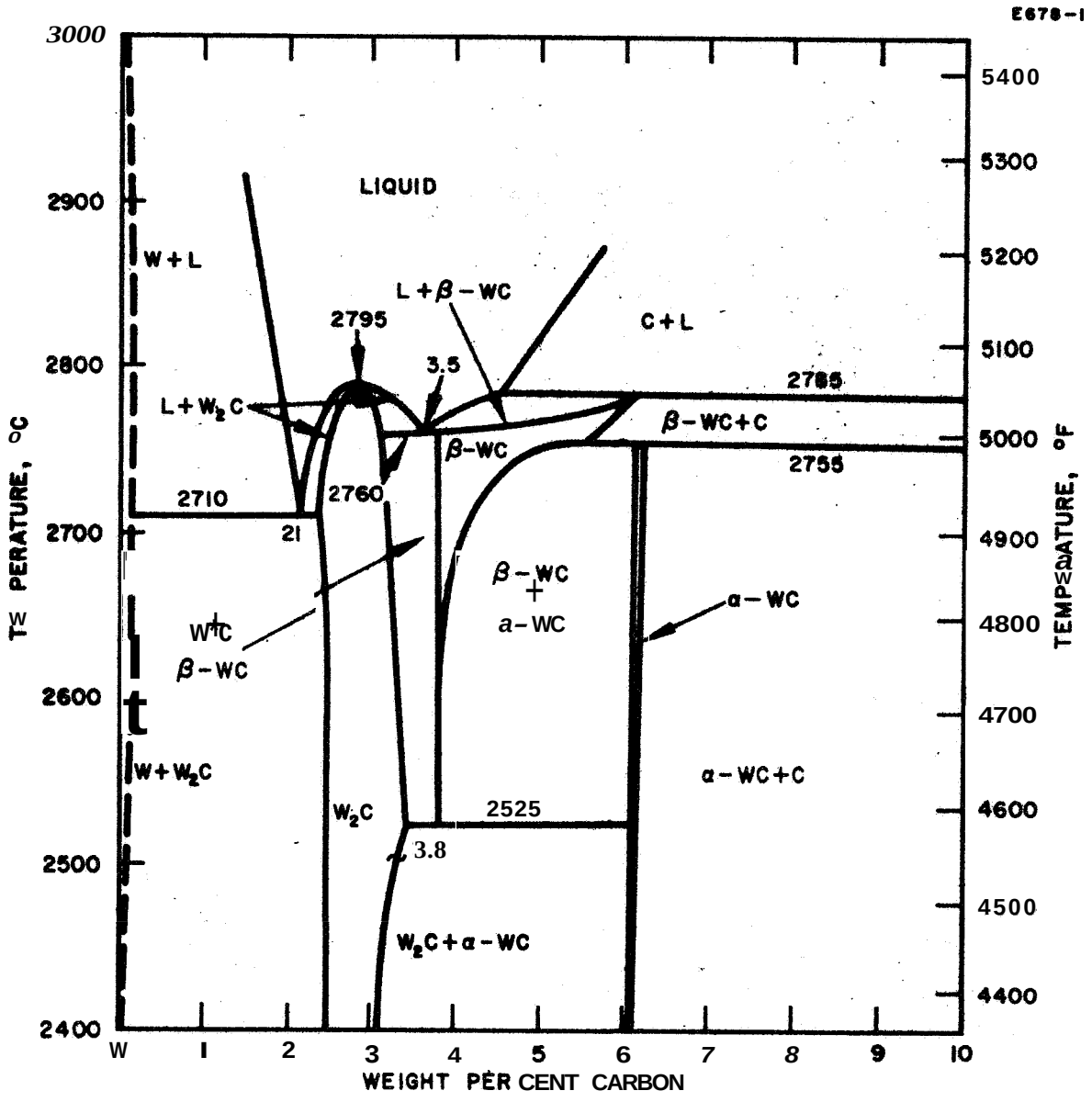

Fig. 3. Tungsten-carbon phase diagram.

TABLE II

Results of Spectroscopic Analysis of Tungsten-Rhenium Alloys

Element Detected	Alloy Tested						
	W-5% Re	W-7% Re	W-10% Re	W-15% Re	W-26% Re	Iridium	Molybdenum
Tungsten	Remainder	Remainder	Remainder	Remainder	Remainder		
Iridium						Remainder	
Rhenium	5.0%	5.7%	11 %	13. %	24. %	nil	
Silicon	0.018	0.040	0.032	0.030	0.026	0.012	trace
Magnesium	0.0014	0.00092	0.0011	0.00063	0.00092		trace
Iron	0.0089	0.020	0.014	0.012	0.017	0.0053	0.12
Molybdenum	nil	nil	trace, less than 0.02	0.11	nil	nil	Remainder
Copper	0.0015	0.0013	0.00077	0.0020	0.00083	0.00048	trace
Calcium	0.0034	0.0031	0.0040	0.0022	0.0033		nil
Chromium	nil	trace, less than 0.001	nil	nil	nil	nil	nil
Other Elements	nil	nil	nil	[illegible]	nil	nil	nil

rhodium exceeds that of iridium by several orders of magnitude (rhodium vapor pressure of 10^{-5} Torr is reached at 1681°K, while iridium has the same vapor pressure at 1993°K), therefore rhodium may evaporate at elevated temperatures. At temperatures above 700°C, iridium oxidizes somewhat in air and forms a high vapor pressure oxide. Rhodium is less affected by oxygen. To reduce traces of carbon, the iridium filament was heated at atmospheric pressure in air to about 700°C.[29]

D. FILAMENT TEMPERATURE MEASUREMENT

The filament temperature was measured with a micropyrometer in the temperature range between 1000 and 2200°K. Inside the 1/2 in. long central electrode the temperature gradient was less than 3°K, the error limit of the pyrometer. Spectral emissivity and glass window corrections have been applied. The spectral emissivities of tungsten, rhenium, and molybdenum are well known; those for the W-25% Re alloy and for iridium have been measured by comparison with black body radiation (Fig. 4). At 1500°K, the spectral emissivity of iridium (highly polished) is 0.33 (measured at 6650 Å, in good agreement with Goldwater, et al.[4]). The spectral emissivity is strongly dependent on the surface roughness and is 0.49 at 1300°K for the highly polished surface of the W-25% Re alloy. Figure 5 shows the heater power input versus temperature for the W-25% Re filament.

For determination of the cesiated W-25% Re surface minimum work function, temperature measurement below 1000°K is important. The preferred measuring technique in this temperature range is by thermocouple. However, thermocouple wire diameters are no smaller than 1 mil, and it is quite evident that a thermocouple of this dimension attached to a 2 to 7 mil filament changes the filament temperature distribution by heat conduction. Therefore, thermocouples could not be used. Use of the filament resistance change for temperature determination is also questionable because of the steep and changing temperature

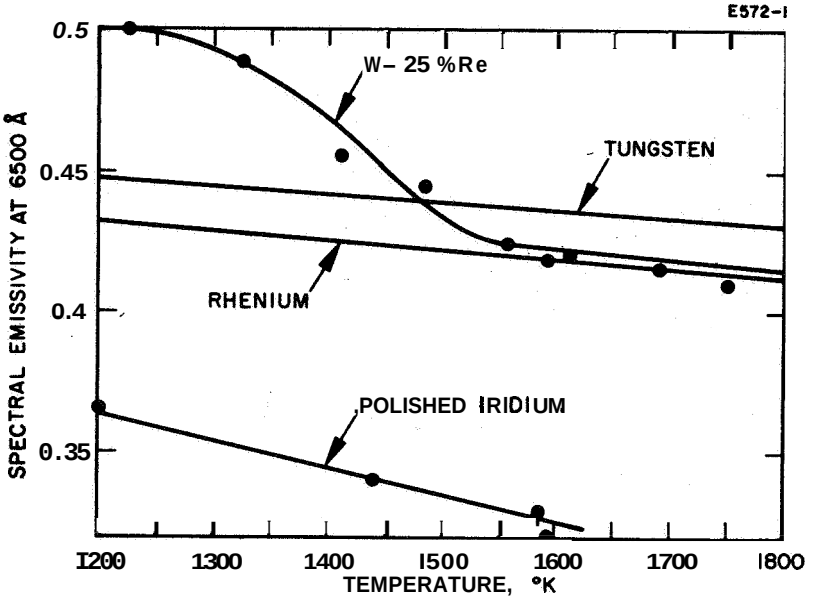

Fig. 4. Spectral emissivities of tungsten, rhenium, W-25% Re, and iridium at 6500 Å.

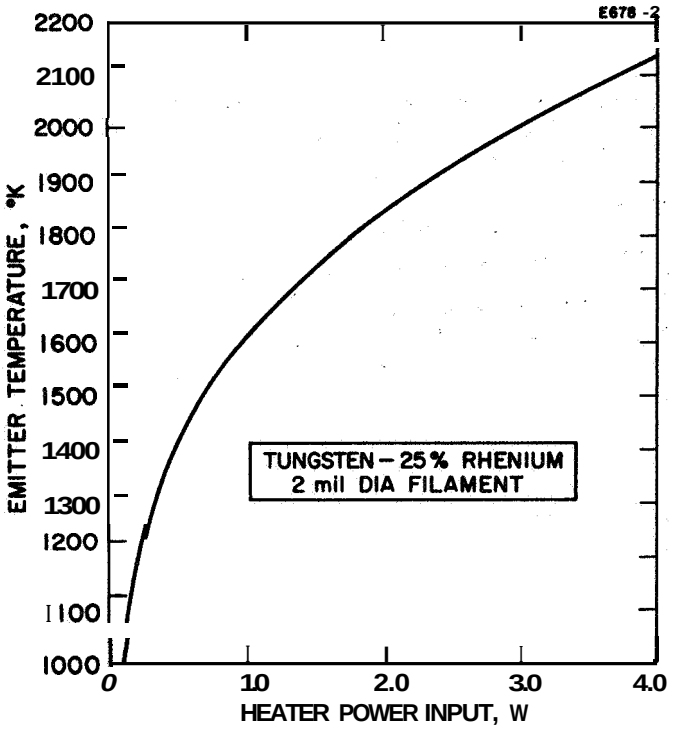

Fig. 5. Heater power versus temperature for the W-25% Re filament.

gradient at the filament ends. To insure the best possible temperature measurement below 1000°K, micropyrometer calibration above 1000°K was carefully established and extrapolated then toward 300°K.

In all of our experiments, the filament was dc heated. With dc heating, electromigration takes place; even after recrystallization, more different crystal planes are participating in the electron emission than would be expected with ac heating (in contrast to the single crystal development).[30] The effect of electromigration should not be intermixed with the shingle structure, as reported by Nichols.[31]

Electron work functions have been measured prior to admittance of cesium, and during and after the experiments with cesium. To reduce the cesium influence on the work function measurement in the low temperature range, the tube was cooled with LN_2 during these readings.

In the low pressure range employed here, the influence of the ion pump discharge current on the electron and ion currents was below the sensitivity of the ammeter, as checked with and without ion pump operation. The ion pump influences the readings only at pressures exceeding 5×10^{-7} Torr a pressure range far above that used. It may be emphasized that the ion pump was shut off during the threshold temperature readings and during the minimum work function measurements on the cesiated W-25% Re alloy, rhcniumand iridium. No noticeable pressure increase was detected during ion pump shutoff. The 0.2 liter/sec ion pump again operated without trouble after the cesium vapor pressure was down on the 7 scale.

E. THERMIONIC WORK FUNCTION

The electron work function of the refractory metals and metal alloys was measured by thermal electron emission in connection with the Richardson equation

$$j = (1 - r)(4 \pi m_e k2/h3)\, T2 \exp(- e/kT)\, \phi(T_o - \alpha T) \qquad (6)$$

with

$$A' = (4 \pi m_e k^2/h^3) = 120.3\ A/deg^2\ cm^2 \ . \qquad (7)$$

r is the electron reflection coefficient, as measured by the depletion of electrons in the low energy range of the Maxwellian distribution. For metals, the contribution of r is small. m_e is the electron mass, k the Boltzrnann constant, h the Planck constant, T the emitter temperature, and e the electron charge in coulombs. a is the temperature coefficient of the work function, as measured by change of the contact potential in a diode structure. If (with both electrodes clean) the anode temperature is changed, a small potential should develop because the Fermi level changes with increasing temperature (see Fig. 6). In Fig. 6 the electron potential between two different but connected metals is shown. The shaded areas define the Fermi level.

If it is assumed that the average temperature coefficient of the work function can be derived from the Richardson constant, as computed from the Richardson plot and its relation to the theoretical constant **A** of eq. (7), we have as an example for the W-25% Re alloy

$$a = 2 \times 10^{-5} \times T$$

$$\phi_e = \phi_R + aT \qquad (8)$$

and

$$\phi_e = 4.69 \text{ eV}$$

Here ϕ_e is the effective work function, **A** = 120.3, ϕ_R is the Richardson work function,[32] and T is in degrees Kelvin.

With an external electric field the Schottky effect must be considered; the Richardson equation is then

$$J = J_{E=0} \exp e(eE)^{1/2}/kT \quad A/cm2 \qquad (9)$$

The electric field E at the filament is

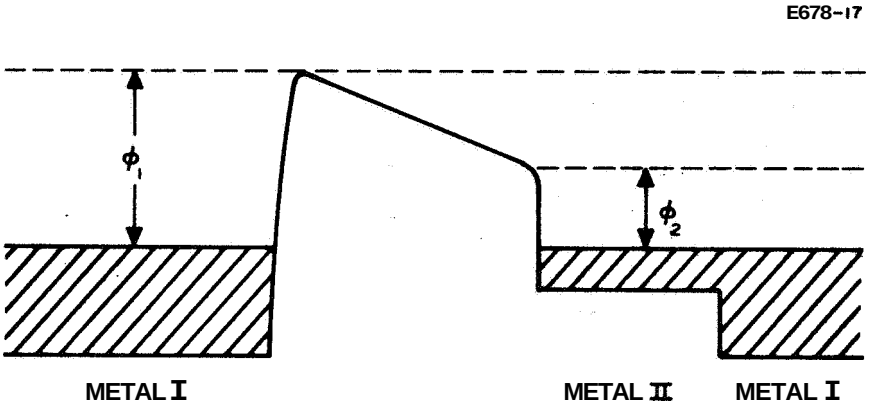

Fig. 6. Potential between two connected conductors with the work function ϕ_1 and ϕ_2.

$$E = U/(r \ln R/r) \qquad V\ cm^{-1} \tag{10}$$

where r is the filament radius in centimeters and R is the radius of the outer electrode. U is the applied voltage. In Fig. 7, E is given with the filament radius as a parameter. In connection with the electric field consideration, the perveance of the guard ring diode is of interest and is expressed by (see Fig. 8)

$$p = i/U^{3/2} \qquad A/V^{3/2}\ , \tag{11}$$

with the measured electron perveance

$$p_e = 2.28 \times 10^{-5} \qquad A/V^{3/2}$$

and the cesium ion perveance

$$p_i = 4.74 \times 10^{-8} \qquad A/V^{3/2}$$

for a 50 μ diameter filament, 1.17 cm anode radius, and 1/2 in. center electrode length. Extraction potentials of a few volts are sufficient for electron current densities of 10 mA/cm. In connection with the above dimensions the electric field at the filament is about 250 V/cm; this field reduces the thermionic work function by 3.1×10^{-3} eV, well inside the error limit of the reported work function data (see also Fig. 9). Measurement of the Schottky plot up to 10 kV/cm yielded a straight line with log j versus $E^{1/2}$. Consequently, no attention has been paid to the patch effect (see Fig. 10). All electron currents have been measured with 7.5 V extraction potential.

The electron and ion currents were measured with a calibrated Keithley 600 A electrometer amplifier instrument. To confirm these data, in a few cases another Keithley 600 A instrument was used to take the

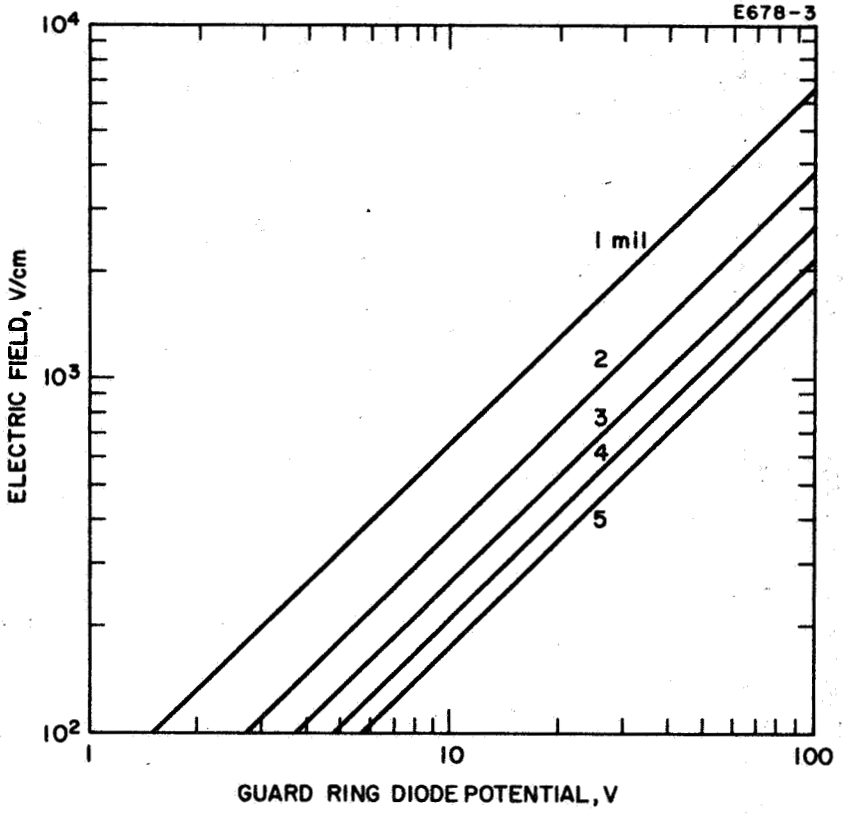

Fig. 7. Electric field as a function of guard ring diode potential.

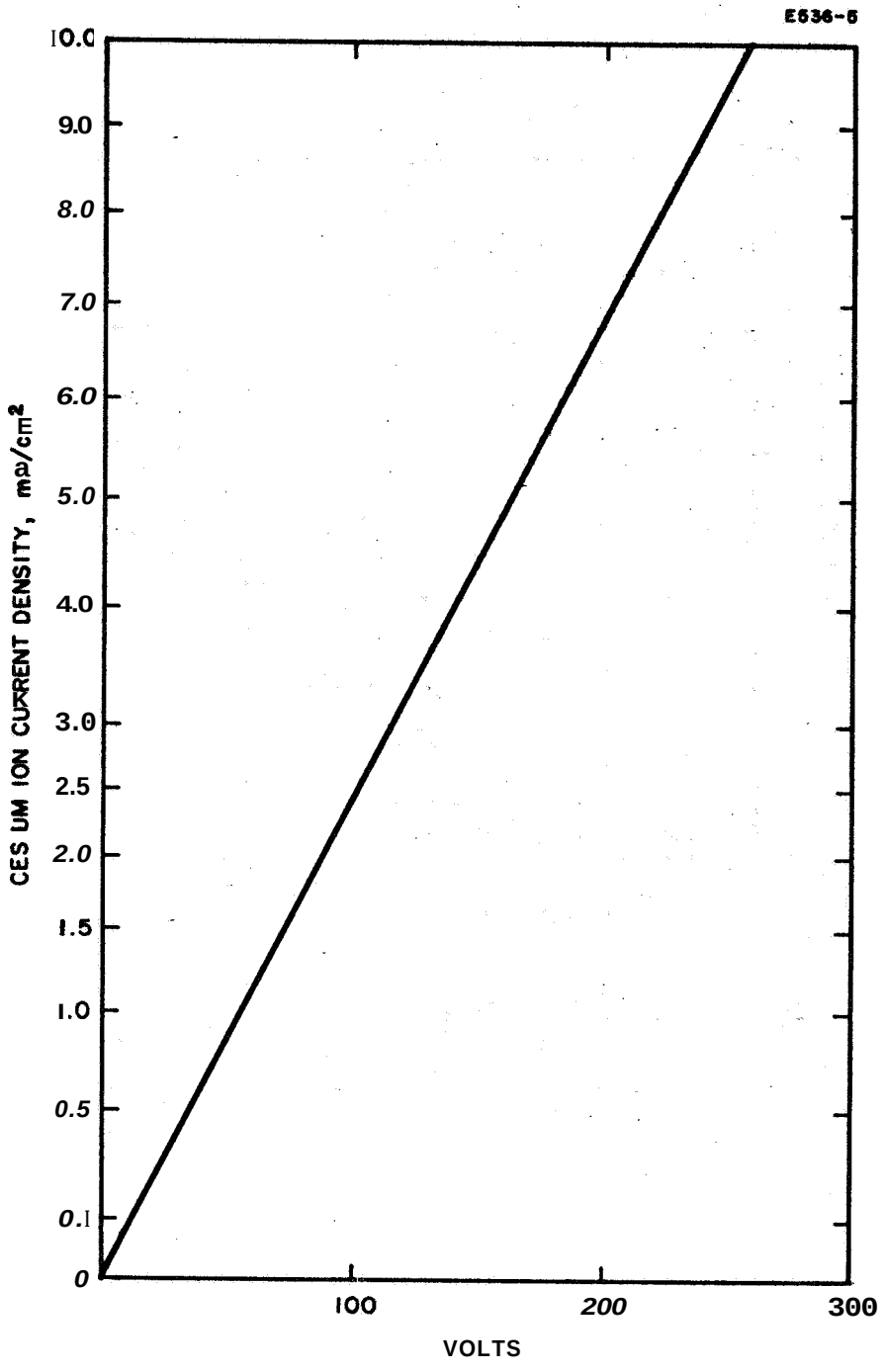

Fig. 8. Ion current density versus extraction potential for the guard ring diode. The cesium ion perveance is $P = 4.74 \times 10^{-8}$ A/V3/2.

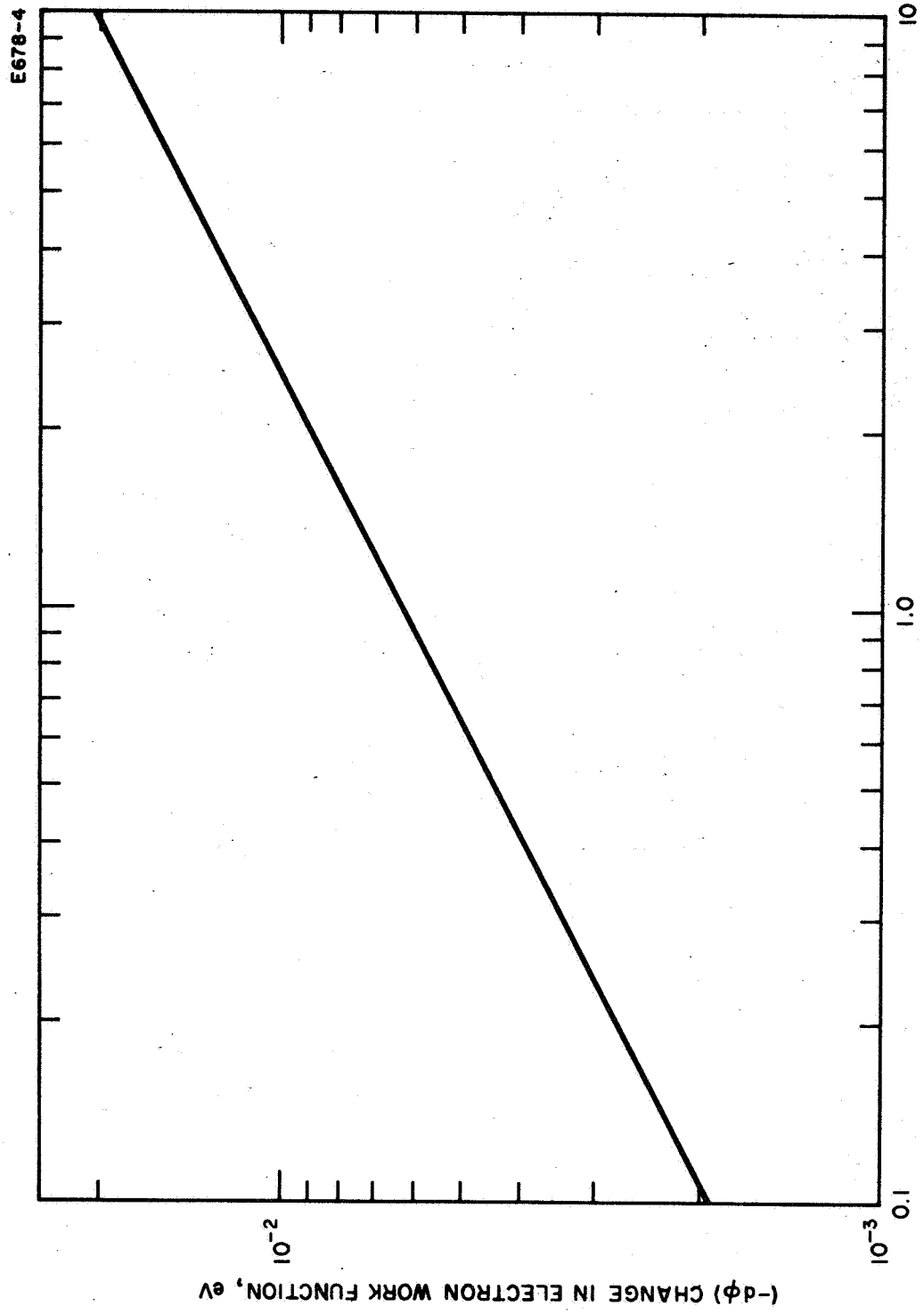

Fig. 9. Change in electron work function with the electric field E(kV/cm).

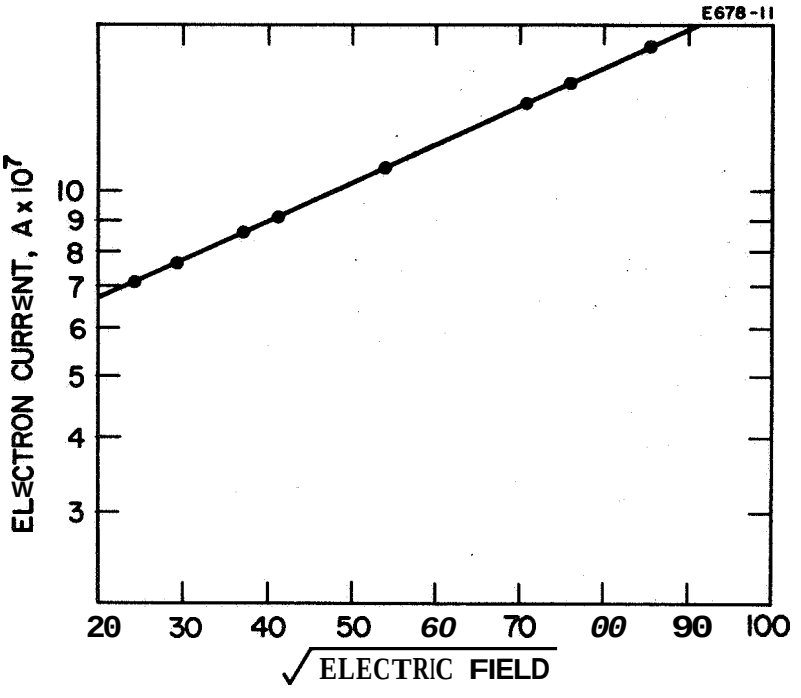

Fig. 10. Shottky effect: The electron current increases proportional to the square root of the electric field, according to $di = \exp e\sqrt{eE}$.

same data. The currents measured with both instruments agree within a very small margin and both show the same reading above 10^{-6} A as a sensitive research microammeter.

Figure 11 is the Richardson plot for the W-25% Re alloy, taken after cleanup of the filament and covering five orders of magnitude of electron current density. There is no curvature of the Richardson plot (with least square fit of the straight line), even though a patchy surface such as that investigated here may produce an upward concave slope.[13] This particular filament was observed for more than three months, at room temperature (in a vacuum in the 10^{-9} Torr range) and (for about a month) at 2000°K. During this observation the electron work function remained constant, and no change in the electron emission characteristic was observed. The electron current density may be slightly overestimated because of the unknown surface roughness.

Electrolytic tank investigations showed that about 10 kV/cm are necessary to compensate a strong patch field at the emitter surface (with 1 V potential difference between adjacent patches). The equipotential lines for these (normalized) patches are plotted* in Fig. 12. Table III combines the work function data for the filaments investigated. Except for rhenium and the alloy W-25% Re, the effective work functions ϕ_e are tabulated. For tungsten, iridium, and the other alloys, the Richardson work functions ϕ_R are tabulated. The work functions affect the critical temperatures for surface ionization, and will be discussed below.

F. CRITICAL TEMPERATURES FOR SURFACE IONIZATION

After clean surface conditions were confirmed by the thermionic work function data (stabilized work functions of the tungsten-rhenium alloys), the cesium capsule was opened. Critical temperatures for the cesium surface

*All patches contribute to the electron emission. However, the contribution of each patch must be weighted with its work function in the exponent. Consequently, for a given work function distribution, the high work function patches influence the electron current i only slightly.

$$i = T^2 \Sigma A_i F_i \exp - \phi_i/kT$$

with F_i the surface area of the i^{th} patch.

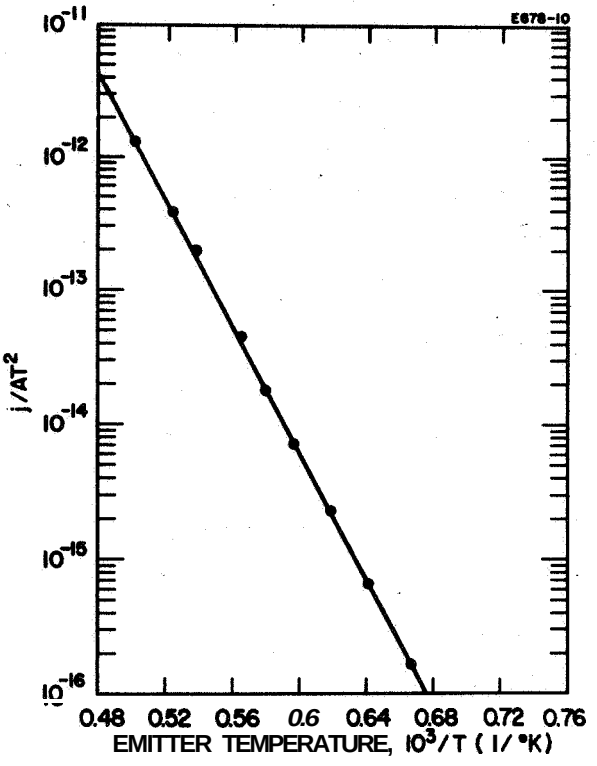

Fig. 11. Richardson plot for W-25% Re alloy. (j is in A/cm^2).

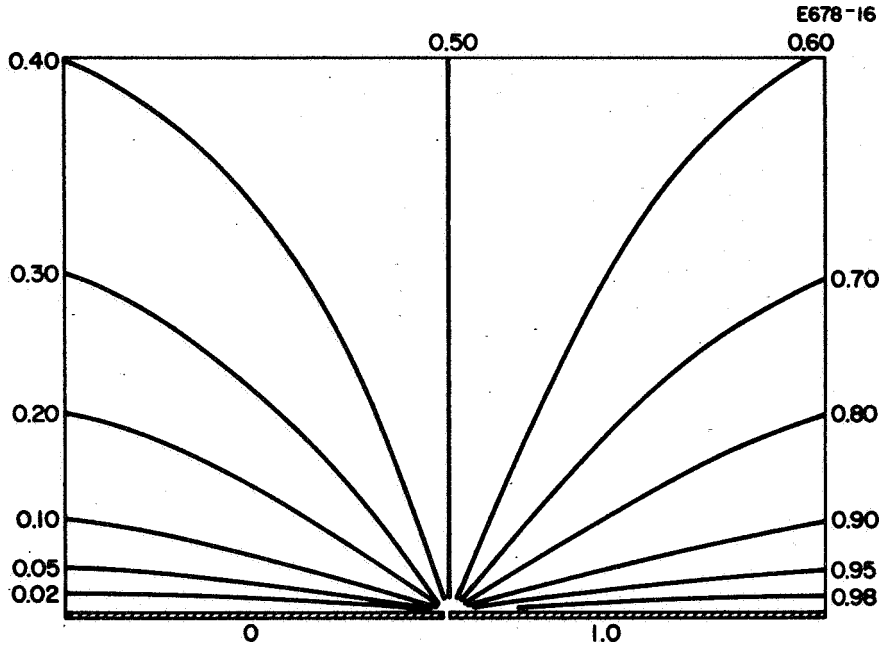

Fig. 12. Equipotential lines for normalized patch work functions.

TABLE III

Work Functions and Richardson Constants

Filament	ϕ, eV	$A/deg^2\ cm^2$
Tungsten	4.54	120
W-5% Re	4.55	120
W-7% Re	4.56	120
W-15% Re	4.59	120
W-25% Re	4.695	146
Rhenium	4.88	164
Iridium	5.40	140

ionization were measured over a wide range of ion current densities for all metals and metal alloys involved. Prior to these experiments the cesium was checked spectroscopically for impurities. All impurities were in the low ppm range, with the maximum for a single component not exceeding 30 ppm. Rubidium was so low in content that it need not be considered. The amounts of potassium and sodium are low. If we also consider their lower vapor pressures, when compared with that of cesium, the contaminant effect on the critical temperature for cesium can be neglected.

To establish a fixed cesium vapor pressure, the all metal tube was submerged in a water bath thermostat with the temperature controlled to within $0.02^{\circ}C$. The entire tube, including the flange connection, was submerged. The base .plate with the electrode feedthroughs, the ion pump, and cesium reservoir were shielded from the water vapor and maintained about $100^{\circ}C$ higher in temperature by a separate heater.

Based on their experimental work, Zandberg, et al.,[12] concluded that extrapolation of the Taylor-Langmuir data** toward higher ion current densities is not possible (see also Fig. 18 of Ref. 10). In contrast,

our T_C data on the clean tungsten surface are in agreement with Taylor-Langmuir data if the high temperature branch of the hysteresis loop is considered (Fig. 13).

With ion desorption, the Schottky effect again must be considered, as with the electron emission. The electric field lowers the ion desorption energy. At electric fields below 5×10^5 V/cm, the term $(e^3 E)^{1/2}$ governs. At higher fields, the additional terms $1/2\, E^2 (\alpha_o - \alpha_i)$ and $r_\sigma Ee$ must be considered.[33] In the presence of the electric field the Saha-Langmuir equation becomes

$$a = a_{E=0} \exp (e^3 E)^{1/2} \; t \; \frac{1}{2} E^2 (\alpha_o - \alpha_i) \; t \; r_\sigma Ee \qquad (12)$$

with

$$a_{E=0} = \frac{1}{2} \exp e(\phi - I)/kT \quad . \qquad (13)$$

a is the ratio of ions to atoms, and the factor 1/2 results from the statistical weights of ions and atoms. ϕ is the work function, I the ionization potential, α_σ the atom polarizability, and α_i the ion polarizability, with $\alpha_\sigma = 57$ Å^3 and $\alpha_i = 2.7$ Å^3 for cesium,[34] r_σ is the ion radius of the adsorbed metal. The last term, $r_\sigma Ee$, does not strongly affect the ion desorption energy; at fields above 5×10^5 V/cm, however, the second term must be considered (Fig. 14). At a field of 10 kV/cm, the ion desorption energy is lowered by 0,038 eV with

$$- dQ_i = e(eE)^{1/2} \qquad (14)$$

$e = 4.8 \times 10^{-10}$ esu and E is expressed in V/cm/300 esu. For conversion, $1\,eV = 1.6 \times 10^{-12}$ erg. Figure 14 shows the influence of both field terms, and final desorption energy is (see Fig. 15)

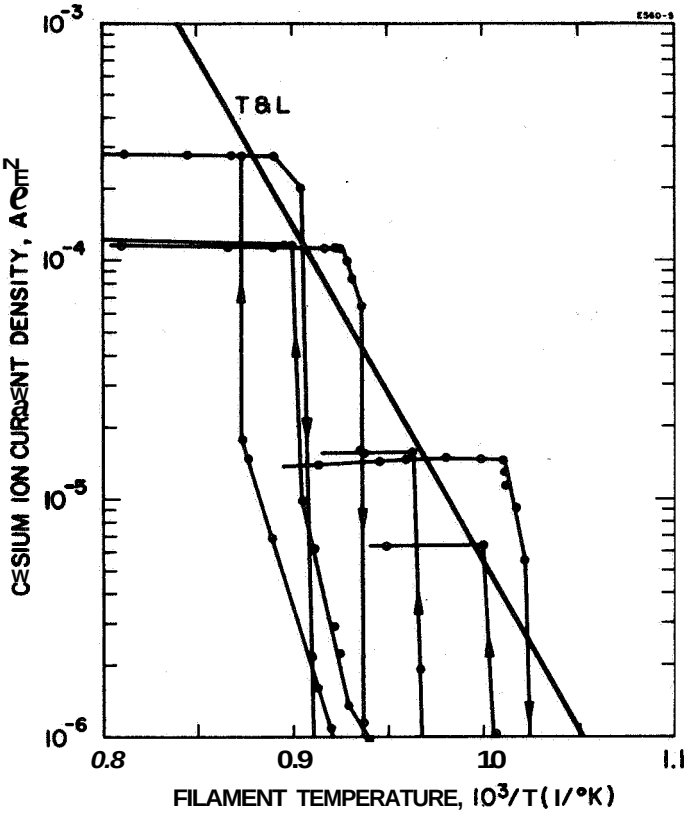

Fig. 13. Cesium threshold temperature measurements on a 2 mil tungsten filament. Within the error limit these data correspond to the Taylor and Langmuir data if the high temperature branch of the hysteresis loop is considered.

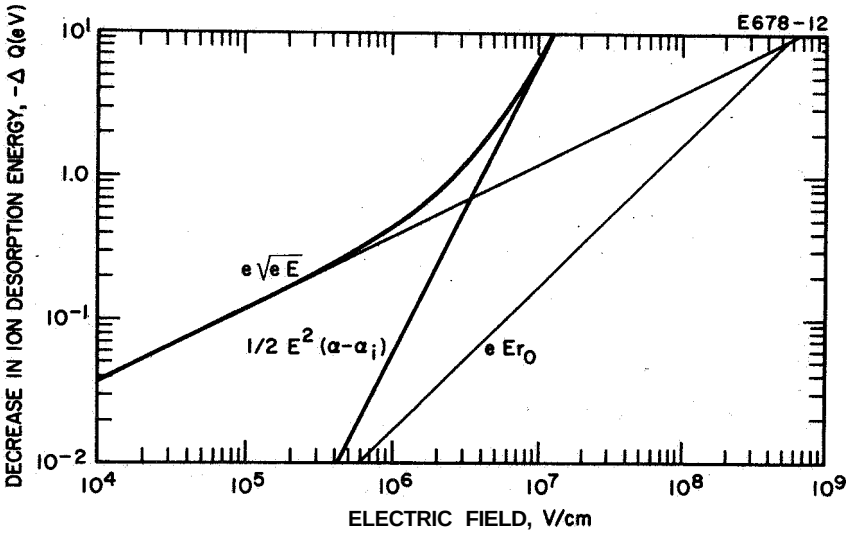

Fig. 14. Change in ion desorption energy with the applied electric field. Considered are the Schottky term $e\sqrt{eE}$, $1/2E^2(\alpha_o - \alpha_i)$, and eEr_o.

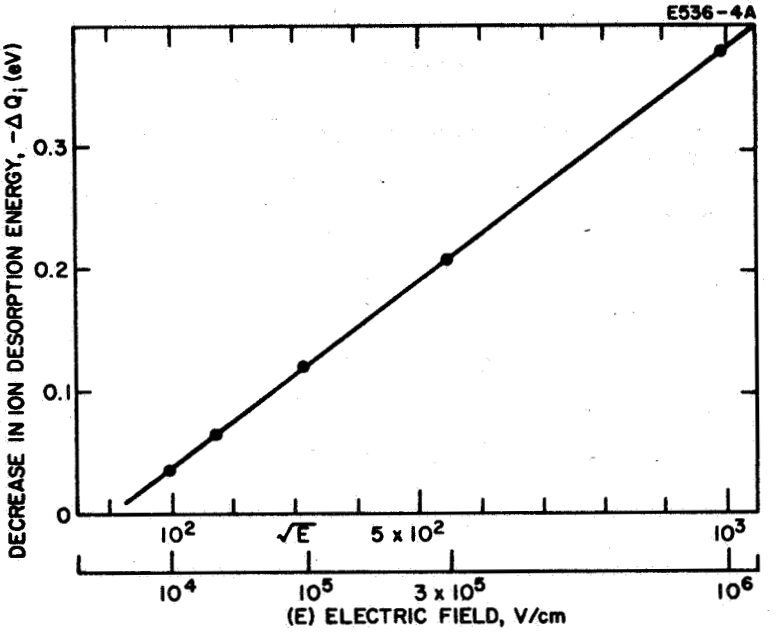

Fig. 15. Decrease of ion desorption energy due to the Schottky effect. The change in ion desorption energy is defined by $-dQ_i = e\sqrt{eE}$.

$$Q = Q_{i(E=o)} - dQ \quad .$$

The decrease in critical temperature for surface ionization is related to dQ by the Frenkel equation (eq.(2)

$$\tau = \tau_{\theta} \exp Q/kT$$

where τ is the average surface lifetime of the adsorbed atoms (or ions) and Q is the desorption energy (see eq. (4)).

$$Q_{E=o} = (k/e)\,(T_2 \times T_1/T_2 - T_1) \ln \frac{\tau_1}{\tau_2}$$

Furthermore the ion current densities and surface lifetimes are related by eq. **(3)**

$$j = e\theta\sigma_o/\tau \quad ;$$

consequently,.

$$\frac{\tau_1}{\tau_2} = j_2\,\theta_1/j_1\,\theta_2$$

with θ the surface coverage relative to the monolayer and σ_o the number of atoms/monolayer cm^2. dT_c follows from the above equations, according to

$$Q_{E=o} - dQ = f(T_c - dT_c) \qquad (15)$$

and

$$dT_c = \left\{ \left[\frac{1}{2}(T_1 + T_2) \right]^2 - (dQ/Q)(T_1 \times T_2) \right\}^{1/2} - \frac{1}{2}(T_1 + T_2) \, . \tag{16}$$

Here T_1 and T_2 are the critical temperatures for the ion current densities j_1 and j_2. The decrease of critical temperature resulting from the applied electric field is plotted in Fig. 16 for ion desorption energies 2.0 eV, 2.25 eV, and 2.5 eV. The ion desorption energy of 2.0 is close ta the measured value of 1.95 eV for cesium on polycrystalline tungsten.[19] At the field of 10 kV/cm, the critical temperature is decreased by 11°K. This decrease can be measured only if the changeover from low to high ion current density in the ionization threshold region is connected with a pronounced turnover (inside a few degrees) into the saturation region. In turn, this requires clean surface conditions, in contrast to the smooth rolling over from low to high current density, as observed on carburized tungsten, for example.[26] In Fig. 16 measured points for cesium on W-5% Re are added and compared with the theoretical slope and Zandberg data.[35] At 10^6 V/cm dT_C is slightly more than 100°K. In Fig. 17 the critical temperature for cesium surface ionization on tungsten is plotted for fields of 10^4, 10^5, and 10^6 V/cm. It is obvious that in connection with our experiments, the field at the filament never exceeds 10^4 V/cm. Consequently, no corrections are applied to the measured data.

In connection with alkali surface ionization on solid substrates, hysteresis is generally observed at zero E-field[5] (see Fig. 18). The hysteresis width increases in the presence of an electric field.[33] On the other hand, as Chaikovskii, ~~et al.~~,[5] have shown, the hysteresis width decreases with increasing ion current density. It may be emphasized that the hysteresis width does not depend on any scanning speed (Fig. 18). Neither instrumental nor emitter temperature time constants should be interpreted as such an effect.

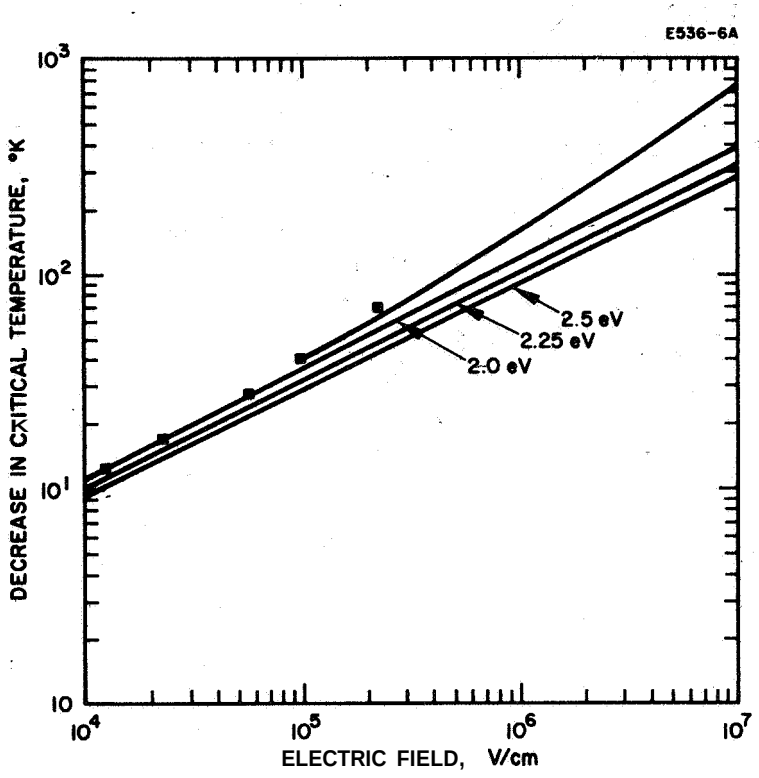

Fig. 16. Decrease in critical temperature as a result of the Schottky effect. The three lines are for ion desorption energies with Q_i = 2.0, 2.25, and 2.5 eV. At electric fields below 4×10^5 V/cm the measured points agree fairly well with the 2.0 eV desorption energy line measured here on W-5% Re. At fields above 10^5 V/cm, the term $1/2\ E^2 (\alpha_o - \alpha_i)$ is considered.

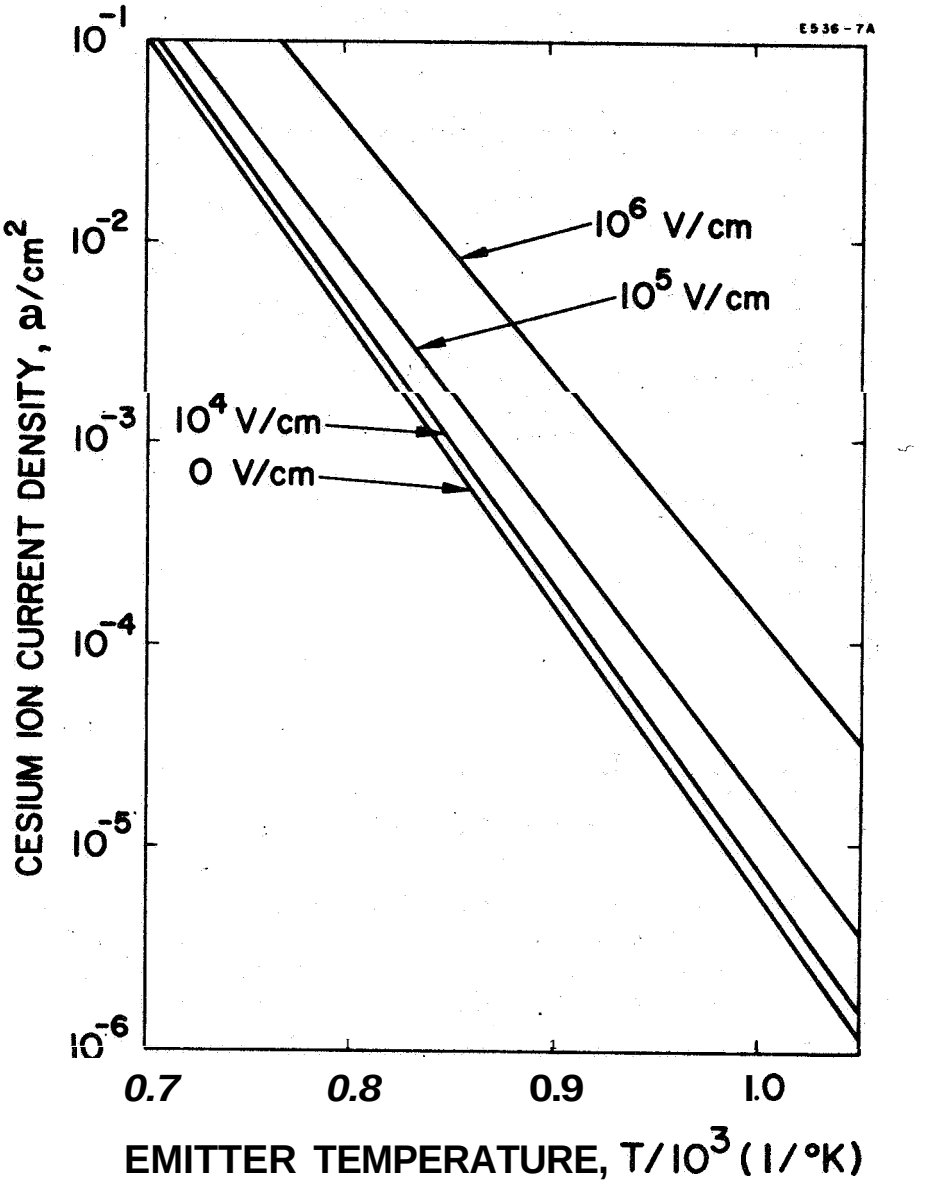

Fig. 17. Cesium ion current density versus inverse critical temperature at various electric fields.

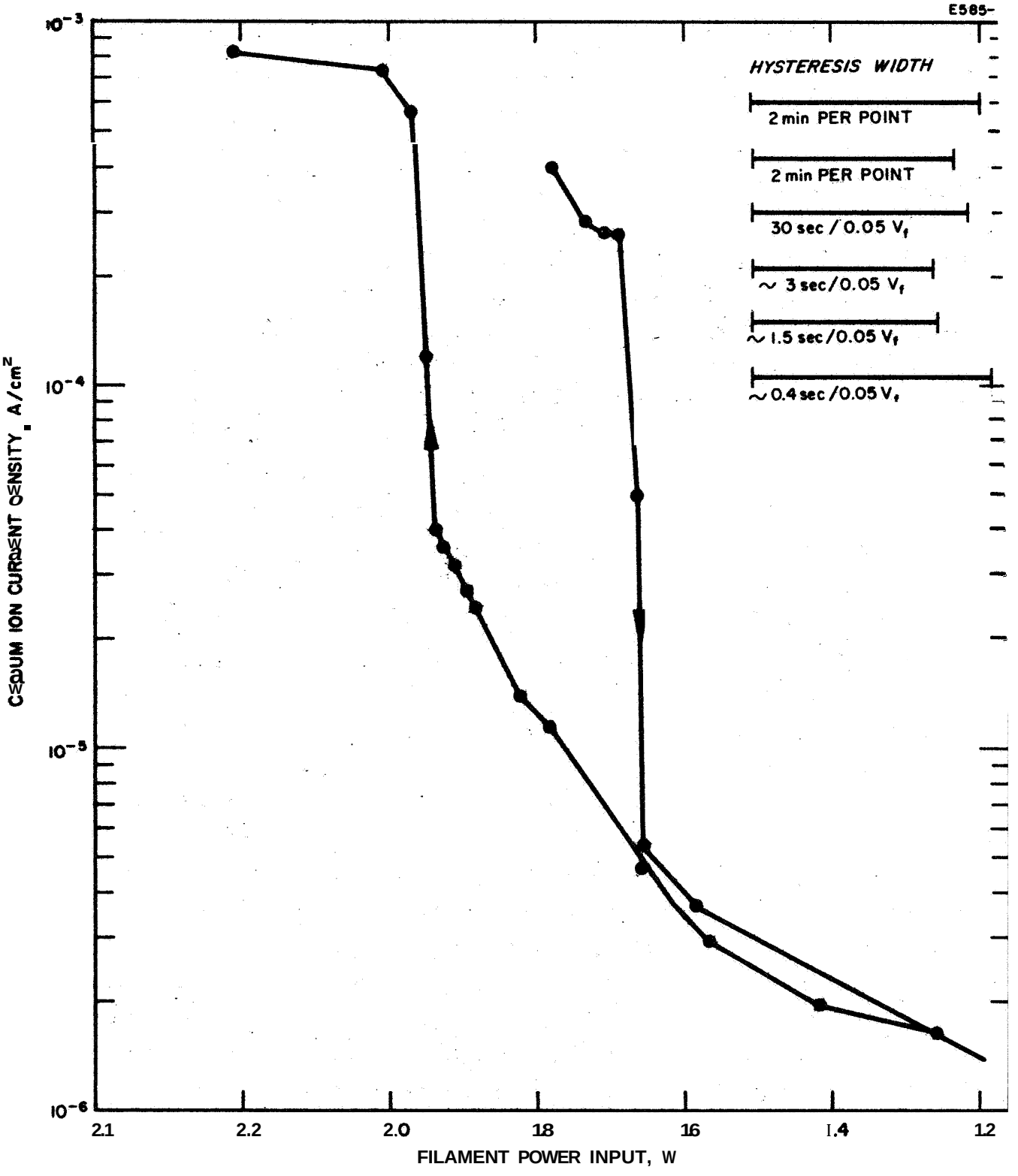

Fig. 18. Typical hysteresis plot for molybdenum filament. Inside the error limit the hysteresis width is independent of the scanning speed. (Various scanning speeds are indicated above.)

The threshold temperatures for cesium surface ionization on tungsten, W-5% Re, W-7% Re, W-15% Re, W-25% Re, and a 7 mil rhenium filament are plotted in Fig. 19 for the current density range between 10^{-5} and 10^{-2} A/cm^2. For comparison, T_c data for porous rhenium, as reported earlier, have been added.[1]

Five iridium filaments were included in this investigation. The first yielded an electron work function of 5.2 eV, while the second and third ones yielded only 5.0 eV, in contrast to published work functions of 5.3 eV and 5.4 eV.[4] As was pointed out previously, rhodium is one of the major contaminants in iridium (although it was not detected in the spectral analysis). Heat cleanup of iridium is difficult because of its low melting point (2454°C). Change of the iridium filament resistance during the heat treatment was noticed for several samples, and the final filament diameter of these was less than the original value. Figure 20 presents the threshold temperatures, as measured with two different iridium filaments, with ϕ = 5.2 eV. The hysteresis loop exceeds that observed on tungsten at the same cesium ion current density because of the higher work function. One iridium filament with 5.4 eV thermionic work function was lost prior to threshold temperature measurements. In Table IV the T_c of iridium is incorporated. The threshold temperature of iridium far exceeds that of tungsten.

In connection with the sputter deposition of molybdenum in ion microscope experiments, the critical temperature of this metal is of interest. (A polycrystalline surface was investigated, in contrast to the single crystal surface deposit described later in this report.) An undoped GE molybdenum wire was used (3 mil diameter). Molybdenum wires frequently contain cobalt, titanium, and/or other metal additives. Spectral analysis of this wire yielded 0.12% Fe as the main contaminant, It is questionable whether the heat treatment removed all of the iron. The final work function was 4.46 eV, with A = 282 A/deg^2 cm^2, in contrast to the generally accepted molybdenum work function of 4.24 eV (Ref. 36). Table IV provides the threshold temperature constants A and B for the refractory metals and metal alloys investigated.

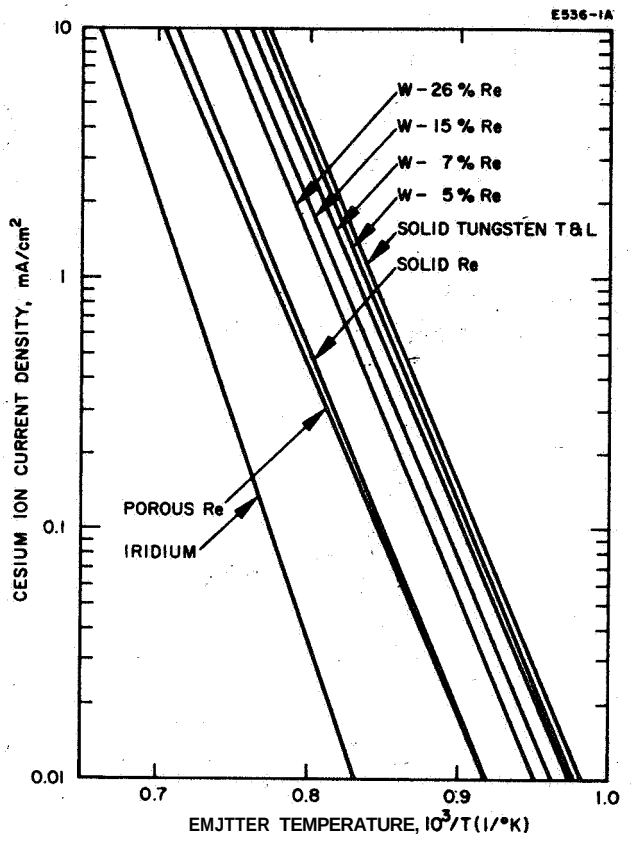

Fig. 19. Threshold temperatures for tungsten-rhenium alloys, tungsten, rhenium, and iridium. Earlier data measured on porous rhenium are added.[1]

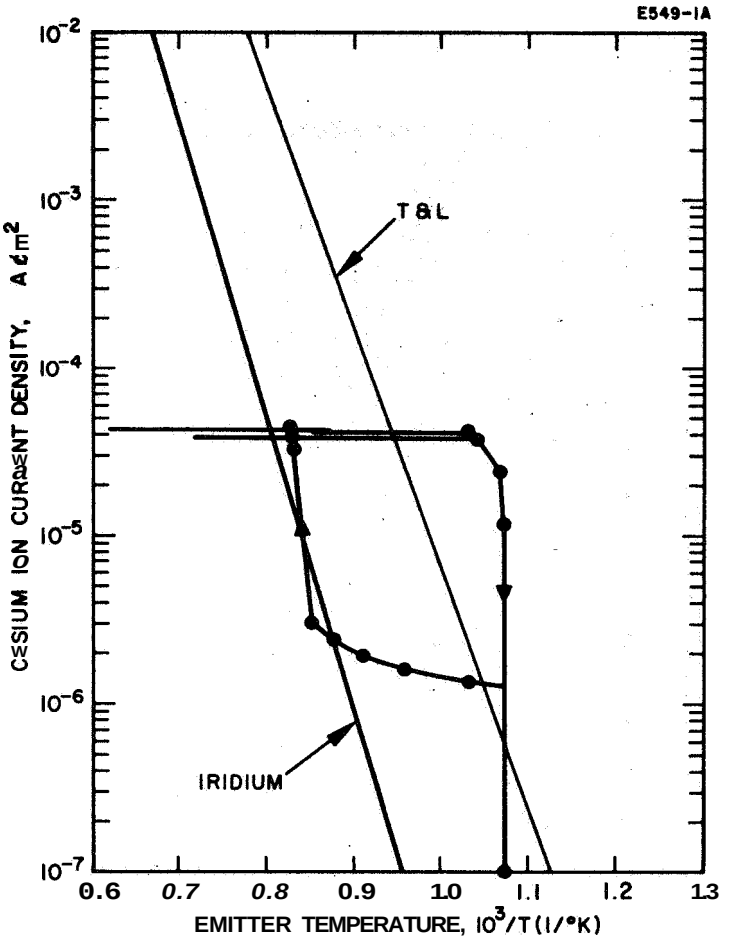

Fig. 20. Threshold temperature data for iridium. The iridium threshold temperatures were measured after the thermionic work function stabilized at 5.2 eV. For comparison, tungsten threshold temperatures are added. The hysteresis loop was measured while the work function was at 5.0 eV.

TABLE IV

Threshold Temperature Constants

Material	A	B
Tungsten	14.0×10^3	8.764
Tungsten-5% Re	13.8×10^3	8.52
Tungsten-7% Re	13.9×10^3	8.53
Tungsten-15% Re	13.81×10^3	8.30
Tungsten-25% Re	14.0×10^3	8.32
Rhenium	14.91×10^3	8.59
Iridium	16.81×10^3	9.1,
Molybdenum	12.32×10^3	7.37

The Patch Effect and Its Relation to Electron and Ion Emission

In previous paragraphs we considered the electron work function, measured on a polycrystalline surface, Here the patch effect and its influence on electron and ion emission are investigated. For all refractory metals and metal alloys included in this investigation, the difference between the thermionic work function ϕ, as measured on the clean polycrystalline surface, and the cesium ionization potential I exceeds 0.6 eV. Under this condition the Saha equation predicts ionization efficiencies exceeding 98% in the temperature range of interest. To become ionized, cesium therefore must not migrate to high work function patches,

The electron emission from a patchy surface has to be weighted exponentially with the patch work function. Under this consideration the Richardson equation is

$$\nu_e = \frac{T^2}{e} \sum_k A_k F_k \exp - \frac{\phi_k}{kT} \text{ Sec}^{-1} \qquad (17)$$

with ν_e the number of electrons emitted per second, T the emitter temperature in ^{o}K and F_k the surface area of the k^{th} patch with the Richardson constant A_k.

The number of ions ν_i emitted from a patchy surface per second is

$$\nu_i = \frac{\sigma_o}{\tau_o} \sum_k \theta_k F_k \exp - \frac{Q_k}{kT} \text{ Sec}^{-1} \qquad (18)$$

This equation is derived at by using the Frenkel equation (2) and the relation

$$\nu_i = \frac{\sigma_o \theta F}{\tau}$$

Q is the ion desorption energy with [19]

$$Q = 0.722 \ (\phi - I) \pm 1.47 \text{ eV}$$

and in case of cesium, we have

$$Q = 0.722 \ \phi - 1.34 \text{ eV} \qquad (19)$$

and

$$\Delta\nu_i = \frac{\sigma_o \theta}{\tau_o} \exp - \frac{Q}{kT} \left[F_i - F_k \exp - \frac{0.722 \ \Delta\phi}{kT} \right]$$

$$\Delta\nu_e = \frac{T^2}{e} \exp - \frac{\phi}{kT} \left[A_i F_i - A_k F_k \exp - \frac{\Delta\phi}{kT} \right] .$$

From the above equations, it follows, at 1300°K,

$$\Delta\nu_i \propto \exp - 6.44\, \Delta\# \qquad (20)$$

$$\Delta\nu_e \propto \exp - 8.9\, \Delta\# \quad . \qquad (21)$$

In both cases, ion as well as electron emission, the work function change is in the exponent of the weighting factor for the patch emission. Because the same surface is considered here for both types of emission, we conclude that with $(\phi - I) \geqq 0.6$ eV, the electron work function of the patchy surface is also the work function, which governs the ion emission and with it the ionization efficiency and the threshold temperature for surface ionization.

In connection with the increased mean ion lifetime of high work function patches, the surface coverage there increases relative to the low work function patches and cesium migration from the high work function patches to low work function ones is probable.

G. WORK FUNCTIONS, CRITICAL TEMPERATURES, AND THE TUNGSTEN-RHENIUM PHASE DIAGRAM

The measured work functions and critical temperatures of the tungsten-rhenium alloys indicate a nonlinear continuous increase of both with the amount of rhenium in tungsten (see Fig. 21). The projections into the phase diagram have no maxima, as would be expected in accordance with the theoretical consideration of Levine, et al.[20] The range between 25% and 100% rhenium in the phase diagram is extrapolated (dashed lines). The continuous nonlinear change of work function and

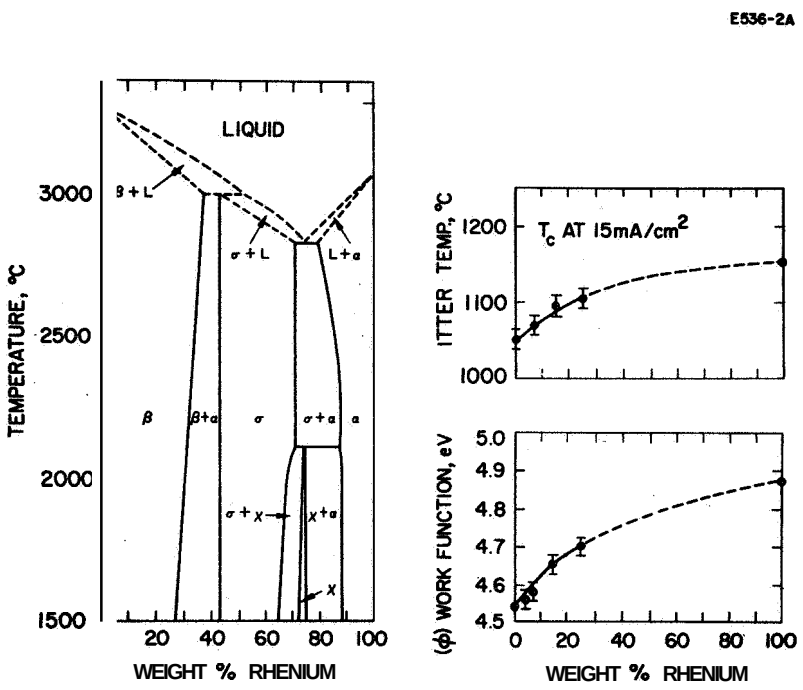

Fig. 21. Projection of work functions and threshold temperatures onto the tungsten-rhenium phase diagram. The dashed lines are interpolations.

critical temperature is in good agreement with the secondary electron emission behavior of this material, as reported by Dyubua.[18] The minimum work functions of the cesiated tungsten-25% rhenium, rhenium, and iridium filaments are 1.3, 1.1, and 1.3 eV, respectively. In contrast to the small change on porous emitters, the electron emission current changes by passing through the "S" curve over about three orders of magnitude at constant cesium vapor pressure. Changes on the porous material are about one order of magnitude.[26] In Fig. 22 these curves are plotted for cesium vapor pressures corresponding to bath temperatures of 24°C, 51°C, and 79°C. The pressures have been computed according to Ditchburn, et al.[37]

$$\log p = 11.176 - 1.4 \log T - 4042/T \qquad (22)$$

with p in Torr and T in degrees Kelvin. The measured ion currents are in good agreement with the vapor pressures, if we assume a sticking probability of 1 for cesium. The number of impinging atoms/cm^2-sec is given by

$$N = \frac{1}{4} n \bar{v} = 3.5 \times 1022\, p/(MT)^{1/2} \qquad (23)$$

with M the atomic mass number. n is the number of molecules per cubic centimeter and $\bar{v}$ the average velocity in centimeters per second.

As explained earlier, it is difficult to measure the filament temperature in the range below 1000°K. Therefore, the temperatures above 1000°K were carefully calibrated against the electric power input and then extrapolated to zero power input with T = 300°K. The error limit should not exceed 0.1 eV.

Secondary Electron Emission and Threshold Temperature

Secondary electron emission does not contribute to the ion current reported here because of the low ion extraction potential employed in these

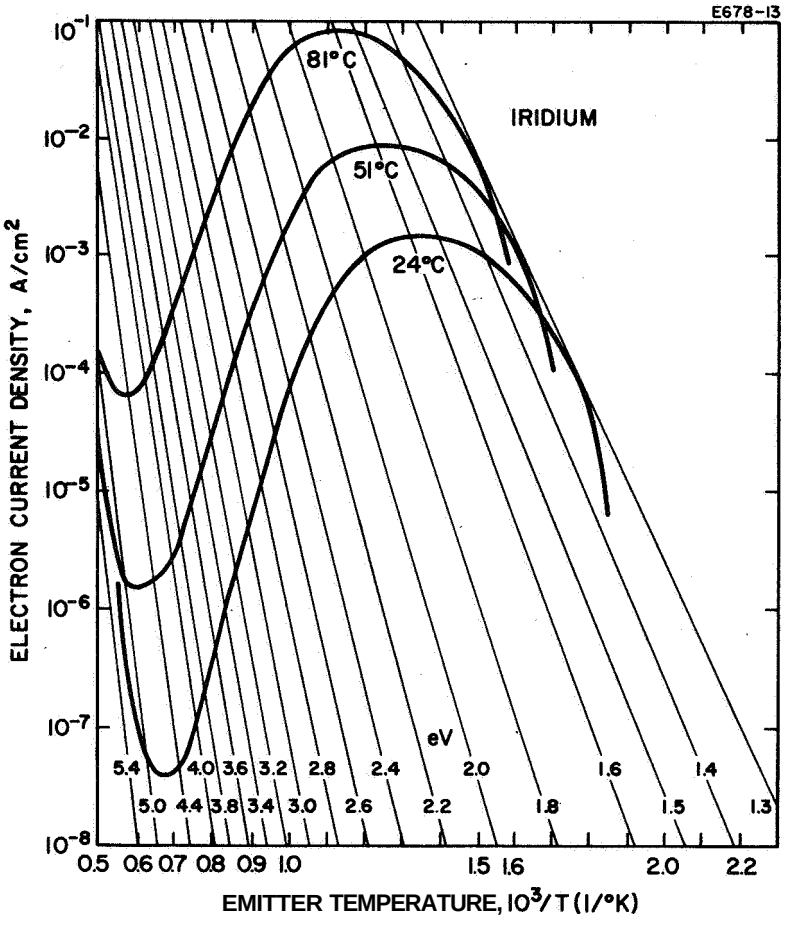

Fig. 22. Minimum work functions of the cesiated iridium filament. The thermionic work function under clean surface conditions here was 5.2 eV and the minimum work function is 1.3 eV.

measurements, The threshold for secondary electron emission from tungsten is about 150 V, as reported by Waters,[37(a)] and the secondary electron yield decreases from Li toward cesium, as reported by Bruenne[37(b)] for molybdenum. The maximum potential used in these experiments for cesium ion extraction does not exceed 300 V. At 300 V, the secondary electron yield for Cs on Ni is less than 1%. Therefore, the ionization threshold temperature is not affected.

Photoelectron Emission

The threshold wavelength for photoelectron emission λ_{th} is

$$\lambda_{th} = 3 \times 10^{18} \times h/\phi \quad \text{Å}$$

with $h = 4.136 \times 10^{-15}$ eV sec and ϕ the collector work function. For clean polycrystalline nickel, the threshold wavelength is $\lambda_{th} = 2530$ Å; for a cesium monolayer with $\# = 1.8$ eV, $\lambda_{th} = 6900$ Å. The experiments do not indicate photoelectron emission below 1500°K. This is emphasized by the constant saturation ion current over a wide temperature range. The saturation ion current densities also are in excellent agreement with cesium vapor pressures, according to $\log p = 11.176 - 1.4 \log T - 4042/T$ with p in Torr and T in °K (see Ref. 37) and $i = 0.794\, p_{Torr}/\sqrt{T}$.

Filament Contamination by Sputtered Material

It has been pointed out that gas adsorption from the residual gas atmosphere and bulk contaminants, diffusing to the surface, change the filament work function and the threshold temperature for surface ionization. Another source of contamination can be deposition of sputtered material. To avoid any such effect, the outer electrode of the guard ring diode should be of the filament material. Even then, heat cleanup of the electrode remains a problem. Furthermore, not all metals originally considered for this investigation are available in sheet form.

The cesium ion perveance of the diode is 4.74×10^{-8} $A/V^{3/2}$; with ion current densities of 10 mA/cm^2 and a filament diameter of 50 μ, extracticn potentials of 260 V are necessary. This is far above the sputtering threshold of any metal. For refractory metals (such as tungsten, tantalum, and rhenium), the threshold is 30 eV; the threshold energy for low melting point metals which are competitive with cesium (such as copper and nickel) is 17 eV and 20 eV (Refs. 37(c) and 37(d)). Here nickel is used as the electrode metal. The sputtering yield of nickel under bombardment with 260 eV xenon ions is 0.4 (Ref. 37(e)); it is 0.15% for the same ions at 50 eV. A 0.2 mA/cm^2 cesium ion current density can be measured without sputtering. Above 20 eV ion energy, the work function change is particularly strong on the iridium filament. To eliminate the sputtering effect above 0.2 mA/cm^2, only the upper threshold temperature has been measured, by adjusting the temperature with the extraction poteatial close to and above space charge limiting conditions. After each measurement, the filament was heat cleaned and its work function checked. Low threshold temperature data are extrapolated from low current density measurements. With sputter deposition, the T_C changes to that of the deposited metal. Nickel on iridium lowers the T_c, while this deposit on tungsten yields a higher T_c.

SECTION III

NEUTRAL EFFLUX AND THRESHOLD TEMPERATURES MEASURED ON POROUS PELLETS COATED WITH IRIDIUM AND RHENIUM AND ON THE W-25% Re ALLOY

For evaluation of the porous pellets, the ion beam deflection technique has been employed, as described earlier.[38] Besides other advantages, this technique prevents metal sputter deposition onto the ion emitter, and the neutral efflux is measured opposite to the emitter. The contribution of charge exchange ions to the neutral efflux is negligible.[39] For all investigated pellets, the neutral efflux is complementary to the ion current, The work function resulting from the neutral efflux data at low ion current densities (Saha equation) is identical with the thermionic work function.

The thermionic work function was measured on a variety of porous tungsten pellets with ϕ = 4.54 eV. At cesium ion current densities in the 0. 1 mA/cm^2 range, this thermionic work function is in excellent agreement with the Saha equation work function as based on the neutral efflux measurements. However, with increasing ion current density the neutral efflux increases stronger from the porous surface than anticipated in connection with the increased surface ionization threshold temperature, Besides its dependence on the ion current density, the Saha equation work function also decreases with decreasing emitter pore density or more general with increasing flow rate per pore.[38,1] In the case of 2 x 10^6 pores per cm^2 (traverse counting technique) and 10 mA/cm^2 cesium ion current density, the Saha equation work function is 0. 18 eV below the thermionic work function. Above considerations are in agreement with neutral data reported earlier for porous tungsten,

One group of investigators reports at low ion current densities a neutral efflux distribution different from the cosine distribution with a peak orthogonal to the emitter surface.[40(a)] This would result in too high neutral efflux measurement. Also the geometrical factor of the

neutral detector relative to the emitter changes in case of deviation from the cosine distribution during ion extraction. (All investigators agree to the cosine distribution in case of no ion extraction.[40(b)]) Neutral efflux data measured with our neutral detector opposite the ion emitter show a constant geometry factor and furthermore the total alkali flow rate remains constant under the cosine distribution conditions, if the $T^{-1/2}$ dependence of the alkali flow rate through the porous pellet is considered. Here the neutral efflux may be compared to the total flux in case of no ion extraction as well as to the saturation range ion current.

Constant neutral detector geometry factor in the space charge limited as well as in the saturation range indicates a cosine distribution for our measurements of the neutral efflux from porous emitters during ion extraction. The neutral detector geometry factor measured under ion extraction is the same as that measured without ion extraction. Furthermore, this geometry factor coincides with that computed under the assumption of cosine distribution of the evaporated cesium atoms. It should be emphasized that in these measurements the neutral efflux is complementary to the ion current under space charge limited as well as under saturation conditions. It must be mentioned that in connection with the small neutral detector collimator cross section (1/8 in.) charge exchange neutrals play only a very minor role.[39] (See also Appendices II and III.) Furthermore, the threshold temperature measured by neutral efflux coincides with that measured by the ion current.

Here the Saha equation work function coincides with the electron work function of the porous emitter up to ion current densities of about $1\ mA/cm^2$ (see also Section II, page 45 ff). This in turn proves that the neutral efflux data measured here are correct, and further supports the above deduction that the neutral efflux during ion extraction follows the cosine distribution law.

The pore density of all pellets was determined by the traverse technique.[41] However, not all of the pores counted are necessarily open and contributing to the cesium conduction.

The pellet transmission coefficient {the ratio of the number of atoms leaving after diffusion through the porous pellet to the number of atoms impinging on the cesium reservoir side) was measured with helium in the molecular flow range and in the temperature range between $300^{\circ}K$ and $1600^{\circ}K$. For all pellets reported here, the $T^{-1/2}$ dependence of the helium flow rate was confirmed (Fig. **23).**

The electron work function, threshold temperature for cesium surface ionization, and neutral efflux were measured under ultrahigh vacuum conditions. No oxygen nor hydrocarbons were detected by the CEC 21-612 residual gas analyzer (with an oxygen sensitivity of 5×10^{-9} Torr/div at 20 μA electron current).

According to our standard procedure, pellet surface conditions were checked by thermionic work function measurements. None of the pellets showed the work function measured with W-25% Re, rhenium or iridium filaments. Two porous tungsten substrates were coated – one with a thin layer of iridium and the other with a thin layer of rhenium. **A** third pellet was pressed and sintered, using prealloyed and spheroidized W-25% Re powder of narrow size distribution.

The work function of the W-25% Re alloy pellet was only 5×10^{-2} eV below that measured with the corresponding filament. This may be attributed to the possibility that the original powder was mixed with small amounts of tungsten powder. The work functions of the iridium- and rhenium-coated pellets both exceeded the polycrystalline tungsten work function. Deterioration of their work functions with time of operation is attributed to diffusion of the coating material into the tungsten substrate. Despite the fact that these three work functions did not reach the expected values, we learn from these measurements that increased work function improves the ion current to neutral efflux ratio and also increases the threshold temperature. We also learn that thin chemical coatings are not sufficient to insure long term stable operation of the ion emitter. Diffusion into the substrate is discussed in more detail in Section VI of this report.

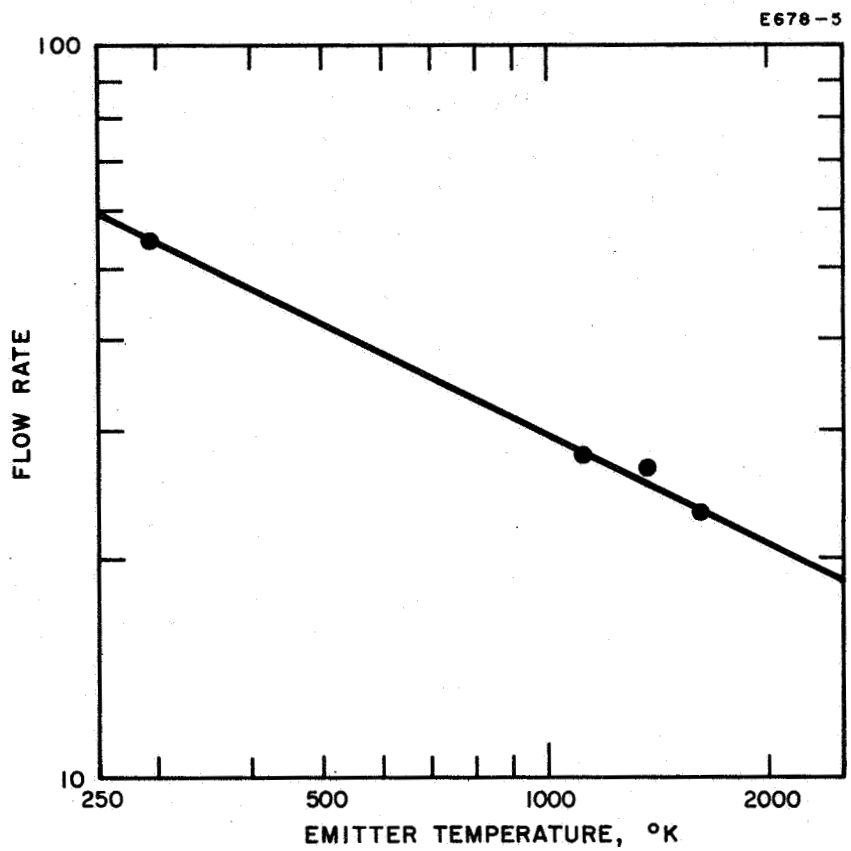

Fig. 23. The cesium flow rate through the porous pellet follows closely the expected $T^{-1/2}$ slope in the temperature range between 300 and 1700°K.

A. TUNGSTEN-25% RHENIUM ALLOY PELLET

This pellet was pressed and sintered from prealloyed spherical powder in house and was machined according to the required dimensions. [42] Finally, the copper was evaporated and the pellet directly and without difficulty electron beam welded to the standard molybdenum support. (This type of welding was unsuccessful with a porous iridium pellet because a very brittle iridium-molybdenum alloy developed in the welding zone; this zone showed large cracks after welding.) A layer of rhenium between the iridium and molybdenum led to the successful welding of these two metals.

The mean pore diameter and the mean pore distance of this pellet are, respectively, 2. 8 μ and **4.** 88 μ; the pore density is 1.7 **x** 10^6 pores/cm^2. *It* should be noted, however, that the statistical density is far below the weighted density. Therefore, the actual pore density (traverse technique) is lower and is estimated to 1 x 10^6 pores/cm^2.

After standard cleanup for several hours under UHV conditions, with small amounts of cesium diffusing through the pellet and with pellet temperatures exceeding 1600°K, a thermionic work function of 4.64 eV (with A = 350 A/deg^2-cm^2) was measured for this alloy. Under this condition the neutral efflux at a cesium ion current density of 10 mA/cm^2 reached 3.5% (see Fig. 24). At the ion current density of 0. 1 mA/cm^2, the threshold temperature is somewhat below that reported for solid W-25% Re, but it exceeds those at slightly higher ion current densities. No hysteresis has been observed. The vacuum during these measurements was in the 10^{-9} and low 10^{-8} Torr range. Consequently, we may assume that the surface is composed of W-25% Re and tungsten patches. During these experiments, the thermionic work function decreased by a small amount. A second attempt to measure the neutral efflux of this pellet under clean surface conditions yielded the same results. The work function did not improve to 4.695 eV as measured with the solid W-25% Re filament. In contrast, the work function slowly deteriorated further. Work function deterioration here is independent of cesium flow.

IONIZER PELLET EVALUATION **REPORT**

HUGHES

pellet type tungsten - 25% Re made by HRL test date 8-27-65

pellet material W-25% Re, prealloyed , mean pore diameter, μ 2.78

mean pore distance, μ 4.88 , transmission coefficient 7.19×10^5

pores/cm^2 1.7×10^6 by traverse technique, weight density ~~75~~ %

surface treatment none , statistical density 63.7 %

work function 4.64 eV, clean up process standard

with A = 350 A/$deg^2 cm^2$

misc. information made from spherodized W-25% Re alloy

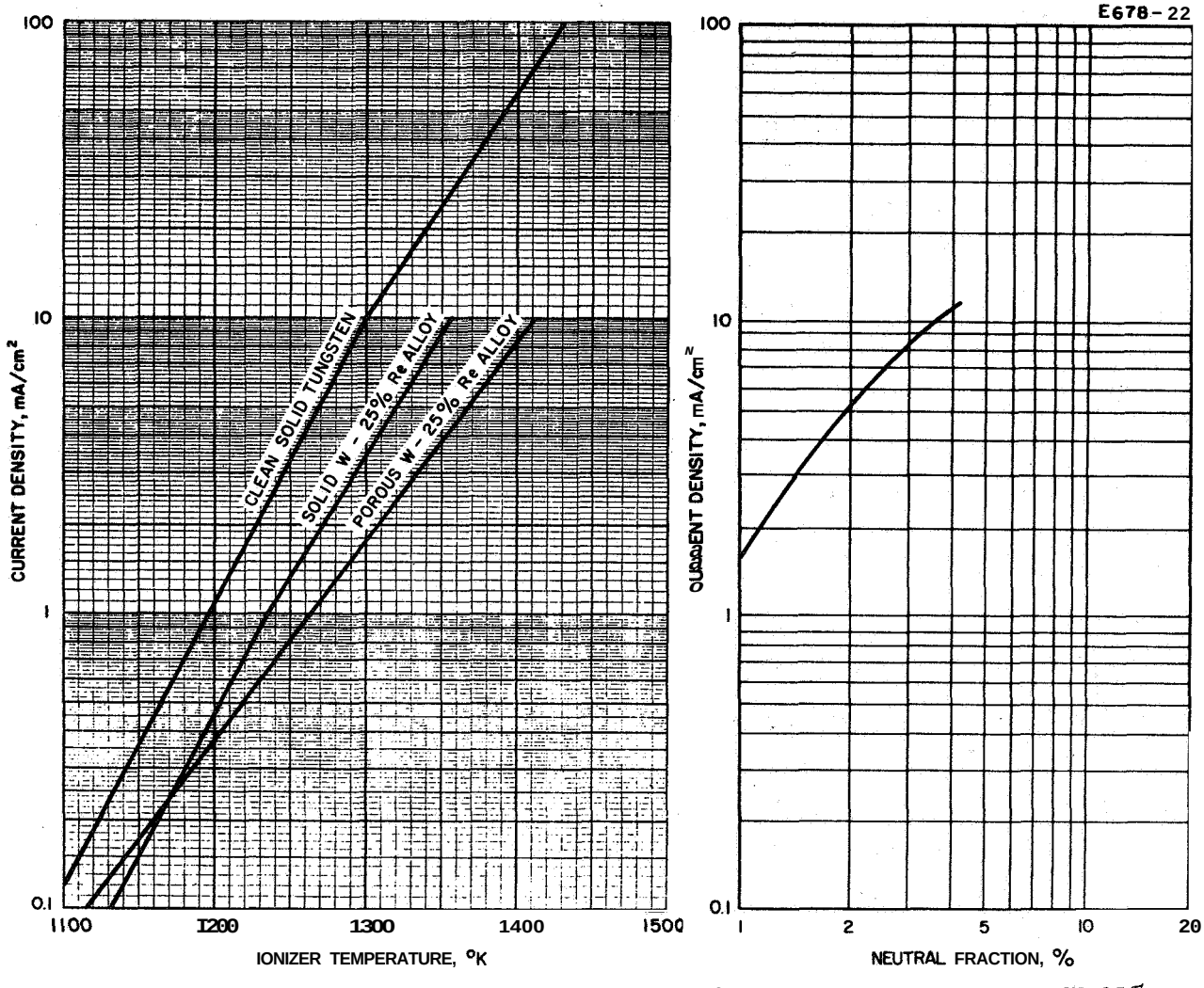

Conclusions: Data are preliminary, because work function is below that of the W-25% Re alloy. The statistical density is far below the weighted density and therefore it is concluded that above pore density is overestimated and may be close to 1×10^6 pores/cm^2.

test made by O. K. Husmann date ~~8-27-65~~ report prepared by ~~Husmann~~

Fig. 24. Neutral efflux and threshold temperature of the W-25% Re pellet. The thermionic work function is 4.64 eV.

B. IRIDIUM COATED PELLET

A Phillips Metalonics Mod B porous tungsten substrate previously had been coated with a 5-mil layer of spherical 2.4 p tungsten powder sintered to about 70% density. This coat has a pore density of 2.7×10^6 pores/cm^2 (Ref. 39). This fine grain porous tungsten layer was then chemically coated with a thin layer of iridium. The transmission coefficient of this pellet prior to the iridium coating was 1×10^{-4}; it reduced to 3.5×10^{-5} after this coating was applied. After operation at 1500°K, the pellet transmission coefficient increased and stabilized at 4.5×10^{-5}. We may conclude that the original pore density decreased in connection with the iridium coating; after coat application it was about 1.2×10^6 pores/cm^2.

When this investigation began, the electron work function indicated a strongly changing surface, with a steep decrease from about 5 eV down to about 3.5 eV during the first two days of operation, Temperatures in the 1750°K range were necessary to improve conditions. After about 3 days the work function was back at 4.8 eV (not at 5.4 eV, as reported for iridium).[1] Finally, the cesium capsule was broken and the neutral efflux at current densities below 1 mA/cm^2 was in the 0.1% range; the threshold temperatures were far greater than that for tungsten. The work function decreased to 4.7 eV by the end of the investigation. At a cesium ion current density of 10 mA/cm^2, the neutral efflux was found to be 2.1% with a critical temperature of 1565°K (compared with 1300°K for clean solid tungsten measured at the same current density). While this neutral fraction data and work function are consistent (through the Saha equation), these values are not representative of the characteristics effected of a pure iridium surface (Fig. 25).

It should be mentioned that the threshold temperature exceeds that reported here earlier for solid iridium with $\phi = 5.2$ eV; this is true even though the work function of the pellet was between 4.8 and 4.7 eV and the pore density was 1.2×10^6 pores/cm^2.

IONIZER PELLET EVALUATION REPORT

HWWLS

pellet type X-B-68-d coated made by Philips-Metalonic s test date 7-13-65

pellet material tungsten coated with iridium, mean pore diameter, μ ----------

mean pore distance, μ ---------- , transmission coefficient 3.5 x 10 - ~

pores/cm^2 1.9 x 10^6 by flow rate technique, weight density ——— %

surface treatment iridium coated by chem. deposition, statistical density ---- %

work function 5.0 eV, clean up process 1750 °K over three days

misc. information uncoated, pore density is 2.7 x 10^6 (2.4 u W-coat on Mod. B substrate)
During the measurements, the work function deteriorated from 5.0 to 4.7 eV. E678-21

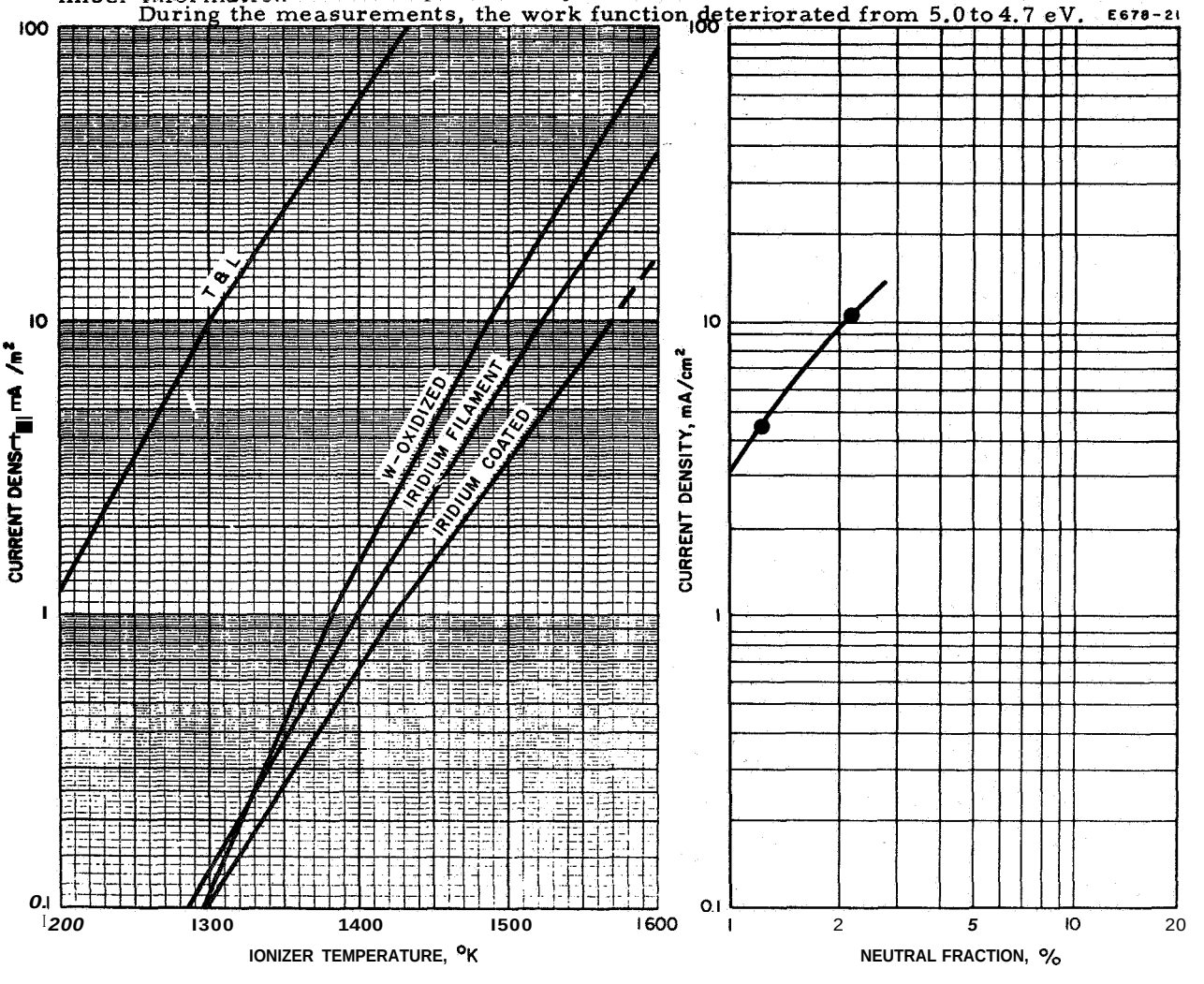

Conclusions: The critical temperature for cesium surface ionization is strongly exceeding that of tungsten. The ionization efficiency is about a factor two better than that on W.

test made by O.K. Husmann date 7-13-65 report prepared by Husmann

Fig. 25. Neutral efflux and threshold temperature of the iridium coated tungsten substrate. The final thermionic work function is 4.7 eV. T_c data for solid iridium are added.

C. RHENIUM COATED PELLET

A Phillips Metalonics Mod B pellet was chemically coated with a thin layer of rhenium. The original transmission coefficient of this pellet was 1.8×10^{-4}; it decreased to 9.8×10^{-5} after coating, indicating that the number of open pores was reduced. The final work function of this pellet, measured again under UHV conditions after the standard clean up procedure, was 4.69 eV; however, this deteriorated slightly during further operation. Some of the rhenium probably alloyed with the tungsten substrate.

The threshold temperature for cesium ions at 0.1 mA/cm^2 is below that reported for solid rhenium; at higher current densities, however, the threshold temperature exceeds that for solid rhenium, This result was expected with this low pore density pellet (with 2.27×10^5 $pores/cm^2$ uncoated) (Fig. 26).

Above 1 mA/cm^2 the threshold temperatures exceed those measured with the rhenium filament and with an all rhenium pellet. l The neutral efflux indicated a considerable improvement over that measured on the uncoated pellet, however, these data are not felt to be representative of a pure rhenium surface.

IONIZER PELLET EVALUATION REPORT

HUGHES

pellet type Mod B. Recoated made by Philips-Metalonics test date Sept. 1965

pellet material tungsten, Re wet coated, mean pore diameter, μ _____

mean pore distance, μ _____, transmission coefficient 9.78×10^{-5}

pores/cm^2 2.27×10^5 by ~~traverse~~ technique, weight density ~~_____~~ %

surface treatment ~~wet coated with Re~~, statistical density ~~_____~~ %

work function 4.69 eV, clean up process standard

misc. information _____

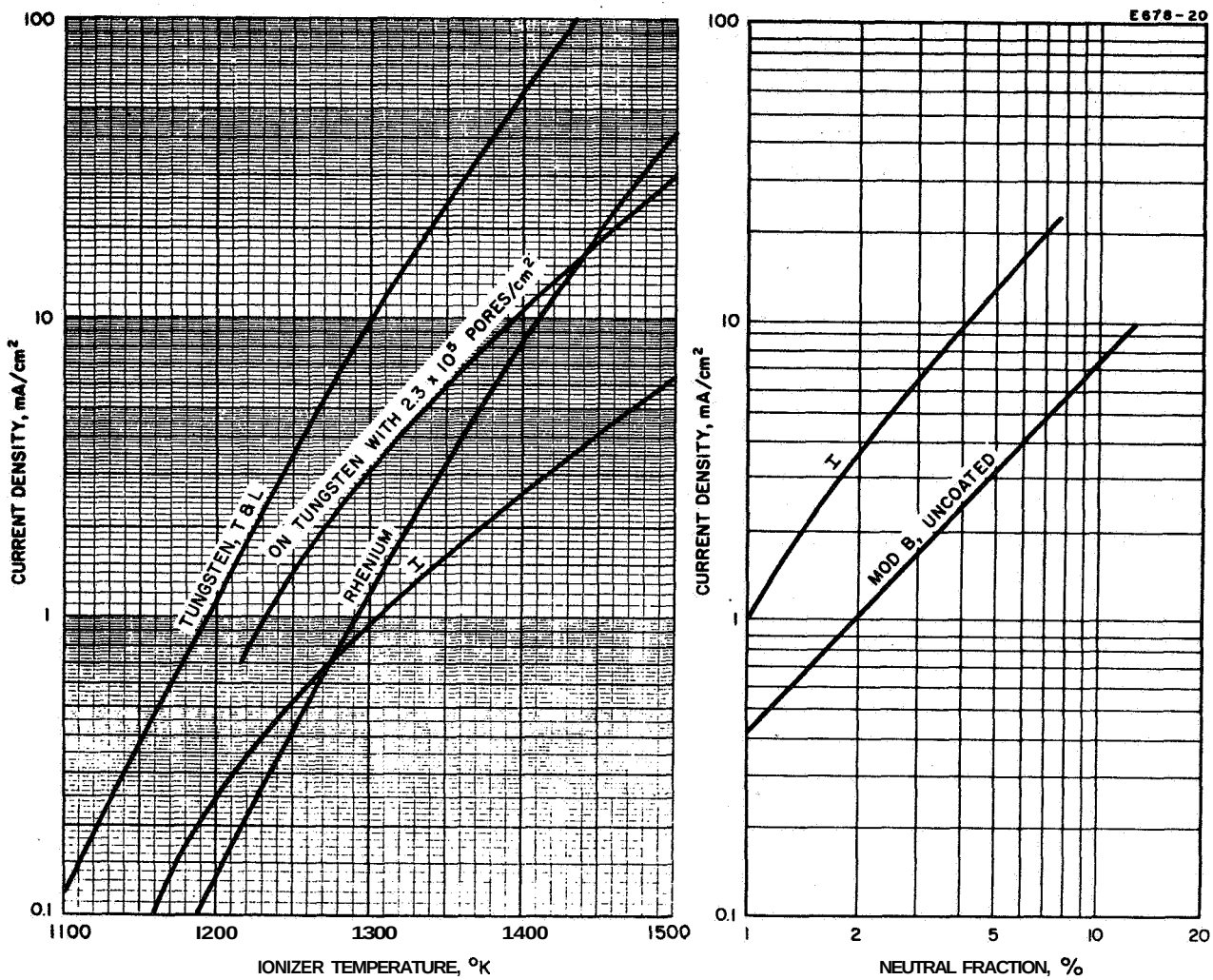

Conclusions: The steep increase in T_c is in agreement with the low pore density of this emitter.

test made by O.K. Husmann date Sept. 1965 report prepared by Husmann

Fig. 26. Neutral efflux and threshold temperature of the rhenium coated tungsten substrate. The thermionic work function is 4.69 eV. For comparison, T_c and the neutral efflux data for the uncoated tungsten pellet are added (Mod B).

D. CONCLUSIONS

The filament data show a continuous nonlinear increase of both the thermionic work function and the threshold temperature for cesium surface ionization with increasing amount of rhenium alloyed to tungsten. Threshold temperatures for rhenium and iridium exceed those measured on tungsten and the tungsten-rhenium alloys. At elevated temperatures, iridium evaporates at a much higher rate than the other metals and metal alloys under consideration here. With $\phi - I \geq 0.6$ eV, the electron work function governs the ion emission. The ionization capabilities can be improved if porous tungsten pellets are coated with a high work function refractory metal. However, the above neutral efflux data from porous W-25% Re, and also the tungsten substrates coated with a thin layer of iridium and rhenium, make it quite clear that the actual thermionic work functions of these coat materials must be reached in order to reduce the neutral efflux to the desired level, In particular, the techniques employed here of chemical deposition of the coating should be improved or replaced by advanced techniques that establish a sufficiently thick layer of deposit without reducing the emitter pore density. Another possible solution is pressing the whole pellet from the refractory metal powder.

SECTION IV

THE ION MICROSCOPE

A first report on our ion microscope development was presented in the Final Report to Contract NAS-3-4110 (Ref.42(a). At the time, the maximum magnification was 130 x, employing an electrostatic immersion lens. The ion microscope was completed during the present contract and a number of investigations were carried out with this new tool in an effort to improve understanding of cesium surface ionization of a porous ion emitter. The most important result to date is the cesium surface migration length from one pore as measured over a wide current density range. This migration length is close to 2 μ. The ion current density around the pore exit decreases steeply with increasing distance from the exit. Therefore, most of the ion emitting area is covered with less than 4% of a monolayer of cesium; a partial overlap of the emission centers improves the use of the available surface area. Consequently, for porous tungsten a pore density of 10^7 pores/cm^2 is desirable. These measurements were made under clean surface conditions, as ascertained by electron current measurements with the Faraday cage built into the microscope,

Magnifications on the order of 1000 to 1500 x are necessary for the study of the ion emission properties at the pore exits; they can be achieved by the combination of an electrostatic immersion lens and a unipotential lens. Magnifications exceeding 10^2 require improved techniques in order to make full use of the resol-.ition possible theoretically[43]

$$\delta = \frac{E}{U_e} \text{ cm}^{-1} \qquad (24)$$

with δ in lines per centimeter. U_e is the thermal energy of the ions or electrons, and E is the electric field at the emitter surface.

Electrolytic tank studies of the electric field at the emitter surface were conducted; they included the effect on the ion trajectories caused by varying the emitter-electrode distance and applied potentials at the immersion lens (see Fig. 27). These studies indicated that the E-fields were on the order of 8 kV/cm in the ranges of operation, The distance between the first and second electrodes of the immersion lens is 2 mm.[44] The distance between emitter and both electrodes is variable to allow adjustment to the proper focal length for the range of lens potentials under consideration. The first electrode aperture is 2.8 mm; that of the second is 2 mm. The electrodes, together with the emitter, form a Pierce gun system. Figure 27 shows the two different focal lengths for the inner and outer parts of the ion beam. The outer part of the ion beam does not contribute to the image because the ions are intercepted by the unipotential lens. In agreement with previous experience, the tank studies confirmed that both electrodes move away from the emitter with increasing acceleration potential if the potential at the first electrode (opposite the emitter) is kept constant. In this manner, the focal length of the central beam is kept constant. The operation is conducted so that the first electrode has a 600 V retarding potential. The emission is then restricted to a very small area in the center of the electrode aperture. Furthermore, there is no electron or ion current between the first electrode and the emitter; therefore, sputtering of the first electrode material onto the emitter is avoided. This mode of operation offers the extra advantage of high magnifications (see Fig, 28). Both electrodes are radiation heated from the emitter, preventing clogging of the apertures, and they are gold plated to prevent electrostatic charge bui1dup.

According to the tank studies, the electric field at the emitter is about 8 kV/cm for the extraction potentials of interest; consequently, the theoretical resolution is 1.25×10^{-5} cm. Figure 29 presents the

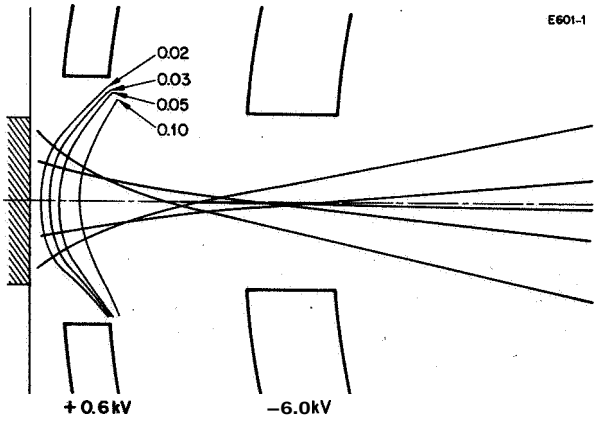

Fig. 27. Ion trajectories in the electrostatic immersion lens. The outer trajectories with shorter focal length are intercepted by the unipotential lens structure. With 6 kV at the front electrode and t600 V at the first electrode, the field at the emitter is 7.9 kV/cm.

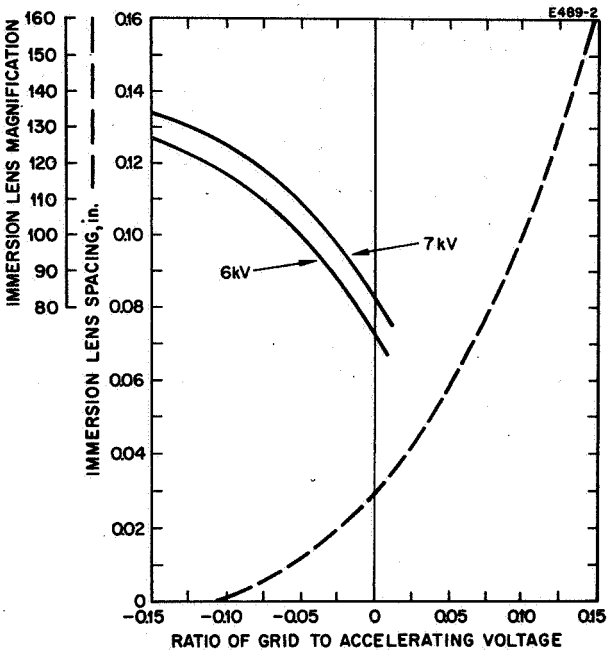

Fig. 28. Ion microscope grid voltage to accelerating voltage ratio as a function of immersion lens to emitter spacing and immersion lens magnification as a function of grid voltage to accelerating voltage ratio. (Emitter to phosphor screen distance = 20. 25 in.)

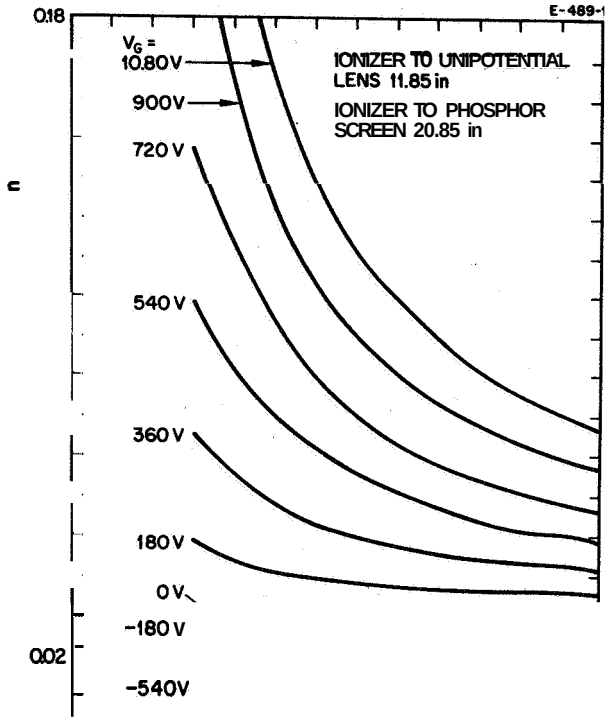

Fig. **29.**
Ion microscope acceleration potential versus distance between the lens and emitter with the first electrode potential as a parameter.

emitter-electrode spacings and the immersion lens magnifications for a number of acceleration and first electrode potentials. Maximum magnification with the electrostatic (immersion) lens is restricted to **130** X. This was measured by comparison with the optically magnified image, using a Bausch and Lomb metallograph. Images of the same area were compared (a) in the light of electron emission and (b) optically. Therefore, our magnification data are based on the optical calibration of the microscope using a standard. This was accomplished after the immersion lens distortion was minimized, using design data from Popp and Walcher.[41] This distortion can be checked easily with available emitter structure patterns. The two dimensional pattern should be constant in size, independent of the location on the phosphor.

The immersion lens equation for a circular lens is[45,46]

$$1/f = \left(1/a\,(U_2/U_1)\right) + 1/b \qquad (25)$$

with f the focal length, U_1 the potential of the first electrode, and U_2 that of the second electrode. a is the object distance and b the image distance. Figure **29** gives the electrode spacings as a function of acceleration potential with the first electrode potential V_g as a parameter. Figure ***30*** shows a cross section through the immersion lens; both electrodes are connected and movable in the z direction relative to the emitter. Similar immersion lens constructions were reported by Mecklenburg, et al.[47]

In order to increase the magnification beyond the limit of the immersion lens, aunipotentiallens was added; design parameters were patterned after those published by Pohlit, et al.[48] The design of low distortion unipotential lenses is well understood (see Archard).[47] The focal length is

$$1/f = \frac{}{8\,U_{}^{1/2}} \int^{+\infty} \left(U^2/U^{3/2}\right) dz \qquad (26)$$

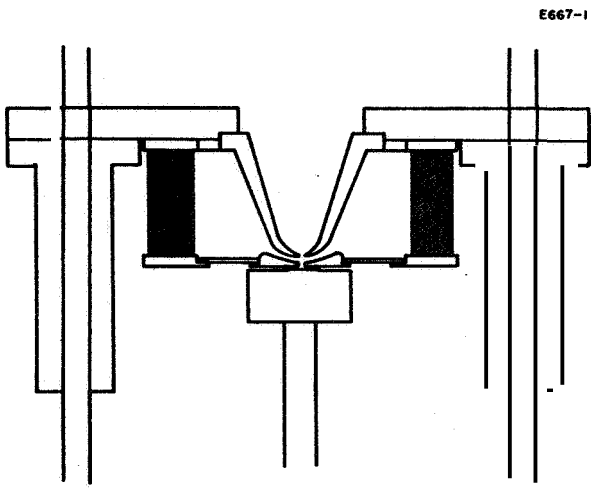

Fig. *30.*
Electrostatic immersion lens.[44]
Both electrodes are movable
relative to the emitter shown
in the center of the figure.

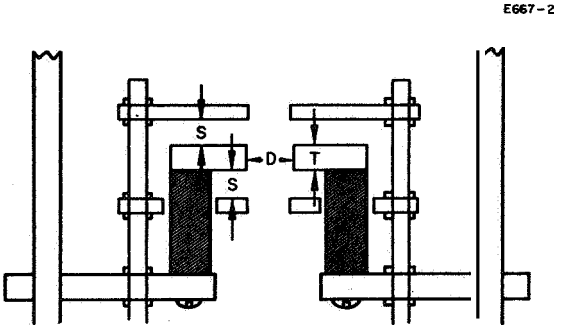

Fig. **31.**
Unipotential lens. *S*, D, and
T correspond to dimensions
reported by Lippert, et al.,[48]
and Archard.[47]

In addition, $1/f = 1/a + 1/b$, and the magnification is $V = b/a$ with. f the focal length, U_o the potential in front of the lens, U_B the potential behind the lens, U the potential at the axis ($dU/dz = U'$), a the object distance, and b the image distance from the main plane. V is the magnification. Three unipotential lenses were designed, The one with the highest magnification (and therefore the smallest aperture) is shown in Fig, 31. The focal length of this lens is described by

$$f \cong (8/3)(S + T/2)[(1 + (2\,S/D) - T/(2D)/(2\,S/D)]^2/(1 - V_L/V_o)^2$$

with S, D, T, V_L, and V_o according to Fig. 31. This lens has a fixed position above the immersion lens and only the potential of the central electrode is variable. (It is connected directly to the emitter by a variable calibrated voltage divider.) The acceleration electrode of the immersiop lens and both outer electrodes of the unipotential lens are operated at ground potential.

Minimum image distortion of the surface under investigation is of major importance for work function studies of the emitter surface and for ion current density measurements. Minimum spherical aberration coincides with the condition of maximum lens strength. As a weak lens approximation, the third order coefficient of spherical aberration[47] C_s is

$$C_s = 3.5\,f^3/(S + T/2)^2 \qquad (27)$$

with f the focal length and S and T dimensions of the unipotential lens (see Fig. 31). The chromatic abberation follows the theory of Glaser and Schiske.[49]

The electron work functions on small emitter surface areas can be measured, i, e. , in connection with the patchdistributionfunction study.

The microscope is designed to permit x-y motion of the emitter, so that it is possible to scan its entire area. This can be accomplished, for example, by the traverse technique; automatic plots of ϕ versus location are possible. Furthermore, the work function is used as a check for clean surface conditions. The electron current density from a small surface area as measured by the Faraday cup is

$$j = i\,V2/r2\,\pi \quad A/cm^2, \tag{28}$$

i is the measured emission current, V is the magnification (by optical calibration), and r is the radius of the Faraday cup,

Ions with energies greater than about 20 eV sputter the target material,[50] In particular, most of the phosphors are very sensitive to sputtering and, as in the case of ZnS, lose their fluorescent characteristic. The ZnSi phosphor performs somewhat. better. Aluminum backing does not reduce the sputtering rate sufficiently. Phosphor lifetimes under ion bombardment are generally too short for the observations reported here.[51] On the other hand, image converters perform satisfactorily.[52] The most common form of image converter and, the type used in this microscope, employs a secondary electron cathode in the form of a 500 (maximum 1500) mesh nickel grid mounted parallel to the aluminum backed phosphor. The resolution of this type of converter is

$$\delta = 4d\,(U_e/U_B)^{1/2}\ \text{mm}$$

with d the distance (in millimeters) between the nickel grid and the phosphor, U_e the mean velocity of the secondary electrons released by ion impact on the nickel cathode, and U_B the acceleration potential for the secondary electrons in the space between the phosphor and grid, U_B for this microscope is 10 kV. U_e (maximum yield) is on the order of 2 eV. As long as the secondary electron yield η of the ion to electron

converter is ≥ 1, the phosphor light output B_{asb} equals or exceeds that experienced with direct electron bombardment:

$$B_{asb} = j_i x\, b x\, U_b\, x \eta\, x \sin\theta \qquad (29)$$

with j the ion current density in amperes/centimeters^2, b the light output of the phosphor (asb W^{-1} cm^2), U_B the converter accel potential, and θ the ion impact angle. The response of the phosphor to ions is generally smaller than that to electrons. An exceptionare helium ions.[53] Ions hitting the nickel mesh at an angle smaller than 90^o produce double images because of their ballistic trajectories in the retarding field between the grid and screen. The ghost intensity exceeds that of the actual image because the second image is produced by secondary electrons released inside the accel area; they do not have to be drawn through the mesh. With a sufficiently high ion retarding potential between phosphor and grid, the distance between actual and ghost images can be minimized. The ion microscope resolution further depends on the factors described below.

Magnetic fields affect the electron and ion trajectories, particularly at low particle velocities (e.g., directly above the emitter). Here the electrons or ions are close to the magnetic field of the emitter heater spiral. The trajectory deflection angle θ is proportional to the filament magnetic field at emitter surface.

$$\sin\theta = 6.95 \times 10^3\, L \times u_o\, H/(MU)^{1/2} \qquad (30)$$

where U is the thermal energy above the emitter surface and M is the amu for electrons or cesium, $u_o = 4 \times 10^{-7}$ V sec A^{-1} m^{-1} and $L = 10^{-5}$ m. H is in ampere turns per meter, The heater is located about 1 cm from the emitter surface, and the magnetic field at the emitter surface is reduced to approximately 1% of its original value. The

average heater current is 10 A, with a maximum of 15 A and a minimum of about 6 A. The electron or ion path length with thermal velocity is assumed to be about 10^{-5} m. For 2000 x magnification we have

$$S = \sin\theta \times V = 7.85 \text{ mm}$$

where S is the deflection length. Consequently, ac heating cannot be used here; dc heating with low ripple is required.

Vibration of the emitter relative to the separately supported immersion lens electrodes and unipotential lens produces an effect similar to that produced by ac heating of the emitter; that is, it is similar as far as the frequency range of the vibration and the amplitude are concerned (see Fig. 32). The electrostatic lens electrodes are all connected to the microscope walls. Therefore, the problem is the natural frequency of the separately supported emitter electrode. Experiments showed that this frequency range, as measured with a recorder pickup head, is in the 105 cps region, neglecting the higher harmonics. Depending on the building vibration, the amplitudes were sometimes high and disturbed the microscope operation. The ion microscope was initially supported on hard rubber mounts and later layers of soft rubber were added, To isolate the microscope from the strong ground vibrations, a 1000 lb concrete block was set up as the microscope support; this, in turn, was mounted on hard rubber. The natural frequency of the whole system is a few cps and is now better isolated from the vibration of the laboratory floor.

The resolution is further reduced by the development of space charge lenses on the emitter surface, in both the electron and ion emission states. Because this microscope is generally operated with fields of 8 kV/cm at the emitter surface, these space charge effects are nearly eliminated.[54] If there is emitter surface roughness, the resolution and contrast are distorted because the equipotential surfaces are distorted. A highly polished emitter surface provides the best results.

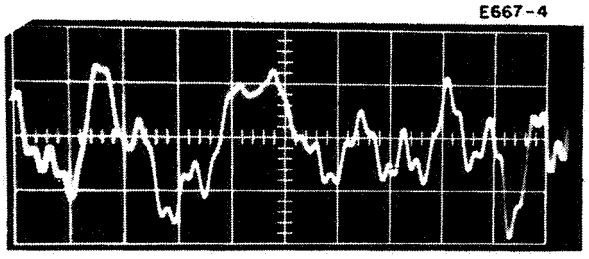

Fig. 32.
Vibration diagram, measured at the emitter prior to placing the ion microscope on a 1000 lb concrete block.

As was pointed out above, the immersion lens was calibrated by comparison with an optical image of the same area, using an optical calibration standard (see Fig. 33). In Fig. 33, from left to right we observe a single crystal area of molybdenum with 500 x optical magnification (Bausch and Lomb metallograph), a 321 x magnification in the light of electron emission, and a 590 x magnification of the electron emission pattern of this single crystal surface. The shingle Structure, which is obvious in both the optical and electron images, should be noticed. The bright lines in the shingle structure are areas of low work function,

Figure 34 represents the total magnification of the ion microscope based on the optical calibration of the immersion lens for various potentials. The potential of the first electrode is 600 V (retarding potential for the emitted particles). The parameter in this plot is the percentage of the emitter voltage at the unipotential lens center electrode. With both lenses (Figs. 30 and 31), a total magnification exceeding 1800 x is possible. By further decreasing the aperture of the unipotential lens, higher magnifications up to about 10^4 x are possible. For the experiments described in this report, two different unipotential lenses, both designed for minimum distortion, were used. Figure 35 gives a few examples of the surface image magnification in the light of cesium ion emission. Magnifications are between 129 x and 1170 x. The smaller magnifications cover only part of the phosphor area because of shielding by the unipotential lens. Reasonable operation is achieved at acceleration potentials between 5 and 7 kV. For this program the ion microscope served two purposes:

- Measurement of the electron work function of the emitter surface (including selective work function measurements on small patches) and quantitative measurement of ion currents from small areas

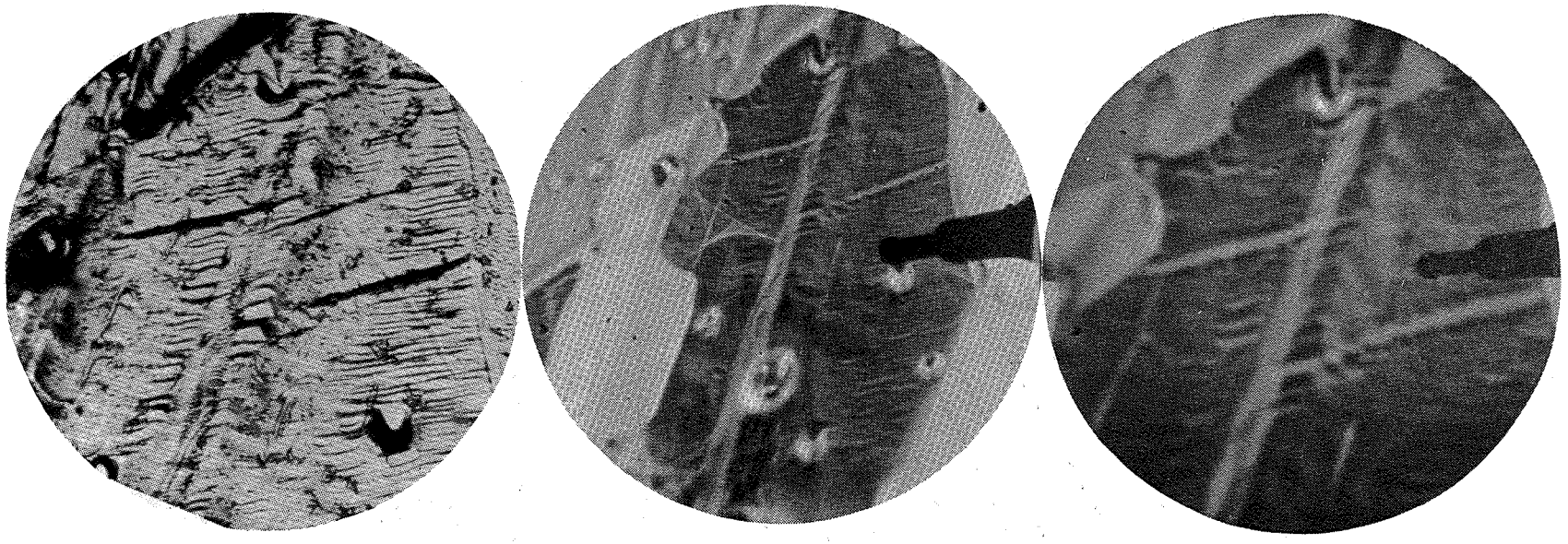

(a) (b) (c)

Fig. 33. Electron emission patterns (b) and (c) from a patchy pellet support made of molybdenum compared with a Bausch and Lomb metallograph picture (a). Note the low work function ripple in the high work function patch.

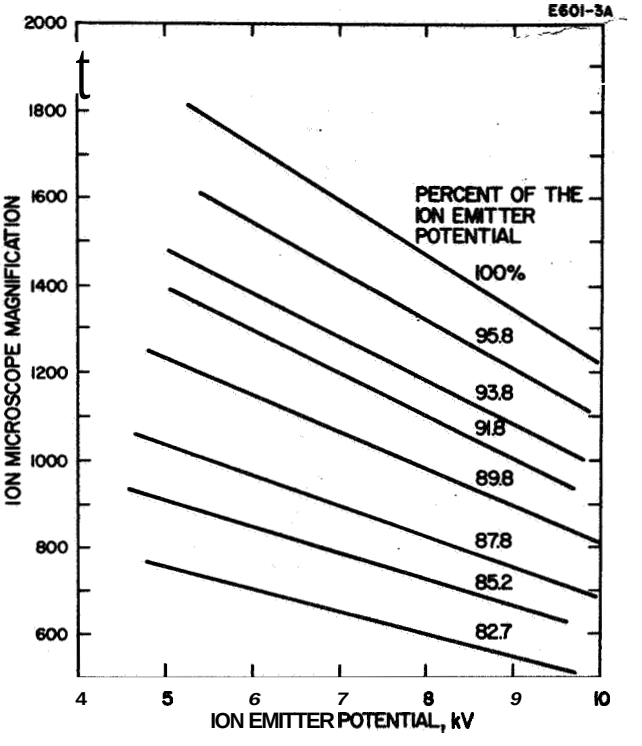

Fig. 34.
Ion microscope calibration curves. The immersion lens first electrode is at 600 V. Parameter is the unipotential lens potential in percent of the emitter potential.

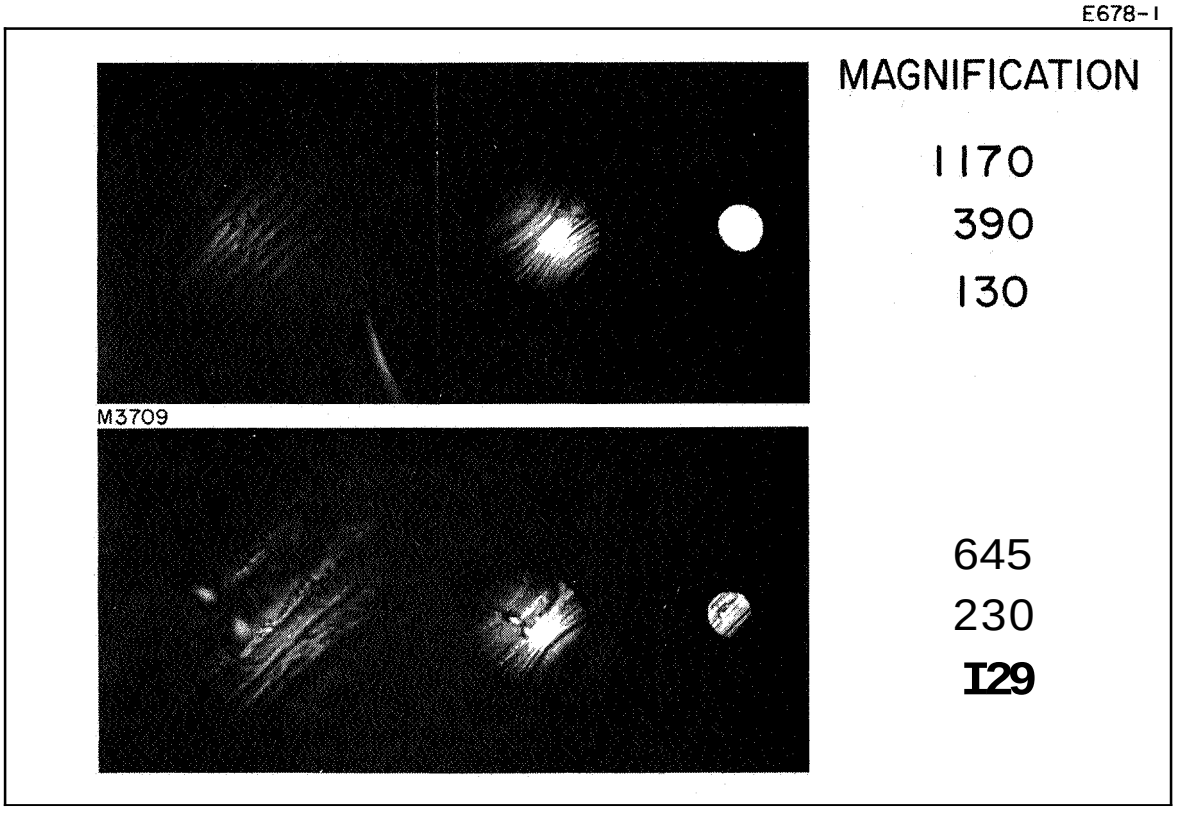

Fig. 35. Typical electron emission pattern from the molybdenum emitter support at various magnifications.

- Measurement of the cesium distribution around the pore exits and measurement of the surface migration length of cesium and other alkalis under consideration,

The phosphor allows visual observation of the emission pattern during emitter positioning, so that interesting emission zones may be measured with the Faraday cage. The Faraday cage is completely shielded to reduce noise background, and only a small circular 2 mm diameter inlet provides the current readings. A separate heater has been incorporated for re-evaporation of alkalies which condense on the supporting insulator. The Faraday cup is located immediately beneath the converter grid, and therefore the calibrated magnifications can be used for computating the current densities. Electron work functions up to 5.0 eV can be measured on small patches; higher work functions will require replacing the Faraday cage with an electron multiplier. At this time work functions higher than 5.0 eV can be measured only at low magnifications; therefore, they generally represent an integrated surface area. Such work function measurements are important because they indicate the surface condition (clean or contaminated).[1,38] As in previous work, thermionic emission data have been used for determining the cleanness of the emitter surface. This ion microscope is built as an ultrahigh vacuum system, equipped with a 200 liter/sec ion pump,. According to our standard techniques, the system is evacuated during baking with a mercury diffusion pump backed by a mechanical pump. A zeolite trap between the pumps prevents hydrocarbons from back-streaming into the vacuum chamber. The microscope is baked at about 200°C and the ion pump at a maximum of 150°C (ferrite ceramic magnets). After baking, the ion microscope is separated from the mercury-diffusion pump by an all metal valve. Only copper gaskets are employed.

A liquid nitrogen cold trap in the upper part of the microscope helps to reduce the alkali vapor pressure for ion emission studies. This low alkali vapor pressure is essential for proper operation of the converter unit.

The isolated emitter is mounted on a x-y table which is movable by micrometer screws. The alkali supply and the emitter are heated separately. There is no valve in the alkali fuel line; therefore, some alkali tends to come out of the pores even when electron emission is being studied. This alkali decreases the electron work function at the pore exits. A heat sink, connected to the emitter support base and cooled from outside the microscope, allows the fuel side to be maintained at a reasonably low temperature if necessary, Figure 36 shows the ion microscope mounted on the concrete base. It should be noted that the phosphor screen is usually observed visually; however, permanent photographic records can be taken by a polaroid camera mounted directly opposite the phosphor.

The ion emission pattern from a porous refractory metal surface is of considerable interest in connection with high ionization efficiencies required for ion propulsion systems. With a solid surface, alkali is deposited from the vapor phase, and there is statistically equal distribution of the alkali over the entire emitting surface; in contrast, on the porous surface the alkali is highly concentrated at the pore exits. Consequently, a porous rear fed emitter yields higher neutral efflux rates than the solid material at the same ion current density. Investigation of the neutral efflux rates on tungsten pellets with pore densities between 6×10^4 and 3×10^6 pores/cm^2 (traverse technique) showed that the pore density governs the neutral efflux (and not the pore diameter, as was assumed earlier by several authors).[1] Porous tungsten pellets currently are limited to about 3×10^6 pores/cm^2 (as measured by the traverse technique), even when coated with 2.4 μ spherical tungsten powder of narrow size classification, which is sintered to a density around 70% of theoretical.[40] The optimum pore density for various porous refractory metals and metal alloys (such as tungsten, rhenium, iridium, and W-25% Re) still must be determined. Here the alkali ion migration length radial to the pore exit is the important parameter, At about 10^7 (equally spaced) pores/cm^2, the available migration length

M 4156

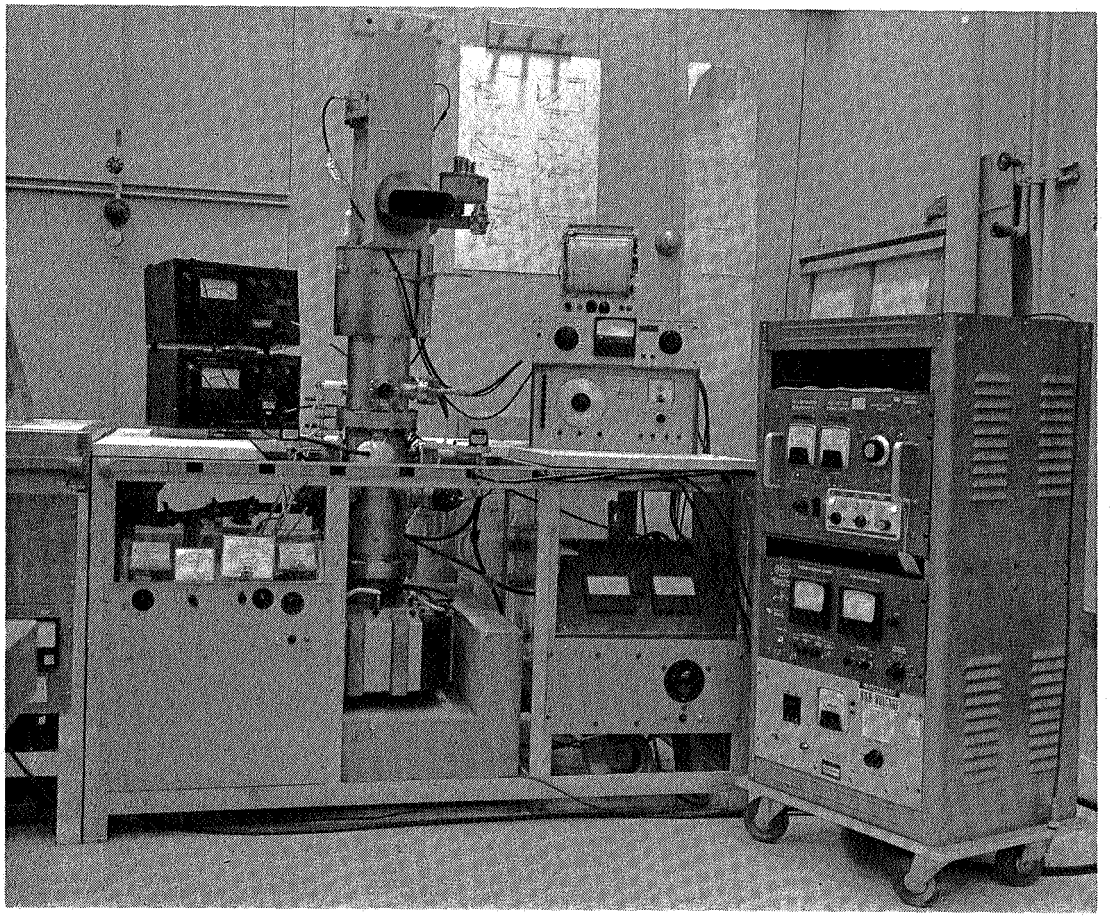

Fig. 36. Ion microscope mounted on concrete base.

(without interception with alkali from a neighboring pore) is 1.58 μ. For 10^4 pores/cm^2, 50 μ are available (see Fig. 37). The surface migration length L is proportional to the alkali concentration gradient $d\rho/dr$ and the temperature dependent diffusion coefficient D(T).

$$L \propto \frac{d\rho}{dr} D(T) \quad . \tag{31}$$

As a first order approximation, it is assumed that the alkali distributes equally around the pore exit with no preferential sites. Consequently, the concentration decreases proportional to 1/r. The surface diffusion activation energy is low – about 11.5 kcal/mol. The 1/r decrease of the alkali concentration is combined with the effect of alkali evaporation. At the center of the alkali supply the surface coverage is high and the heat of evaporation of cesium from cesium is reported to be 16.1 kcal/mol, considerably below that for cesium ions (44.8 kcal/mol at low surface coverage).[19] The heat for cesium atom evaporation at low surface coverage is about 52.8 kcal/mol.[59] It is difficult to estimate the surface migration length radially from the pore exit because the concentration gradient changes strongly, and atom and ion migration lengths are involved, The migration length is best measured in situ with the ion microscope, as in the experiment. As has been pointed out, the concentration decreases more steeply than 1/r, and therefore the emission center radii must be measured according to varying exposure times. Instead of using the meaningless dimension of the pore radius, the emission center radius is used (1) because it is the dimension under observation, and (2) because the pore radii are statistically distributed and usually cover a fairly wide range; their influence on the emission center radius is questionable.[1] The emission center radius depends directly on the flow rate per pore, and emitter temperature.

According to the Saha equation, the ionization efficiency depends exponentially on the difference between the work function and the ionization potential. For a bulk contaminant the work function is usually lower

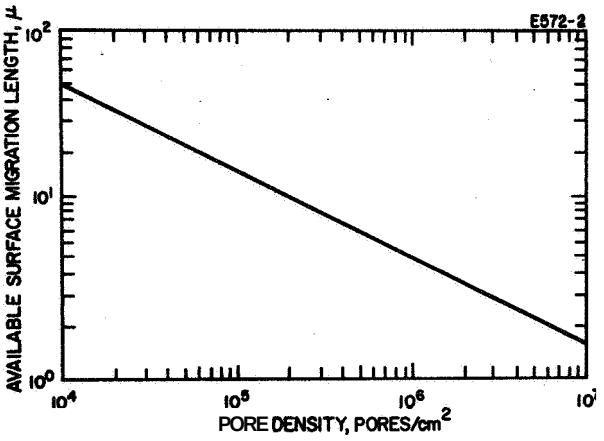

Fig. 37.
Available surface migration length as a function of pore density.

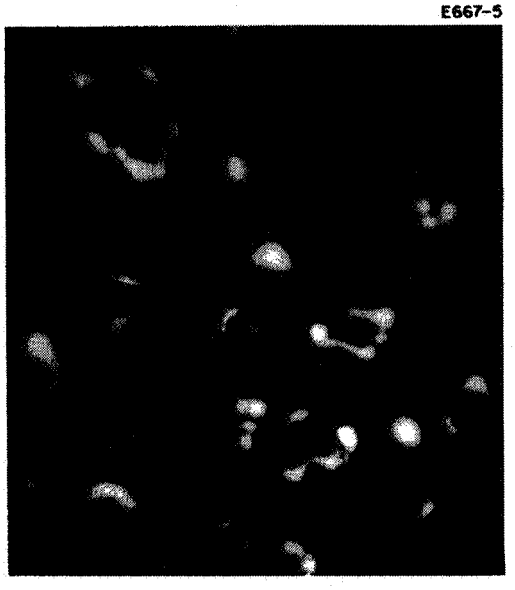

Fig. **38.**
Electron emission from sputter deposited molybdenum after about 3 days operation at 1750°K. The crystal facets are partially cleaned up, as indicated by the dark inner area.

than that measured on the clean surface. In the presence of oxygen or water vapor, however, the work function exceeds that of clean tungsten. (For space flight neither case is interesting because these contaminants are not present in space. Therefore, we refer here to the clean polycrystalline surface.) In case of gas adsorption on the emitter surface, cleanup is achieved by heating to sufficiently high temperature;[38] e. g., to 1800°K in case of oxygen adsorption.[27] Small amounts of cesium hasten, this cleanup at temperatures in the 1600°K range,

For bulk contaminants, the volume diffusion must be considered. As an example of such cleanup, a photograph from sputter deposited molybdenum is presented (see Fig. 38). The surfaces of all crystal facets have the same work function, and therefore the cleanup pattern of these 20 mil thick crystals provides a good example, Cleanup is indicated by the change of the thermionic work function. The first work function measurements on these crystal facets taken over a wide temperature range, gave **3.1** eV, as computed from the Richardson plot. At a given temperature, all crystal facets show the same brightness. Partial cleanup was achieved very slowly, over a few days, while the emitter was kept at 1750°K. During this phase, the electron emission pattern from the facets changed. Instead of an equal brightness over the whole facet (about 20 by 20 μ square surface), the central section developed a higher work function and consequently became darker. The bright zone around this part can be seen in Fig. 38; this is characteristic for the entire sputtered molybdenum surface, During continued heating the bright facet rim disappeared and the work function increased further. Curves I, 11, III, and IV of Fig. **39** were measured sequentially. Curve V was measured on a patch of the pellet support, which is made of molybdenum. Finally, the work function stabilized at 4.2 eV (curve IV) after more-than a week at 1750°K. Work functions between 4.15 and 4.44 eV have been reported for molybdenum.[55,56] The accepted value for the polycrystalline surface is 4.24 eV (Ref. 56). There is little information available on the work function of single crystal molybdenum. Figure 40

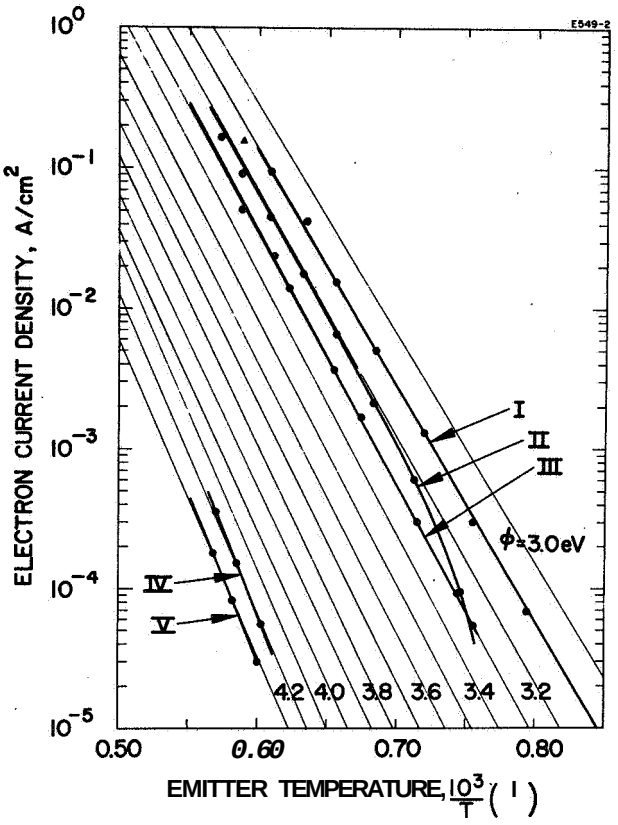

Fig. 39.
Richardson work function measurements on patches of molybdenum sputter deposited on porous tungsten. Curves I, II, 111, and IV were measured sequentially and illustrate the cleanup of the surface. Curve V was measured on a patch of the pellet support which is made of molybdenum,

E667-6

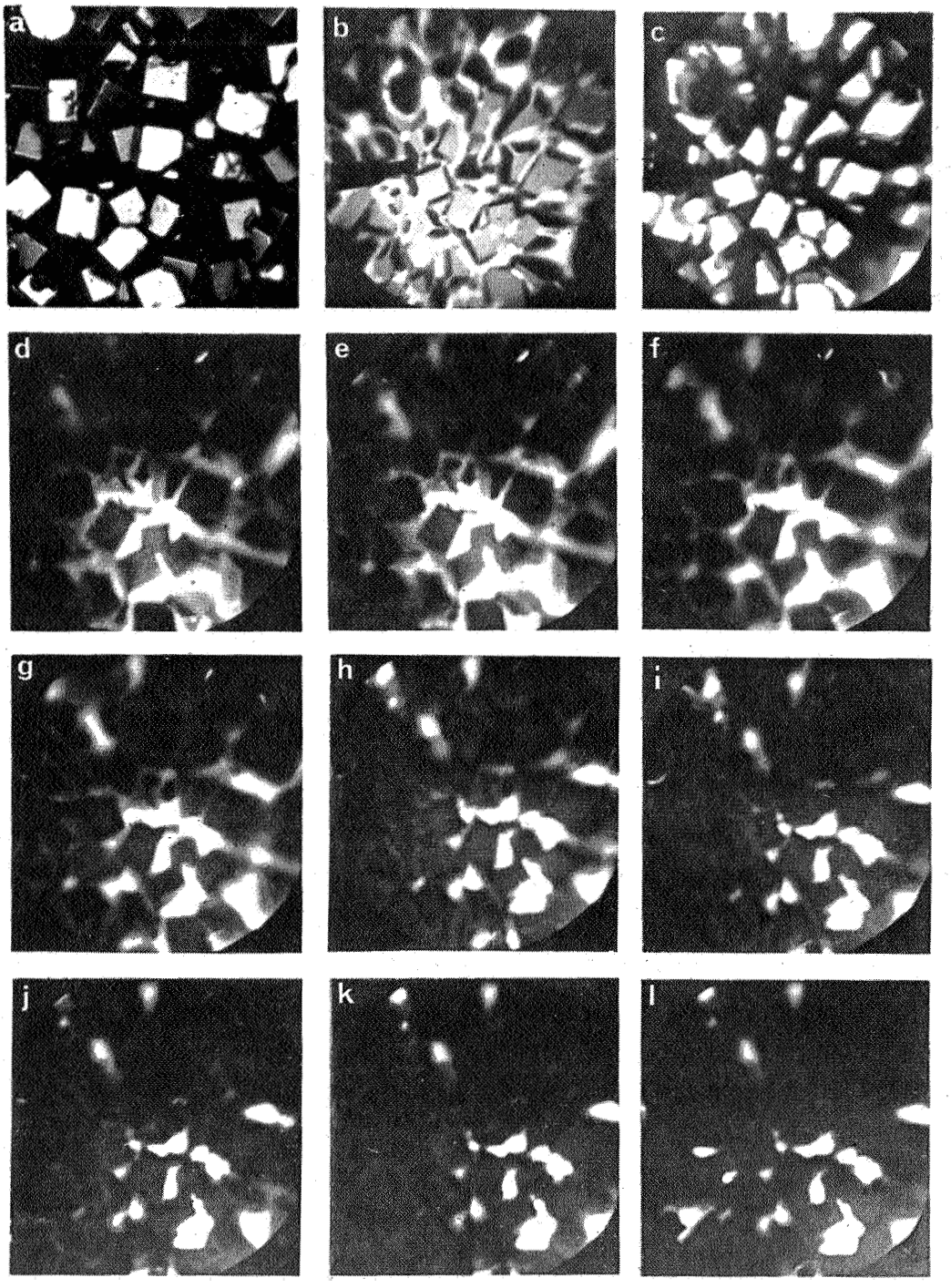

Fig. 40.
Emission characteristics of sputter deposited molybdenum. The magnification is 400x and (a) is the optical image of the same surface area shown in the pictures (b) through (1). (b) is the electron emission pattern, and (c) through (1) represent the ion emission pattern with increasing temperature in the same sequence. (c) was taken in the threshold region of surface ionization. The patches in (b) show the same brightness over the entire emitter area and consequently indicate one thermionic work function.

shows a number of photographs of the sputter-deposited molybdenum surface, with the crystal facets. Figure 40(a) is an optical view at 400 x magnification. Figure 40(b) shows this same area, in this case in the light of electron emission from the emitter surface. Note the same brightness of all crystal facets and the increased brightness in between; this increase results because of cesium diffusion and the lowered work function at the pore exit. Figure 40(c) through 40(ℓ) were taken in the light of cesium ion emission. In Fig. 40(c) the crystal facets are bright and the areas in between dark, because of excessive cesium accumulation. This image was taken in the threshold region for cesium surface ionization. The remaining images, Fig. 40(d) to 40(ℓ) were taken in the saturation range of surface ionization; therefore, the ion emission from the areas around the pore exits is predominant, and almost no cesium diffuses over the crystal facets. All photographs were taken of the same emitter area. In the saturation range, the ion emission center diameter shrinks at constant cesium flow rate with increasing emitter temperature (compare Fig. 40(d) with 40(ℓ)). Table V gives the emitter temperatures and exposure times for Fig. 40. The exposure time for Fig. 40(c) is **30** times that of the other photographs, and was taken in the ion emission threshold range. (Polaroid 200 speed Pan film was used.) Double images at the periphery are visible in Fig. 40. (Fig. 40(d) through 40(ℓ). Because ions are extracted from only a very small area, part of the evaporated cesium is intercepted by the molybdenum electrode opposite the emitter; this cesium on the electrode is re-evaporated onto the emitter with statistical distribution, rather than accumulating around the pore exit. The cesium surface coverage on the remaining large emitter area, not shown in Fig. 40, exceeds one monolayer of cesium atoms (note the positive ion retarding potential applied to the first electrode—see Figs. **28** and 29).

Ion microscope investigation of cesium ion emission from porous tungsten under clean surface conditions yielded surprisingly small surface migration lengths. The steep changeover from low to high ion currents in the threshold temperature range for surface ionization was measured with the built-in Faraday cage.

It was reported earlier that in case of emitter surface carburization, a smooth rolling over from low to high ion currents was observed.[26,38] Investigation of a contaminated tungsten pellet with the ion microscope yielded similar results which are presented here as a typical example.

TABLE V

Emitter Temperatures and Exposure Times for Ion Microscope Photographs of Surface Ionization on a Porous Tungsten Emitter

Figure Number	Exposure Time, sec	Emitter Temperature, °K
40(c)	150	1047
40(d)	5	1063
40(e)	5	1090
40(f)	5	1143
40(g)	5	1207
40(h)	5	1320
40(i)	5	1432
40(j)	5	1513
40(k)	5	1630
40(l)	5	1742

A tungsten pellet with 3.75 eV thermionic work function measured over a large area of the emitter surface by means of the Faraday cage, yielded relatively small migration lengths at temperatures more than 100°K above the critical temperature. The single pore under investigation showed a somewhat higher cesium flow rate than the other pores. The exposure times and emitter temperatures for a series of photographs of this pore (Fig. 41(a) through (j)) in the ion emission phase are given in Table VI. The emission center radius decreases significantly between 1000°K and 1104°K. In Fig. 42 the ion current (curve B) and the ion

TABLE VI

Emitter Temperatures and Exposure Times
for Ion Microscope Photographs

Figure Number	Emitter Temperature, ^{o}K	Exposure Time, sec
41(a)	1000	120
41(b)	1015	60
41(c)	1052	30
41(d)	1080	30
41(e)	1104	30
41(f)	1183	25
41(g)	1261	20
41(h)	1336	20
41(i)	1425	30
41(j)	1581	30

current density (curve **A**), as measured with the Faraday cage for the emission center shown in Fig. 41 are plotted with $\phi = 3.75$ eV. Curve A represents the decreasing ion current density with emitter temperature. In contrast to the ion current density behavior on the clean tungsten surface (with a steep changeover from low to high ion current density) a smooth rolling over is observed here, with no clearly defined threshold temperature. The data plotted in Fig. 42 were taken at a higher ion current density than the series of photographs in Fig. 41. The ion current profile through the ion emission center close to threshold temperature is also shown in Fig. 42. Profiles crossing perpendicularly are very similar and show an ion current minimum in the middle, as expected with a cesium overload. The ion current minimum in the center apparently was lower than indicated in the graph. The average ion current per pore (curve B of Fig. 42) increases slightly with decreasing emitter temperature,. as expected from the $T^{-1/2}$ dependence (straight line) of the cesium flow rate through the porous pellet. In Fig. 42 the

E560-6A

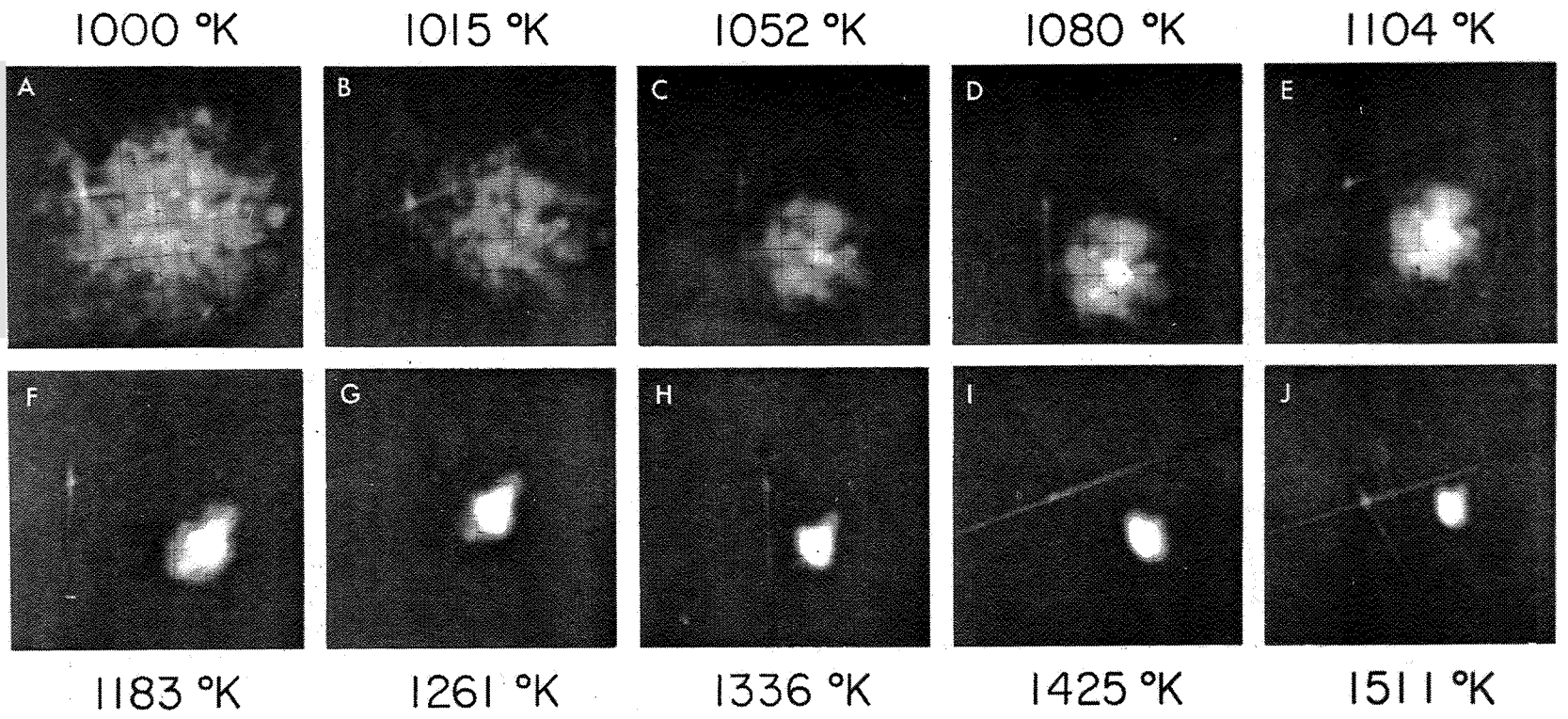

Fig. 41. Cesium ion emission from a single pore on porous tungsten observed over a temperature range of 1000 to 1581°K in the sequence (a) to (j) (see Table VI). The work function is 3.75 eV, indicating a contaminated tungsten surface.

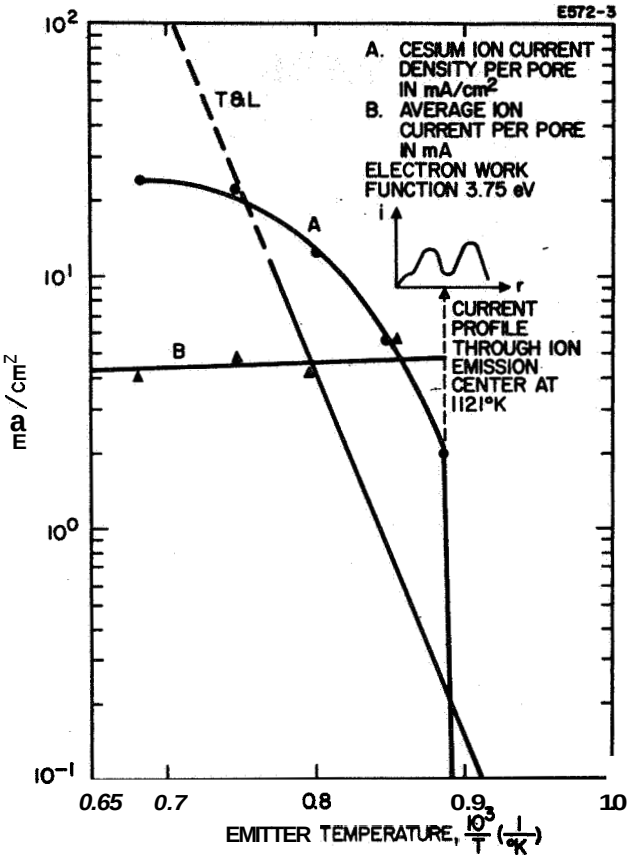

Fig. 42.
Ion microscope studies of ion emission from a single pore. Curve **A** represents the ion current density and shows 24 mA/cm^2 in the high temperature range, smoothly rolling over to lower current density with decreasing emitter temperature. The surface contamination is confirmed by threshold temperatures below that of tungsten (T and L line). The thermionic work function is 3.75 eV. Curve B shows the expected increase of the ion current according to the $T^{-1/2}$ dependence of the cesium flow rate.

critical temperature for solid tungsten is added and, with the work function measurement, indicates a contaminated surface of lower work function than that of tungsten. Obviously, this surface is not carburized; for a carburized surface, we measured increased critical temperatures compared with tungsten.[26] The ion current density per pore reaches 24 mA/cm^2, explaining the increased neutral efflux relative to that from vapor deposited cesium (magnification is 1250 x).

If Fig. 41 is observed closely in the low temperature range (Fig. 41(a) through (d)), dark areas can be seen-between the bright spots. The distinctive pattern in Fig. 41(b) through (d) makes it possible to follow the development of these dark areas. They do not show any crystal shapes, eliminating the possibility of a low surface work function patch. It must be assumed that the dark areas are overfed with cesium. According to Table VI, the images shown in Fig. 41(a) and (b) have, respectively, four times and twice the exposure time of the remaining photographs. It is clear that Figs. 41(a) and (b) were taken in the threshold region for surface ionization.* A plot of the surface migration length (the radius of the ion emission center) is shown in Fig. 43. Two different modes of surface migration are observed: (1) In the high temperature range (1250 to 2000°K), the surface migration length is no more than a few microns. This migration length L is expressed by $\log L = (3.54 \times 10^2/T) - 3.782$. (2) In the temperature range below 1200°K, and with the same cesium flow rate (increased only because of the $T^{-1/2}$ dependance), the migration length increases; below 1200°K the surface migration length L is expressed by $\log L = (3.5 \times 10^3/T) - 6.32$, (cm). At low surface coverage, i.e., at temperatures above 1250°K, the temperature dependent surface diffusion coefficient is expressed by $\log D(T) = -(9132/T) + 4.192$ ($cm^2\ sec^{-2}$) as obtained from

$$L = \left(D(T) \times \tau\,(T)\right)^{1/2} \qquad \text{(cm)} \qquad (32)$$

*Note the smooth rolling over from low to high current density. Figure 42, curve A.

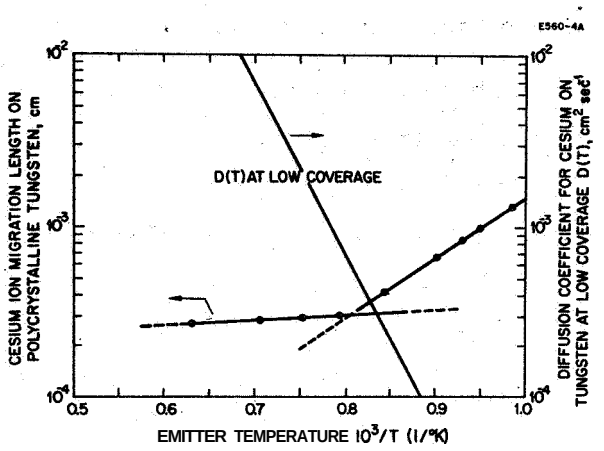

Fig. 43.
Ion migration length and diffusion coefficient at low coverage for cesium on contaminated polycrystalline tungsten. ϕ = 3.75 eV.

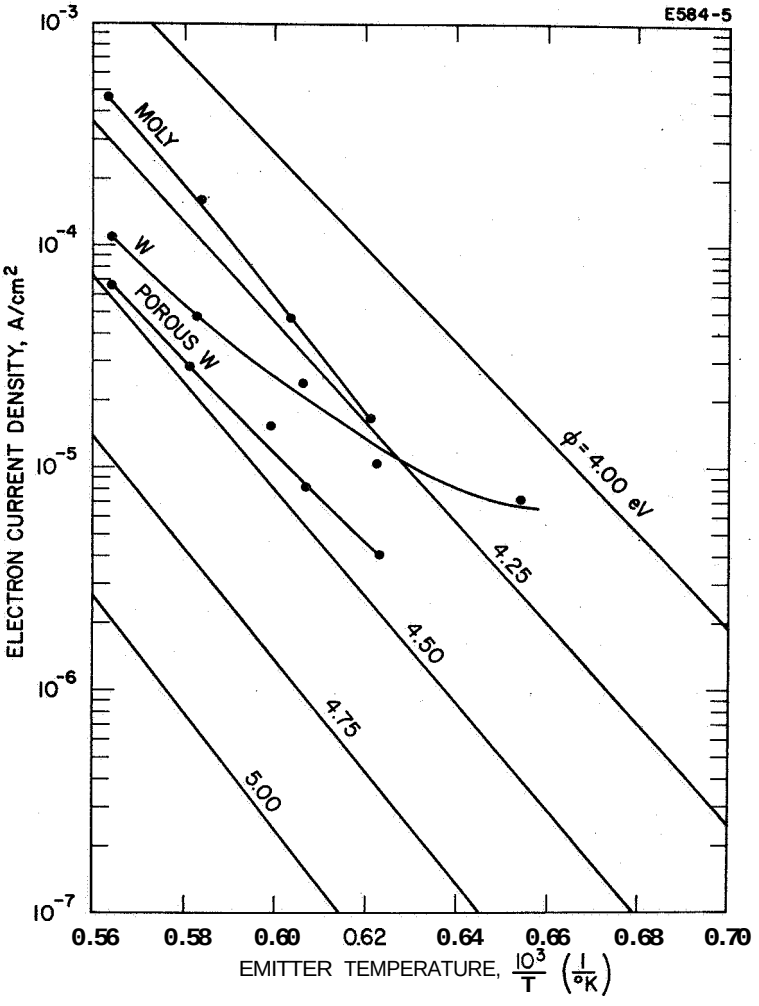

Fig. 44.
Tungsten pellet cleanup, measured with the ion microscope Faraday cage.

with $\tau = 1.77 \times 10^{-12} \exp(11600/T)\, Q_i$ (ref. 19). For clean polycrystalline tungsten $Q_i = 1.95$ eV, as reported earlier.[19] In connection with the threshold temperature measurement (Fig. 42), the alkali ion desorption energy is lower than that measured for clean tungsten.

After slow cleanup for more than a week, the work function reached 4.29 eV and finally stabilized at 4.45 eV (see Fig. 44): A number of photographs (Fig. 45) were taken at 1410 x magnification for emitter temperatures from 1131 to 1430°K. Exposure times and magnifications of these photographs are given in Table VII. The photographs (Figs. 45(a) through (f) make it evident that the surface migration length in this case is in the 2 μ range (the emission center radius) and is only slightly dependent on the emitter temperature. As would be expected because of the 1/r dependence, the ion emission decreases strongly toward the rim of the emission center. For Fig. 45(b) the expose time was doubled; the emission center expands slightly, but the expansion is very limited because of the greater than 1/r decrease of the ion emission center radius (see Fig. 46). In Fig. 46 the ion current is plotted versus emission center radius with the surface coverage increasing toward the center.[57] With a further decrease in the emitter temperature we expect further expansion of the emission center, with a circular dark area developing in its center and expanding with decreasing temperature. The bright ion emitting ring surrounding the dark area then can be explained by the thinning out of the alkali concentration.

Fig, 45(a) was taken close to the threshold of surface ionization. If the measured surface migration lengths are projected into Fig. 37, it shows, for equally spaced pores and 2 μ migration length, that 6×10^6 pores/cm^2 would be the optimum pore density. If the decrease of surface coverage at the emission center rim is considered, the pore density should actually be higher; 10^7 pores/cm^2 should be adequate. In this case, the ion emission centers partially overlap; better use of the available surface is achieved, as is important with respect to the radiation losses.

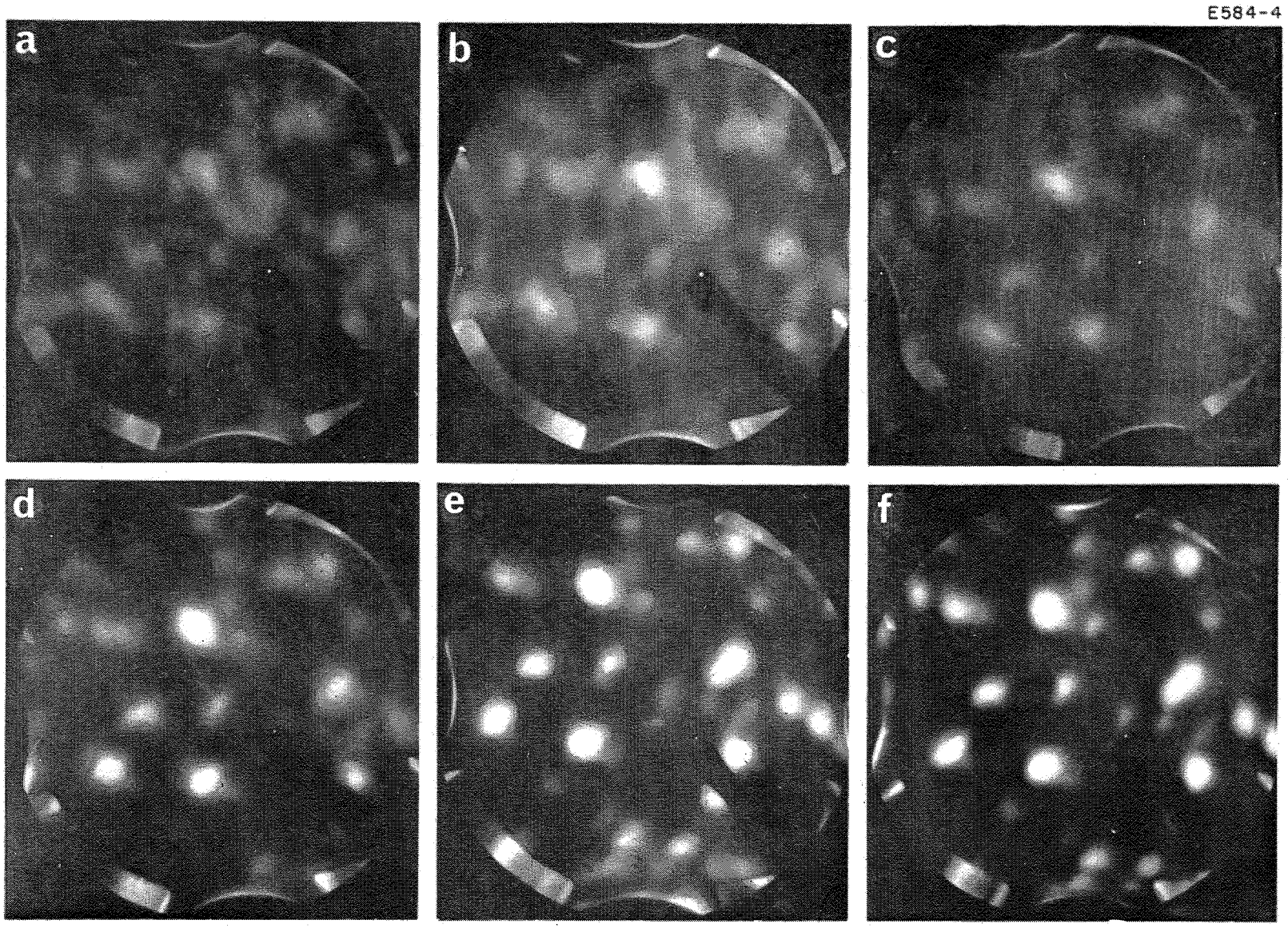

Fig. 45. Cesium ion emission from a clean porous polycrystalline surface with increasing temperature from (a) to (f). The cesium flow rate is constant. The exposure time of (b) is twice that of the other pictures. (See Table VII).

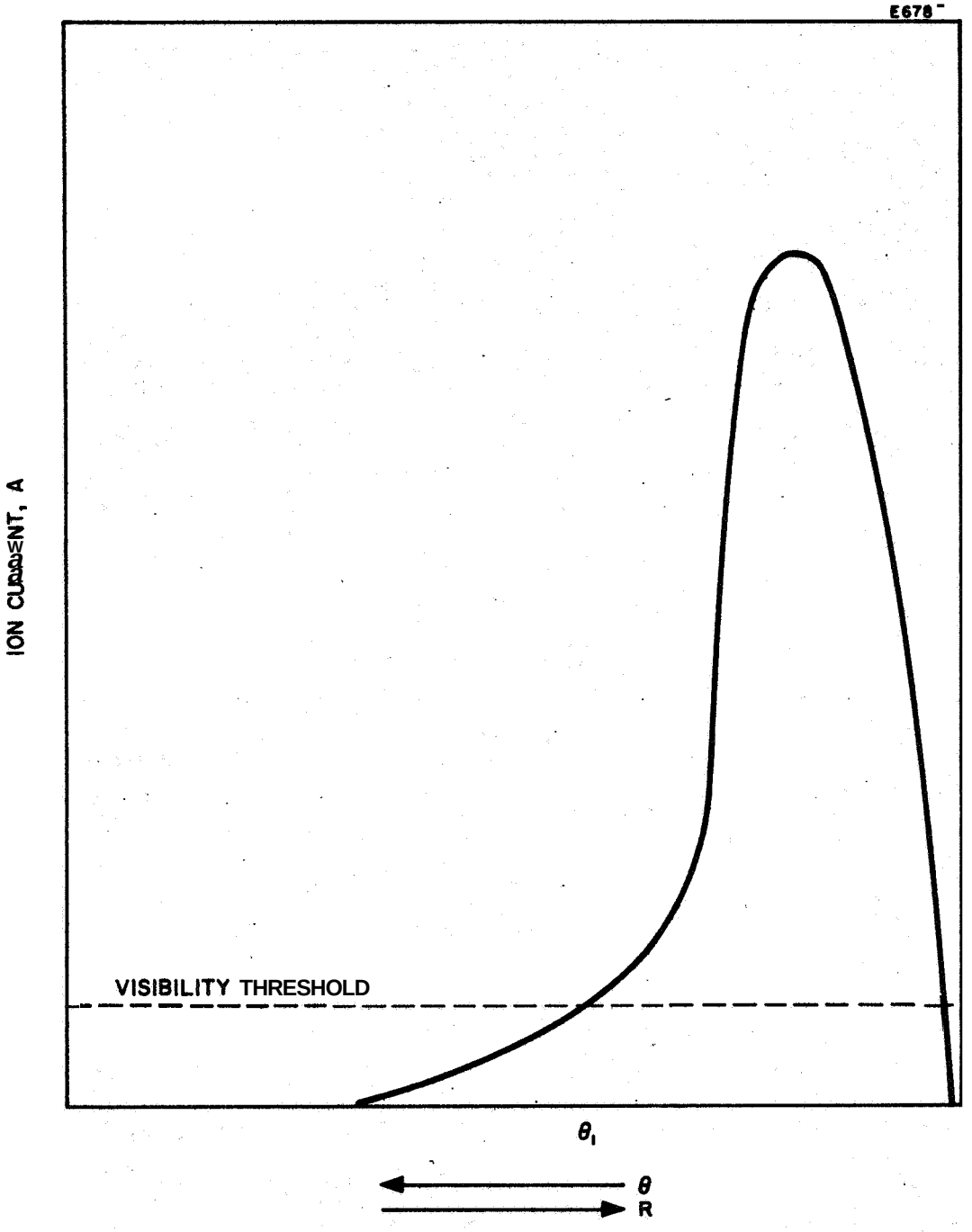

Fig. 46. Cesium ion current dependence on the distance from the alkali supply center. θ is the surface coverage relative to a monolayer and R is the emission center radius. The middle area is covered with excessive cesium and therefore does not contribute to ion emission. Only the outer ring contributes to ion emission, as is shown in the graph.

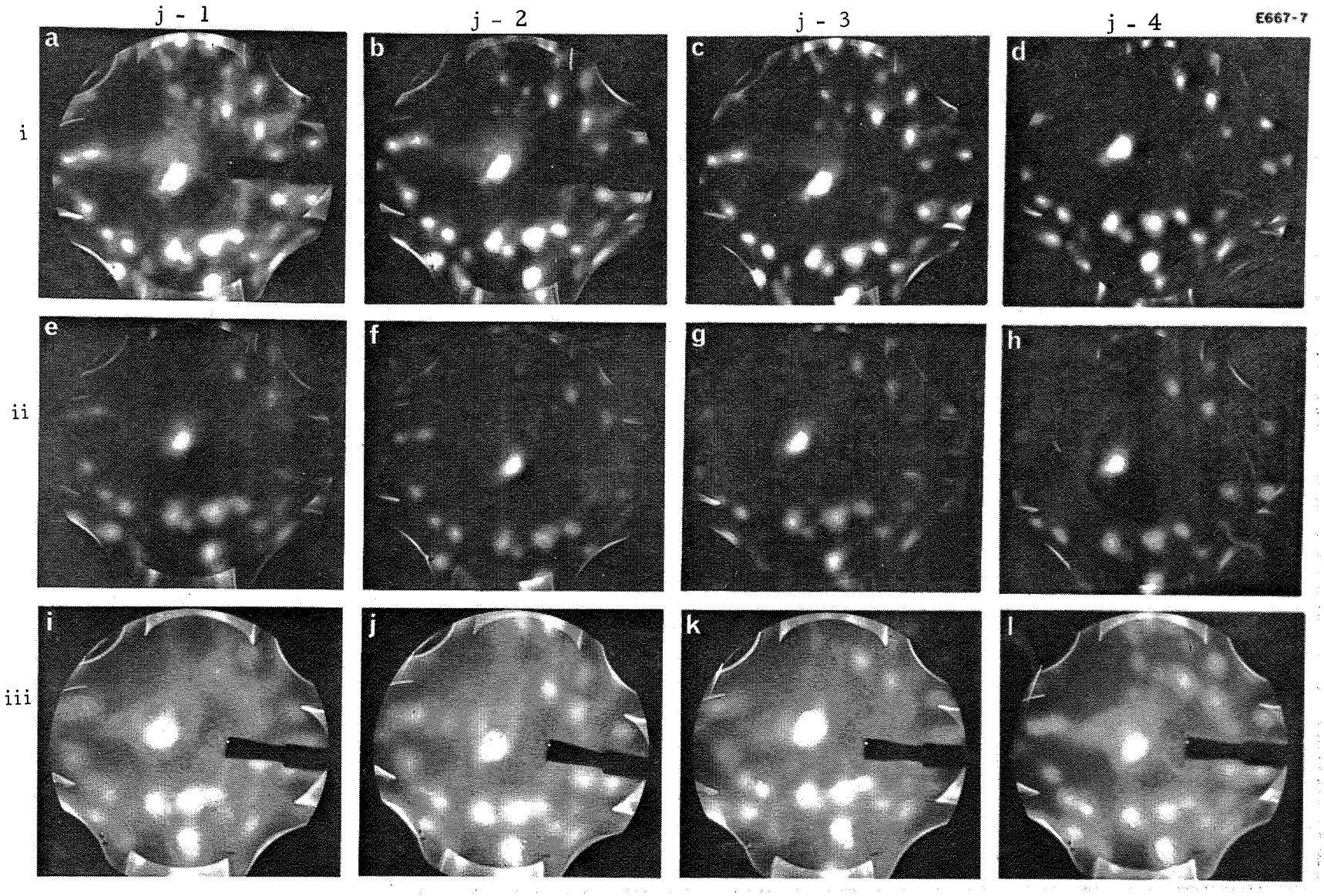

Fig. 47. Ion emission from clean porous tungsten for three cesium flow rates increasing from line i to line iii. The emitter temperatures increase from j - 1 to j - 4. Here it becomes clear that the emission center radius is not very much affected by either the emitter temperature or the cesium flow rate.

TABLE VII

Exposure Times and Emitter Temperatures
for Ion Microscope Photographs

Figure Number	Exposure Time, sec	Emitter Temperature, ^{o}K
45(a)	0.5	1131
45(b)	1.0	1156
45(c)	0.5	1192
45(d)	0.5	1252
45(e)	0.5	1324
45(f)	0.5	1450

Under clean surface conditions, the emission center radius is not strongly dependent on the ion current density. These series of emitter photographs are presented in Fig. 47. Here the magnification is kept constant, and all photographs are taken with f = 1.9. Figure 47(a) through (1) show the same emitter area for three different flow rates. If the pictures in a single row are compared, a fairly constant spot size appears despite the steeply increasing cesium flow rate in the lower photographs. The different exposure time may contribute somewhat to the emission center size; however, if the results at emitter temperatures above 1400^{o}K are compared, there is very little change in size. Furthermore, we know that the emission center does not expand very strongly above the visible size because of the steep decrease of the ion current density at the rim (Fig. 46).

All emission centers have nearly the same diameters, indicating only small differences in the alkali flow rate per pore. The cesium reservoir temperature (see Table VIII) was measured on the emitter support and is not necessarily the accurate reservoir temperatures; however, it represents a good indication of the relative change of the

alkali vapor pressure. As was pointed out earlier, the ion desorption energy also depends on the applied electric field. The desorption energy due to this field is reduced, with

$$- dQ_i = e(eE)^{1/2} \tag{33}$$

TABLE VIII

Exposure Times, Emitter Temperatures, and Cesium Reservoir Temperatures for Ion Microscope Photographs

Figure Number	Exposure Time, sec	Emitter Temperature, ^{o}K	Cesium Reservoir Temperature, ^{o}C
47(a)	4	1240	85
47(b)	4	1315	80
47(c)	4	1381	75
47(d)	4	1435	70
47(e)	1	1240	140
47(f)	1	1322	145
47(g)	1	1379	145
47(h)	1	1450	145
47(i)	1	1238	180
47(j)	1	1320	180
47(k)	1	1392	180
47(l)	1	1474	180

Tank studies were made of the electric field at a model emitter surface (magnified 50,000 x), with pores of 1 μ diameter,, 2 μ separation, and 1 μ pore depth (Fig. 48). With 7 kV applied, the field at this emitter surface was 13 kV/cm. In the pore center the field was 1.4 kV/cm and close to the pore rim increased to 10 kV/cm. At the pore rim, this field may reach 10^5 V/cm if the rim has a sharp corner,

However, as the sharpness of the corner increases, its area, and therefore its contribution to the ion current decreases. Therefore, with regard to the surface area under consideration, we can conclude that the average field at the emitter surface does not exceed 13 kV/cm.[19] Consequently, the decrease in cesium ion desorption energy is $-dQ = 0.044$ eV. The above electric field eliminates the effect of patch fields, as shown in Fig. 49. Here a field of 8 kV/cm is superimposed **over** the patch surface (normalized here) with a work function difference of 1.0 eV.[19]

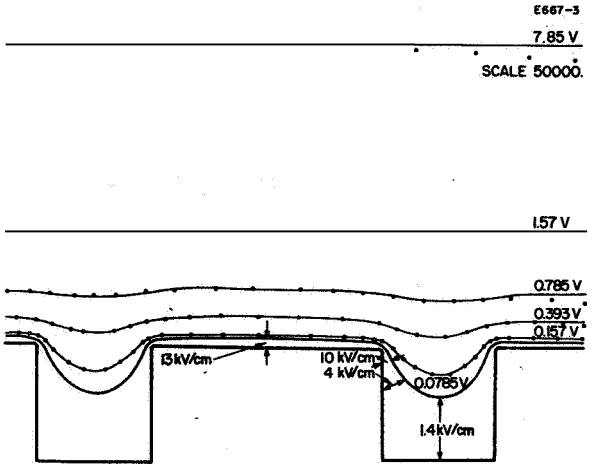

Fig. 48. Equipotential lines above an idealized porous emitter surface with 2 μ pore spacing and 1 μ pore diameter and pore depth. The applied potential is 10 kV. A Pierce gun configuration is used. The actual potentials and fields are indicated.[19]

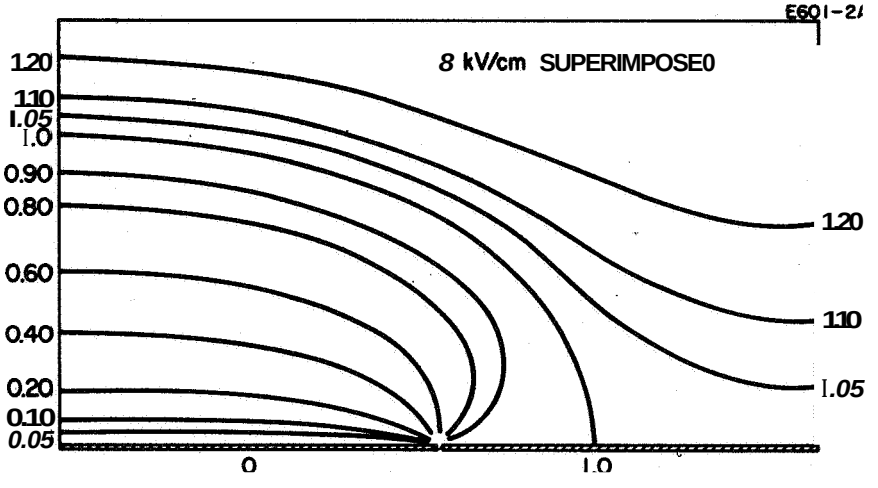

Fig. 49. Equipotential lines on a patch surface with normalized work functions. A field of 8 kV/cm is superimposed.

SECTION V

AVERAGE CESIUM ION SURFACE LIFETIMES ON SINGLE CRYSTALS

The experimental equipment for ion surface lifetime and ion desorption energy measurements was completed during the last quarter of this contract. In this program we have concentraied on the single crystal ion desorption energies instead of the polycrystalline surface.[19] The binding force on a surface of known structure is expected to be easier to interpret; furthermore, the relationship between the electron work function and the binding energy, as given in the Schottky equation, should yield the ionization activation energy term. Based on our knowledge of desorption energies on various crystal faces of one metal and the face distribution function, the desorption energy for the polycrystalline surface can be computed.

In the experiments reported here, single crystal tungsten was used first because the electron work function for the main crystal surfaces is known[13,31] (see Table IX),

TABLE IX

Tungsten Single Crystal Work Functions

	ϕ_R	A_R
(111)	**4.38**	52
(112)	4.65	120
(116)	**4.** 29	40
(100)	4. 52	105
(110)	5. 05	100

According to G. F. Smith (private communication), the work function for W(110) is about 5.20 V, according to Hopkins, et al., it is 5.05 eV.[56(a)] The pulsed atom beam technique is used for measuring the average surface lifetimes and ion desorption energies. Cesium atoms are evaporated from a standard ion gun with a porous pellet surface but with the emitter temperature below the ionization threshold. The cesium atoms pass through a shutter which is rotating at about 5500 rpm; this shutter has two apertures, each covering 30^{o}. The atomic beam then passes through the collimator of a neutral detector, and the atoms are ionized on a single crystal surface mounted perpendicular to the atomic beam inside the LN_2 cooled detector. The ion current between the heated single crystal and the surrounding ion collector is measured. The single crystal is radiation heated and the temperature is measured with a pyrometer, taking into account the spectral emissivity and the window corrections (see Fig. 50).

Adsorption;

$$j_i = A \exp - B \left(1 - \exp - \frac{t}{\tau}\right) \tag{34}$$

Desorption[56(b)].

$$j_i = A \exp - B \left(\exp - \tau_1 + \tau_2\right) \tag{35}$$

$$A \tau \frac{n_o}{\tau_{oi}} \exp - \frac{Q_i}{kT} \tag{36}$$

$$B = \frac{n_o \gamma_i}{kT} \tag{37}$$

Figure 51 shows various pulse shapes registered with an oscilloscope across a 30 kΩ inductance free resistor. The parameter of the curves is $B = n_o \gamma_i / kT$, with n_o the number of atoms arriving. γ_i is a constant.

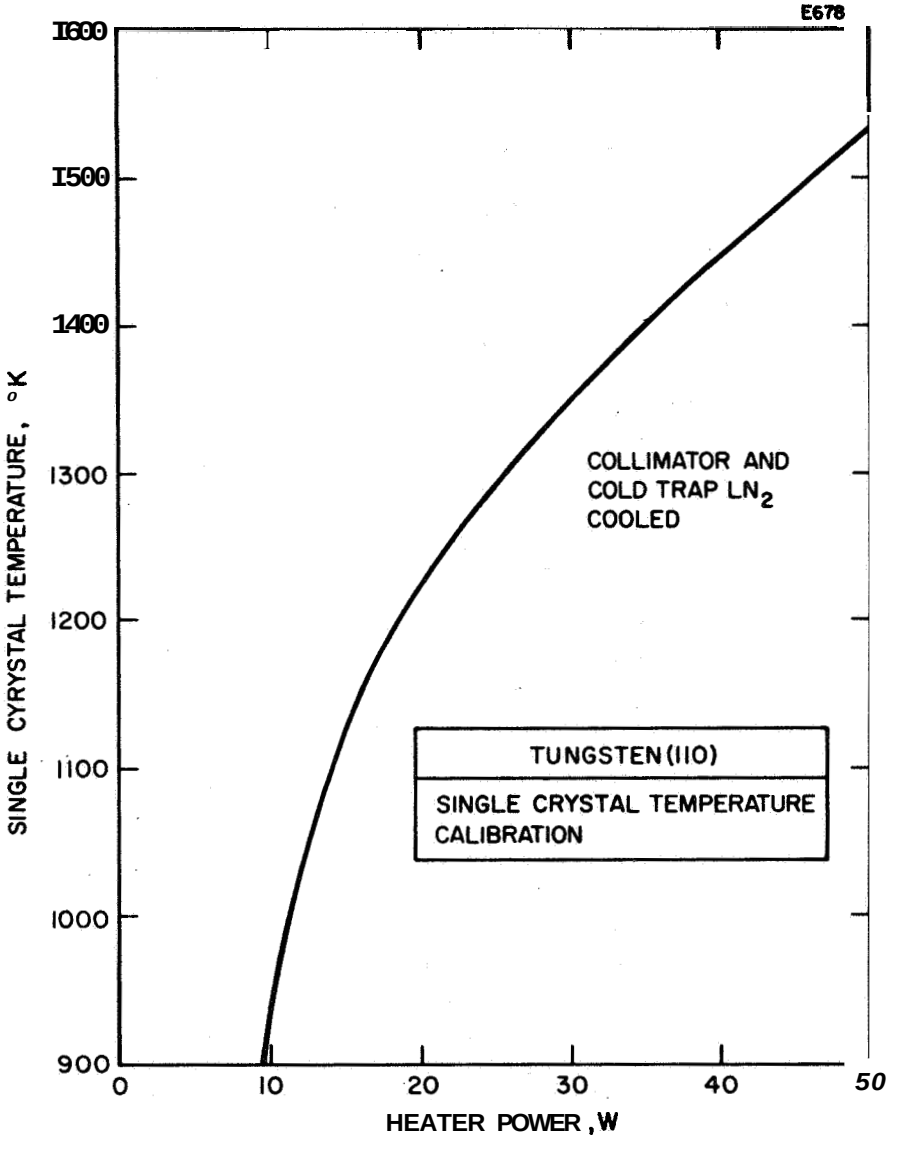

Fig. 50. Tungsten single crystal temperature calibration.

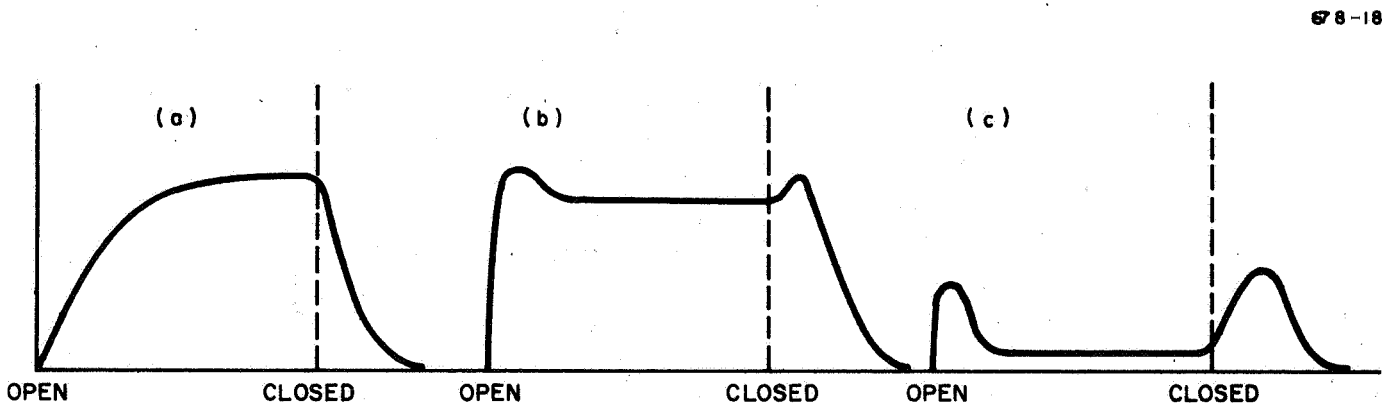

Fig. 51. Surface lifetime experiments with a chopped cesium atom beam. (a) represents the normal condition, while in (b) and (c) the surface is overfed with cesium. After the shutter is closed, all three graphs show the exponential decay from which the ion desorption energy is computed.[56b]

For B = 0 (Fig, 51(a)) we register the exponential increase of the ion current with time (abscissa) from the shutter opening to its closing, and from there on the exponential decay of the ion current density caused by depletion of cesium from the single crystal surface. In Fig. 51(b), B = 1. 5, indicating a higher atom flux to the ionizer surface. Because of excessive coverage, the ion current stabilizes during the time the shutter is open, with atom influx and atom evaporation in equilibrium; after the shutter closes, the ion current decays exponentially after an initial slight increase. In Fig, 51(c), the ionizer surface is flooded with cesium; because of excessive coverage (more atom evaporation than with B = 1. 5) during the open time, the ion current is fairly small; it increases due to surface cleanup after the shutter closes, reaches a maximum, and then begins decaying exponentially. These curves follow eqs. **(34)** through **(37).** The experiment was set up in one of the glass cross tubes (described earlier)[39] used previously for measuring the neutral efflux from porous refractory metal pellets. Ultrahigh vacuum conditions (low 10^{-9} scale) were maintained, and the single crystal tungsten surface was cleaned according to our standard procedure.

The single crystal surfaces were cut from a Linde tungsten single crystal which is 1/2 in. in diameter and 2 in. long. The orientation of this crystal was determined by x-ray techniques, taking both the Laue and the Debye-Scherr diagrams. The latter diagrams (Fig. 52) were recorded with a Geiger counter. In our first experiment we intended to achieve a (110) cut; For this purpose the cut must be within 0. 1^{o} or better, which is quite difficult with a hard metal such as tungsten. The first cut did not achieve this orientation; the Debye-Scherr diagram indicates in addition to the (110) surface, some (200) and to a smaller degree (211). This is confirmed by the Laue diagram (Fig. 53). Accurate adjustment of the surface plane is difficult and time consuming.

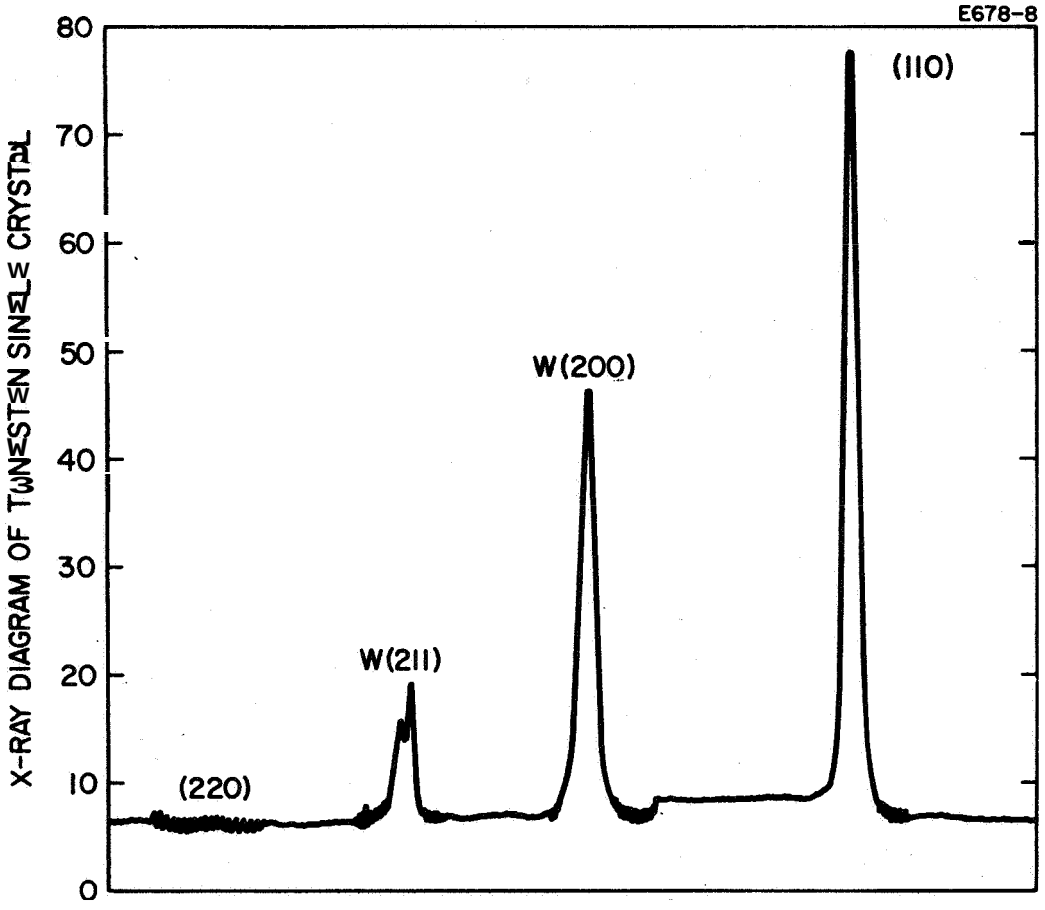

Fig. 52. X-ray diagram of tungsten single crystal. This cut was not well enough aligned, but yielded mainly the W(110) surface with some percentage of the (200) and (211) orientations.

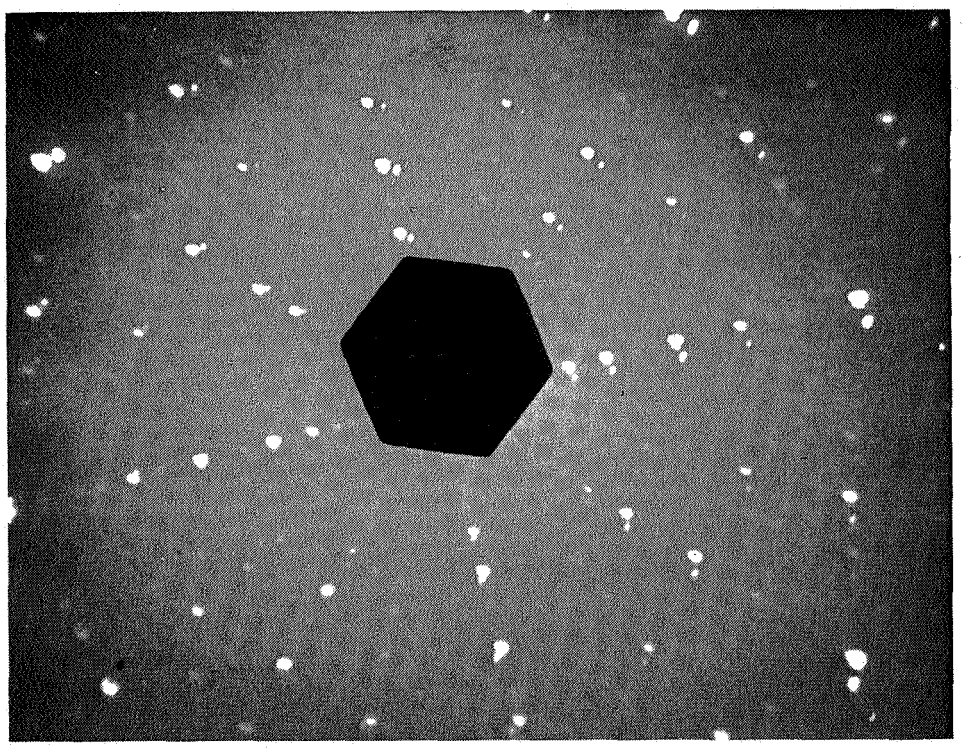

Fig. 53. The Laue diagram of the same tungsten crystal (see Fig. 52) confirms that not only the (110) surface was present. The doubled pattern indicates a slight misalignment of the single crystal prior to cutting.

Cesium ion surface lifetimes have been measured on the crystal face described above, in the temperature range between 1330 and 1061°K. Figure **54** shows a typical curve taken at 1206°K, with 0.2 msec/cm deflection and a preamplifier calibrated sensitivity of 5 mV/cm. The trace is written from the right to the left side. The ion Current increases to a maximum, at the moment of shutter close, and then decays exponentially. The average ion surface lifetime results from

$$I/I_o = 1/e \tag{38}$$

with an arbitrary point for I_o in the exponential decay curve.

Such curves, as represented by Fig. 54, are transferred onto semilog paper (Fig. 55) with the ordinate in percent of the amplitude and the abscissa the time base, The 1/e points from these curves yield the results shown in Fig. 56, with the average surface lifetime plotted versus the single crystal inverse temperature, From the slope of this plot the ion desorption energies are computed according to the Frenkel equation.

$$Q_i = (T/11600) \ln \frac{\tau}{\tau_o} \tag{39}$$

Here $Q_i = 1.827$ eV, with $\tau_o = 5.62 \times 10^{-12}$ sec.

If we consider that we have a tungsten surface with predominantly (100) orientation, the above ion desorption energy is in good agreement with data published earlier for the polycrystalline tungsten surface at low surface coverage,[19] From ionization studies it is well known that ionization preferentially takes place (for alkali deposition from the vapor phase) on the low work function patches, if $\phi - I \geq 0,6$ eV. The work function of the tungsten (100) facet is 5, 2 eV, according to Smith,[13] In contrast, Kuehl reports an ion desorption energy of 1.95 eV for the tungsten (110) surface.[58] However, this desorption energy was not

M 4613

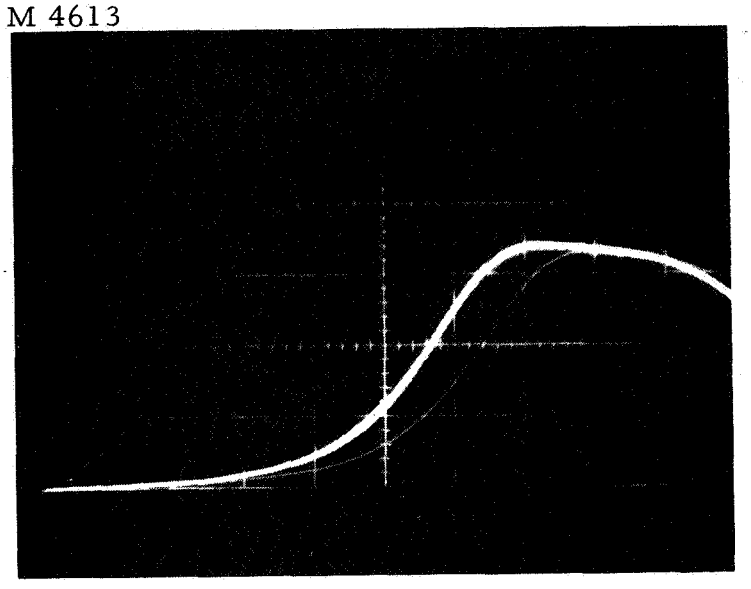

Fig. 54. As was shown in Fig. 51(a), the decay of the ion current is exponential as indicated in the scope trace (read from right to left). The shutter closes at the ion current density maximum.

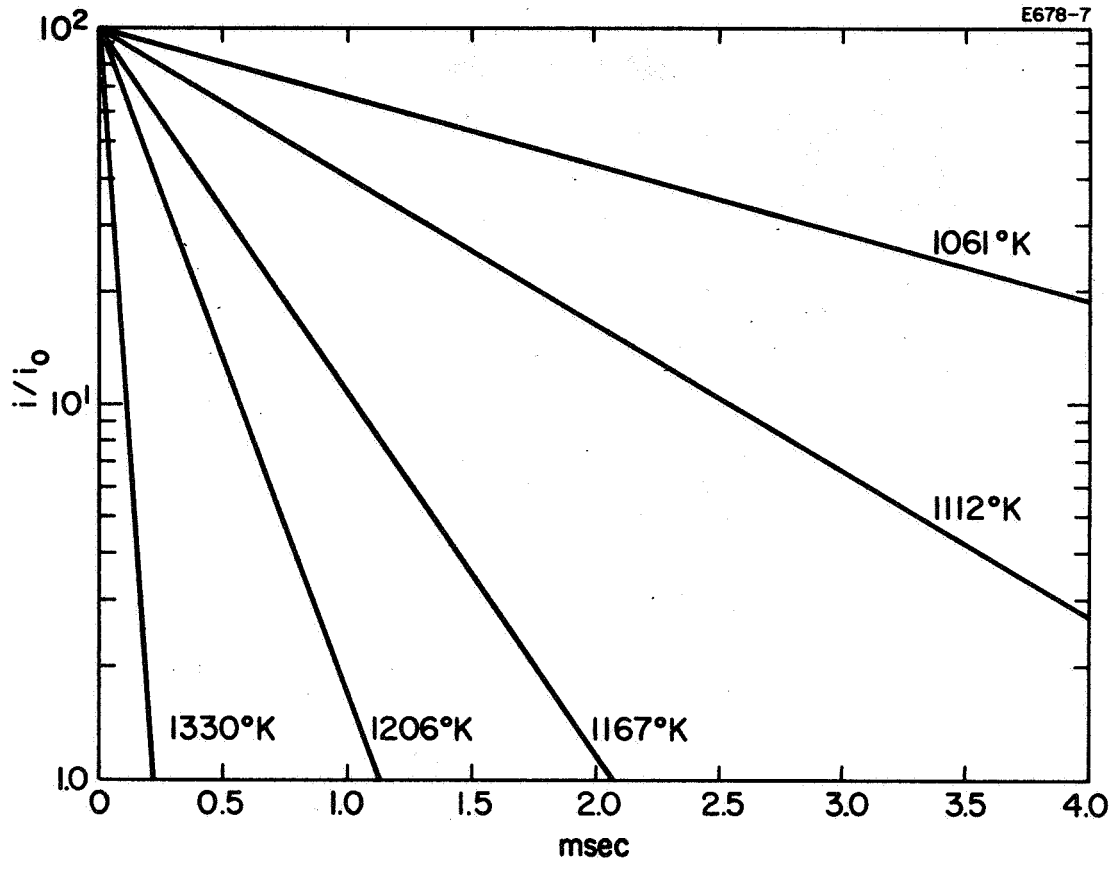

Fig. 55. The exponential decay of the scope traces shown, for example, in Fig. 54 are plotted here on semilog paper and confirm the strict exponential decay for a number of crystal temperatures. The average surface lifetime τ results from $i/i_o = 1/e$ with $e = 2.718$.

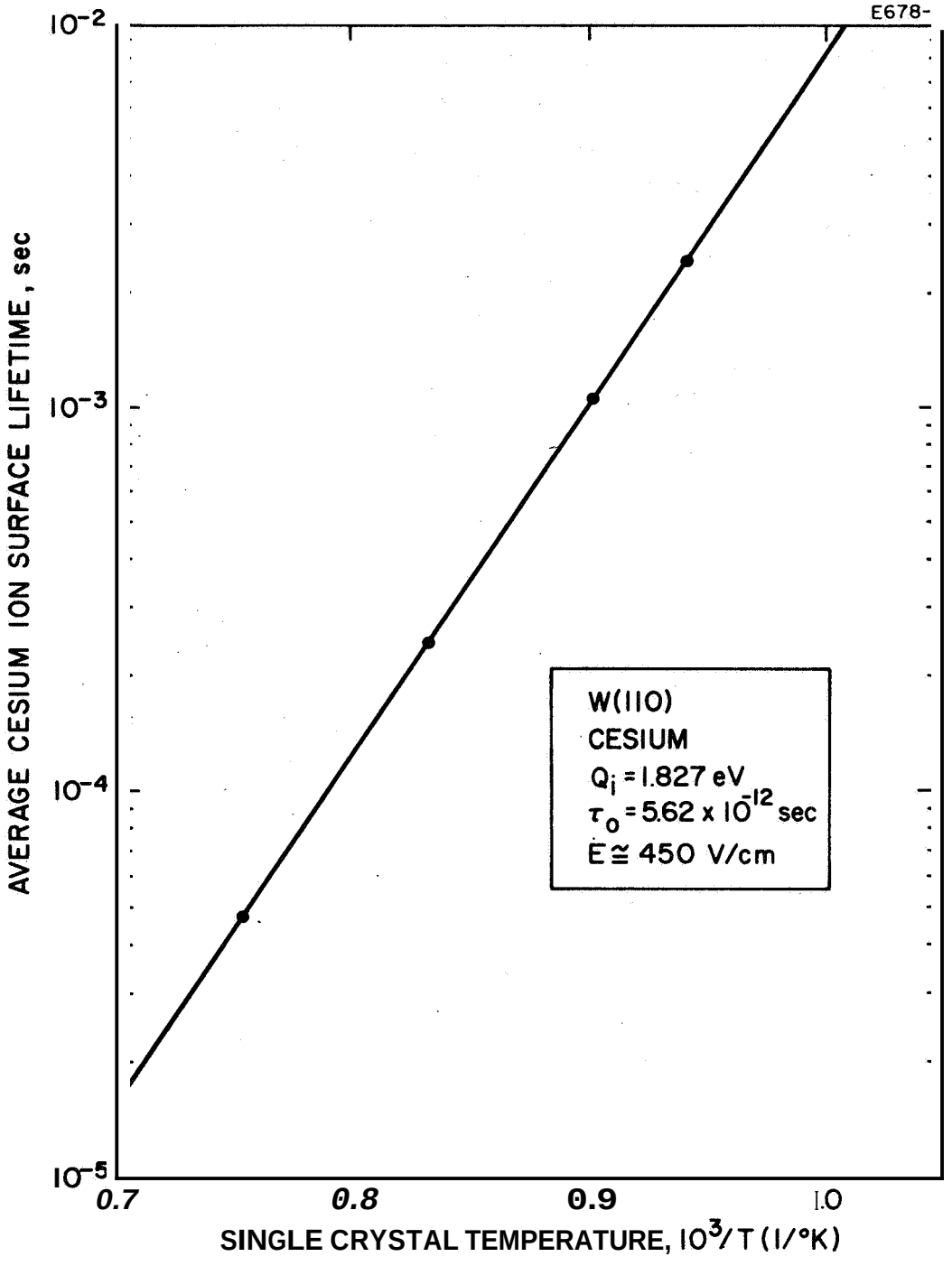

Fig. 56. The average surface lifetimes plotted versus the inverse crystal temperature. This plot yields the ion desorption energy (using the Frenkel equation) with Q_i = 1.827 eV for the composite surface under consideration (see Fig. 52).

measured directly, but was computed from the Schottky equation (see Appendix I). In a recent publication, Schmidt, et al.,[59] report for cesium on tungsten an ion desorption energy of 1.95 eV at about 3% coverage. The ion desorption energy minimum is 1.8 eV at surface coverage below 1%.[59]

SECTION VI

METAL VAPOR DEPOSITION ON POROUS TUNGSTEN

In one of our standard ultrahigh vacuum systems the evaporator was placed opposite the ion gun and constructed so that after evaporation the system operated as a Faraday cage for electron work function measurements. The metal to be deposited was wrapped around the evaporator tungsten filament.

Prior to the experiments the tube was evacuated according to our standard practice,[38] and the clean tungsten pellet work function first was established under vacuum in the low 8^{th} and 9^{th} scale, After all parts, especially the evaporator (mounted 1 in. away from the pellet surface to be coated), were outgassed, the evaporator was heated to a temperature which was high enough to evaporate the metal to be deposited.

The specific evaporation velocity a of the metal under consideration is expressed by

$$a = 5.85 \times 10^{-2} p_{Torr} (M/T)^{1/2} \text{ g cm}^{-2} \text{ sec}^{-1} \qquad (40)$$

with p the saturation pressure in Torr at T ^{o}K of the metal in the evaporator, M is the atomic mass number. The metal deposition on the emitter surface was measured by the change of its work function. When dipoles are deposited on a metal surface, the work function changes by

$$d\phi = 4\pi\sigma_m \theta M$$

with $\theta\sigma_m$ the number of dipoles per unit area and M the dipole moment. The work function increases if the adsorbed layer is negatively charged outward and decreases in the opposite case.

$$\phi = \phi_o - d\phi = \phi_o - 4\pi\sigma_m \theta M^*$$

During evaporation the pellet was kept at elevated temperature (but not so high that the deposited material re-evaporated). The metals under study were iron, nickel, rhenium, and iridium. Iron, nickel, and rhenium partially dissolve in tungsten.[60] Therefore, part of the deposited metal disappears by diffusion into the bulk of its substrate, as governed by the equation

$$C = (c_o/2)[\,1 - \text{erf}\, L/2\,(Dt)] \tag{41}$$

with c_o the original surface concentration. D is the volume diffusion coefficient and depends on the pellet temperature according to

$$D(T) = D_o \exp - Q_d/kT \tag{42}$$

with Q_d the diffusion activation energy. L is the distance from the surface. This equation may be applied for a solid solution. If a compound is formed, the diffusion mechanism is governed by the equation

$$C = c \left\{ 1 - \left(\frac{8}{\pi^2}\right) \exp\left[- \frac{\pi^2}{L^2} Dt \right| \right\} \tag{43}$$

In case of solid solution, the surface coverage follows from equilibrium condition with

$$\sigma_o\theta = \frac{3.5 \times 10^{22} p}{(TM)} - \frac{\sigma_o \theta \exp - Q_a/kT}{\tau_{ao}} - \frac{c_o}{2}\left[1 - \text{erf}\, \frac{L}{2Dt} \right|$$

p is in Torr, M in AMU, T in ^{o}K and Q_a is the atom desorption energy in eV. L is the diffusion penetration depth and σ_o the number of atoms per monolayer and unit surface area. c_o, the surface concentration constant is here equal to σ_o. With $\sigma_o = 5 \times 10^{14}$ atoms/cm^2, the above equation becomes

$$\theta = \frac{\frac{7.8 \times 10^{7} p}{(TM)^{1/2}} - \frac{1}{2}\left[1 - \operatorname{erf} \frac{L}{2Dt}\right]}{\left[1 + \frac{\exp - \frac{Q_a}{kT}}{\tau_{ao}}\right]} .$$

For its numerical evaluation we need to know the temperature dependence of the volume diffusion coefficient D(T), the penetration depth L(t), with t the time of diffusion and also the desorption energy Q_a.

Deposition of iron onto the emitter surface (using 99.99 iron) with an average arrival rate of 1.53×10^{13} atoms/cm^2-sec resulted in a decrease of the electron work function from 4.54 to 4.38 eV. The electron work function reported for β-Fe is 4.28 eV, with A = 26 A/deg^2 cm^2. That for γ-Fe is 4.23 eV, with A = 1.5 A/deg^2 cm^2 (Ref. 61). Figure 57 shows the increase of the electron emission after iron-deposition and the decrease of this current after stopping the iron evaporation, indicating the changeover, to the higher work function of tungsten. Emitter temperature is 1404^{o}K. Approximately 20 min after evaporation stopped, the clean tungsten surface was again established. The solid solubility of iron in tungsten is 0.8% by weight at 1640^{o}C, with little change of solubility with temperature.[62]

Deposition of nickel onto the porous tungsten substrate at 1350^{o}K resulted in an increase of the emitter work function by 0.1 to 0.2 eV, as measured immediately after deposition. The nickel vapor pressure at 1350^{o}K is 7×10^{-4} Torr, and the nickel evaporation at this temperature is 8.56×10^{-6} g/cm^2-sec if the entire emitter surface is covered with nickel. The slightly increased work function was observed for only a

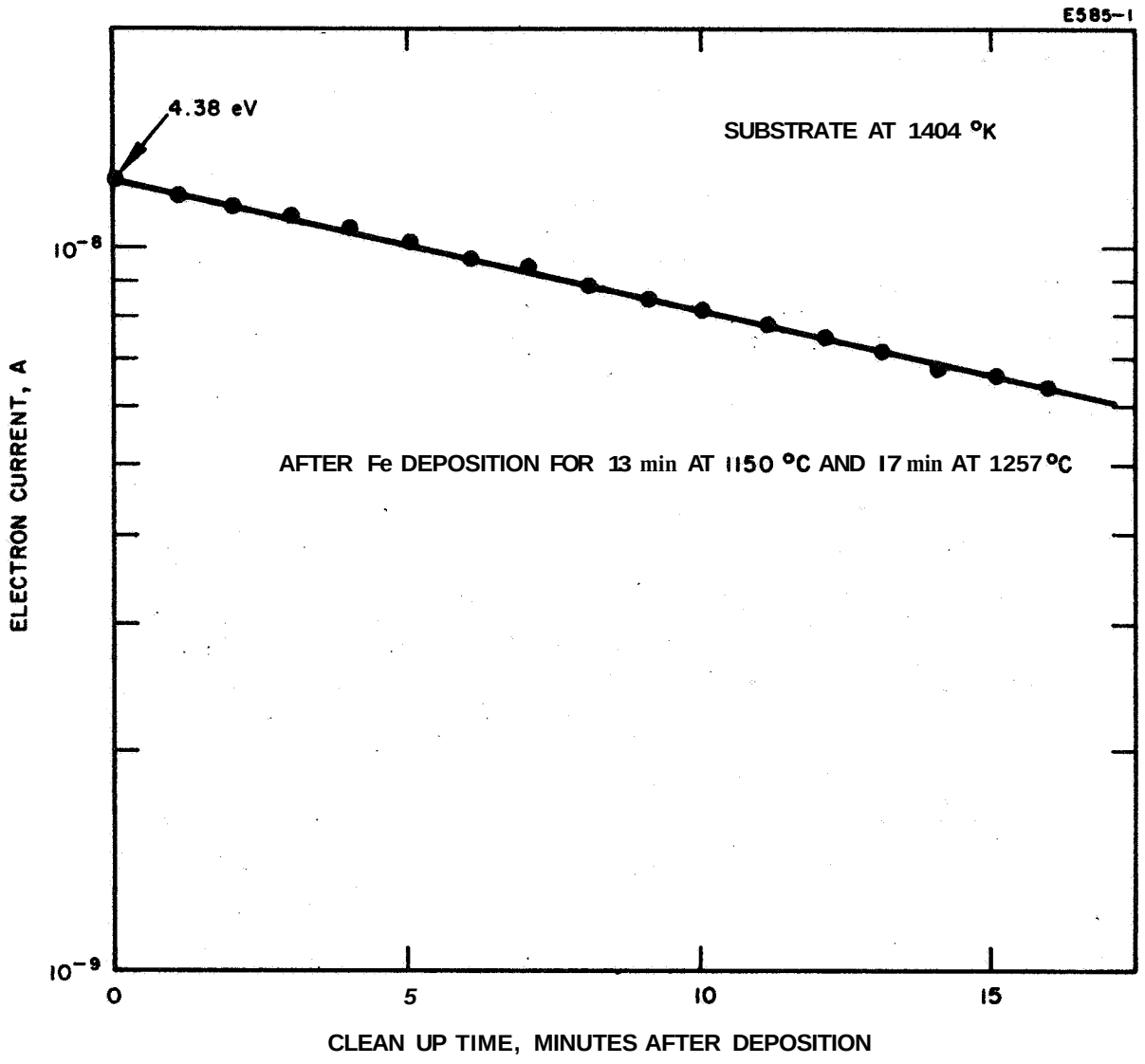

Fig. 57. Electron emission change after stopping deposition of iron onto a tungsten emitter surface. After about 15 min, the original surface conditions prior to deposition are regained.

short time after evaporation stopped. The electron emission then indicated the changeover to that of polycrystalline tungsten. The solid solubility of nickel in tungsten is 0,3 wt% at 1495°C.[60]

The first deposition of rhenium on the same tungsten pellet (Mod E from Philips Metalonics) yielded no change in the emitter work function, It is possible that the evaporator temperature was not high enough. After an improved evaporator had been installed, repeated deposition of rhenium onto porous tungsten yielded a slightly lower work function than that of clean tungsten. In all cases the difference was close to 0, 1 eV, and it disappeared shortly after evaporation stopped. The solid solubility of rhenium in tungsten is as high as 26 wt% at 1600°C (Ref. 60).

A high purity iridium filament was purchased, but deposition experiments could not be completed during the contract period.

It must be emphasized that these experiments do not necessarily reveal the long term behavior of these deposits, except for the tungsten rhenium alloys. Furthermore, as indicated by the rhenium deposit, oriented deposition must be considered as a means of controlling the work function.

APPENDIX I

The Schottky equation is

$$Q_a - Q_i = e(\phi - I) - dQ \qquad (I\text{-}1)$$

with Q_a the atom and Q_i the ion desorption energy. ϕ is the work function and I the ionization potential, Combining the Saha and the Frenkel equation, we come to a similar appearing result,

$$\frac{\nu_i}{\nu_a} = \frac{1}{2} \exp \frac{e(\phi - I)}{kT}$$

$$\tau_i = \text{I-io} \exp \frac{Q_i}{kT}$$

$$\nu_i = \frac{\sigma_o \theta A}{\tau_i}$$

$$\frac{\nu_i}{\nu_a} = \frac{\tau_a}{\tau_i} = \frac{\tau_{ao}}{\tau_{io}} \exp \frac{e}{kT} (Q_a - Q_i) \qquad (I\text{-}2)$$

and

$$Q_a - Q_i = e(\phi - I) - \frac{kT}{e} \ell n \frac{2\tau_{ao}}{\tau_{io}} \qquad (I\text{-}3)$$

The ionization activation energy is

$$dQ = (kT/e) \ell n \frac{2\tau_{ao}}{\tau_{io}} \qquad (I\text{-}4)$$

θ is the surface coverage relative to a monolayer, σ_o the number of atoms per monolayer and unit area, ν_a and ν_i the atom and ion evaporation frequencies, and τ_{ao} and τ_{io} the surface vibration constants for the atoms and ions.

APPENDIX II

Thermal neutrals registered by the neutral detector (ND) are

$$N = n_o A^* A/R^2\pi \text{ atoms per sec} \qquad \text{(II-1)}$$

with n_o the neutral efflux from the emitter (in atoms per cm^2 sec), A^* the emitter surface area (in cm^2), **A** the neutral detector collimator cross section (in cm^2), and R the distance (in cm) between the emitter and the ND anode, Cosine distribution of the emitted neutrals is assumed here, and has been confirmed by neutral effluxmeasurements.

The number of charge exchange neutrals per second n registered by the ND is

$$n = n_o A^* \bar{j} A \xi L/v (L/3)^2 e\pi \qquad \text{(II-2)}$$

with L the interaction length between atoms and ions (in cm), v the thermal velocity of the neutrals evaporated from the emitter, $\bar{j}$ the average ion current density in the interaction volume with

$$\bar{j} = i/\bar{F} \text{ and } \bar{F} = (1/F_2 - F_1) \int_{F_2}^{F_1} F\, dF = 1.37 \text{ cm}^2$$

if 90% of the interaction is considered, The ion beam expansion due to its space charge is

$$r_2/r_1 = (4.1 \times 10^6 M^{1/2} j L^2/U^{3/2})^{1/2} \qquad \text{(11-3)}$$

with r_1 and r_2 the ion beam radii, M the atomic mass number, j the ion current density (in amps/cm^2), e = 1.6×10^{-19} C, and U the accel

potential (in volts).[45] Because the DeBroglie wavelength $\lambda = h/m\,v$ of cesium is much smaller than the dimension of the scattering body, small angle scattering is predominant.[63] The differential charge exchange cross section σ (in cm^2) depends strongly on the scattering angle θ. Only those neutrals which are scattered into an angle of $\gamma = 1.9 \times 10^{-2}$ deg pass the collimator. If we approximate σ by the error function, we have

$$\sigma(\theta) = \sigma_o \exp(-\theta^2) \qquad \text{(II-4)}$$

where $\sigma_o = 2.35 \times 10^{-14}$ cm^2 at 5 kV and zero deflection angle.

Then ξ becomes

$$\xi = \int_o^{\gamma} 2\pi\,\sigma(\theta)\,\sin\theta\,d\theta \qquad \text{(II-5)}$$

and for small angle

$$\xi = 2\pi\,\sigma_o \int_o^{\gamma} \theta \exp(-\theta^2)\,d\theta\ .$$

Since

$$\theta \exp(-\theta^2) = \theta - \theta^3 + \frac{\theta^5}{2!} \ldots,$$

we have

$$\xi = \pi \sigma_o \gamma^2 \qquad \text{(II-6)}$$

and then

$$n = n_o A^* \bar{j}\, A L \sigma_o \gamma 2/v\,(L/3)2\,e. \qquad \text{(11-7)}$$

Considering a cesium ion current density of 10 mA/cm^2 and a neutral efflux of 4% (tungsten pellet with 10^6 pores/cm^2 by the line intercept

method), the contribution of the charge exchange neutrals to the neutral detector reading is less than 1%. Therefore, if the neutral detector reads 4% neutral flux, more than 3. 97% of these neutrals are evaporated from the emitter,

APPENDIX III

Cesium evaporation from oppositely located electrode structures onto the ion emitter contributes to the neutral emission when there is no ion extraction potential at the accel electrode and, on the other hand, under saturation conditions adds to the ion current. Consequently neutral efflux data reported here are slightly below their actual value, compared with the neutral efflux without ion extraction. Charge exchange neutrals slightly increase the neutral efflux reading, partially compensating for above loss[39] (see Appendix II).

Surface roughness leads to an overestimation of the current density. With regard to (for example) electron emission, the actual electron current density from a rough surface is lower than that from a highly polished surface. This lower current density corresponds to a higher thermionic work function. A work function increase on polycrystalline tungsten between 0.09 and 0.12 eV results from a current density reduction by a factor of two, Under the assumption of an average 1 μ pore radius and 1 μ pore depth, the increase in surface area on 20% porosity tungsten corresponds to a thermionic work function increase on the order of 0.03 eV.

REFERENCES

1. O. K. Husmann, **AIAA** J. 1, 2607 (1963).

2. H. W. Hayden and J. H. Brophy, J. Less-Common Metals 6, 214 (1964).

3. B. Ch. Dyubua, €3. N. Popov, and M. A. Tylkina, Radio Eng. Electron. Phys. 7, 1463-1470 (1962).

4. D. L. Goldwater and W. E. Danforth, Phys. Rev. 103, 871 (1956).

5. E, F. Chaikovskii and G. M. Pyatigorskii, Soviet Phys. – Tech. Phys. 9, 847 (1964).

6. D. L. Keller, B. M. I. , private communication, September 8, 1965.

7. R. V. Culver and F. C. Tompkins, Advances in Catalysis (Academic Press, New York, 1959)) Vol. XI, pp. 68-128.

8. E. Ya. Zandberg and N. I. Ionov, Soviet Phys. – Usp. 17, 255 (1959).

9. L. N. Dobretsov, NASA TT F-73.

10. J. B. Taylor and I. Langmuir, Phys. Rev. 44, 423 (1933).

11. W. B. Nottingham, paper presented at Fourth International Conference on Ionization Effects in Gases, Upsala, Sweden, August 1959.

12. E. Ya. Zandberg, V. I, Paleev, and A, Ya. Tontegode, Soviet Phys. — Tech. Phys. 7, 147 (1962).

13. G. F. Smith, Phys. Rev. 94, 295 (1954).

14. N. H. Nichols, Phys. Rev. 78, 158 (1950).

15. J. Anderson, W. E. Danforth, and A. J. Williams, J. Appl. Phys. 34, 2260 (1963).

16. E. Ya. Zandberg and A. Ya. Tontegode, Soviet Phys. – Tech. Phys. 10, 260 (1965).

17. Yu. Ya. Staviskii and S. Ya. Lebedev, Soviet Phys, – Tech. Phys. 8, 1094 (1963).

18. B. Ch. Dyubua and L. A. Ermolaev, Bull. Acad. Sci. USSR, Phys. Ser. 28, 1407 (1964).

19. O. K. Husmann, Phys. Rev, 140, A546 (1965).

20. J. D. Levine and E. A. Gyftopoulos, Surface Sci. 1, 171 (1964) and 1, 225 (1964).

21. N. S. Razor and C. Warner, J. Appl. Phys. 35, 2589 (1964).

22. H. L. Garvin and R. G. Wilson, AIAA J. 3, 1867 (1965).

23. H. S. Goldshmidt and J. A, Brand, Air Force Contract AF 61(052)-306, 1959 to 1961,

24. M. R. Andrews, J. Phys. Chem. 27, 270 (1923).

25. C. W. Horsting, J. Appl. Phys. 18, 95 (1947).

26. O. K. Husmann, D. M. Jamba, and D. R. Denison, AIAA J. 4, 273 (1966).

27. S. A. Becker, E. J. Becker, and R. G. Brandes, J. Appl. Phys. 32, 411 (1961).

28. A. E. Van Arkel, Reine Metalle, Berlin, 1939.

29. H. Moissan, Gompt. Rend. 142, 189 (1906).

30. R. P. Johnson, Phys. Rev. 54, 459 (1938); see also D. O. Boyle, J. Appl. Phys. 36, 2849 (1965).

31. M. H. Nichols, Phys. Rev. 57, 297 (1940).

32. E. B. Hensley, J. Appl. Phys. 32, 301 (1961); see also I. G. Potter, Phys. Rev, 58, 623 (1940).

33. G. M. Pyatigorskii, Soviet Phys. — Tech. Phys. 9, 1117 (1965); see also L. N. Dobretsov, Soviet Phys. — Tech. Phys. 10, 416 (1965).

34. R. M. Sternheimer, Phys. Rev. 115 1198 (1959); see also J. E. Chamberlain and J. C. Zorn, Phys. Rev. 129, 677 (1963).

35. E. Ya. Zandberg, Bull, Acad. Sei. USSR, Phys. Ser. 24, 639 (1960).

36. Handbook of Chemistry and Physics, 40th ed. (Chemical Rubber Publishing Co., 1958/59).

37. R. W. Ditchburn and J. C. Gilmour, Rev. Mod. Phys. 13, 310 (1941).

37a. P. M. Waters, Phys. Rev. 109, 1466 (1958).

37b. R. Bruenne, Z. Phys. 147, 165 (1957).

37c. M. Kaminsky, in Struktur und Eigenschaften der Materie (Academic Press, New York, 1965), Yol. 25.

37d. J. G. Anderson, J. Appl. Phys. 33, 2017 (1962).

37e. R. V. Stuart and G. N. Wehner, J. Appl. Phys, 33, 2845 (1962).

38. O. K. Husmann in Progress in Astronautics and Aeronautics (Academic Press, New York, 1963), Vol. 9, p. 195.

39. O. K. Husmann and R. Turk, AIAA J. 3, 1653 (1965).

40a. D. F. Hall, A. Y. Cho, and H. Shelton, AIAA Preprint 66-218,

40b. B. Thompson, G. Kuskevics, and M. LaChance, AIAA Preprint 66-219.

41. O. K. Husmann in Progress in Astronautics and Aeronautics (Academic Press, New York, 1961), Vol. 5, p. 505.

42. R. Turk, "Tungsten Ionizers with Controlled Porosity for Cesium Ion Engines," Preprint No. 418, International Powder Metallurgy Conference, New York, 1965,

42a. O. K. Husmann, Contract NAS 3-4110, Final Report, November 1964.

43. A. Recknagel, Z. Phys. 117, 687 (1941) and 120, 331 (1942).

44. G. Popp and W. Walcher, Ann. Phys. 20, 293 (1957).

45. M. von Ardenne, Tabellen zur Angewdt. Physik (VEB Deutscher Verlag der Wissenchaften, Berlin, 1962), Vol. I.

46. O. Bruche and A. Recknagel, Electronengeraete (Springer, Berlin, 1941), p. 256.

47. W. Mecklenburg, Z. Phys. 120, 21 (1942/43); see also E. G. Ramberg, J. Appl. Phys, 13, 582 (1942) and 20, 183 (1949); H. Mahl, Z. Phys. 108, 771 (1938); H. Johannson, Ann. Phys. 21, 274 (1934); J. O. Archard, Brit. J. Appl, Phys. 8, 127 (1957).

48. W. Lippert and W. Pohlit, Optik 9, 456 (1952) and 10, 447 (1953) and 11, 181 (1954); see also J. O. Archard, Brit, J. Appl. Phys. 7, 320 (1949); Heise-Range, Optik 5, 201 (1949).

49. W, Glaser and P. Schiske, Optik 11, 422 (1954) and 12, 233 (1955).

50. R. Berisch in Ergebnisse der Exakten Naturwissenschaften (Springer, Berlin, 1964), Vol. 35, pp. 297-422; see also M. Kaminsky in Struktur und Eigenschaften der Materie (Academic Press, New York, 1965), Vol. 25.

51. E. Espe, Wekrstoffe der Hochvacuum Technik, Vol. III. Hilfswerkstoffe (VEB Deutscher Verlag der Wissenschaften, Berlin, 1961), p. 57.

52. G. Moellenstedt and W. Hubig, Optik 15, 538 (1958).

53. D. G. Brandon, S. Ranganathan, and D. S. Whitmell, Brit. J. Appl. Phys. 15, 55 (1964).

54. G. V. Spivak, I. A. Pryamkova, and N. N. Sedov, Bull. Acad. Sci. USSR, Phys. Ser. 24, 648 (1960).

55. L. A. DuBridge and W. W. Roehr, Phys. Rev. 42, 52 (1932); see also S. Dushman, H. N. Rove, J. Ewald, and C. A. Kidner, Phys. Rev. 25, 388 (1925).

56. S. B. L. Mathur, Nat. Lnst. Sci. India 19, 153 (1,953).

56a. B. J. Hopkins and K. R. Pender, Brit, J. Appl. Phys, 17, 281 (1966).

56b. G. Popp, Ann. Phys. 13, 115 (1964).

57. J. A. Becker, Phys. Rev. 28, 341 (1926).

58. W. Kuehl, Thesis, Hamburg, 1954.

59. L. D. Schmidt and R. Gomer, J. Chem. Phys. 43, 2055 (1965); see also M. Kaminsky, Bull. Am. Phys, Soc. 10, 432 (1965); M. D. Scheer and J. Fine, J. Chem, Phys. 37, 2407 (1962).

60. J. J. English, DMIC Report 152, April 28, 1961; and DMIC Report 183, February 7, 1963.

61. H. B. Wahlin, Phys. Rev. 61, 509 (1942); see also G. Siljeholm, Ann. Phys. 10, 178 (1931).

62. H. Arnfelt, "Constitution of the Iron-Tungsten and Iron-Molybdenum Alloys," Iron-Steel Institute, London Carnegie School Memo. 17. 1, March 1928.

63. H. S. W. Massey and C. B, O. Mohr, Proc. Roy, Soc. (London) 141A, 434 (1933).

ACKNOWLEDGMENT

The author wishes to thank H. Childs, D. Lockwood, and F. Kavanagh of the NASA Lewis Research Center, Cleveland, Ohio, for their continuous interest and support of this work.

Thanks are extended to D. M, Jamba for his cooperation and interest in the ion microscope development and his careful measurements with it, to R. Turk for pressing and sintering the tungsten-25% rhenium pellet, and to W. McKee for chemically coating two porous substrates with thin layers of rhenium and iridium. Thanks are also extended to John Mullane for his technical work.

DISTRIBUTION LIST

Contract NAS3-6270

NUMBER OF COPIES

National Aeronautics and Space Administration
Washington, D. C. 20546
Attention: RNT/James Lazar 1
RNT/J. Mullin 1

National Aeronautics and Space Administration
Lewis Research Center
21000 Brookpark Road
Cleveland, Ohio 44135
Attention: Spacecraft Technology Procurement Section, MS 54-2 1
Technology Utilization Office, MS 3-19 1
Technical Information Division, MS 5-5 1
Library, MS 60-3 2
Spacecraft Technology Division, MS 54-1
S. Jones 1
C. C. Conger 1
H. R. Hunzak 1
R. R. Nicholls 6
Electromagnetic Propulsion Division, MS 301-1
W. Moeckel 1
H. R. Kaufman 1
E. A. Richley 1
Report Control Office, MS 5-5 1

National Aeronautics and Space Administration
Scientific and Technical Information Facility
P.O. Box 33
College Park, Maryland 20740
Attention: NASA Representative RQT-2448 6

National Aeronautics and Space Administration
Marshall Space Flight Center
Huntsville, Alabama 35812
Attention: Ernest Stuhlinger (M-RP-DIR) 1

	NUMBER OF COPIES NAS3-6270
Research and Technology Division Wright-Patterson AFB, Ohio 45433 Attention: AFAPL (APIE) Major P. E. Peko	2
AFWL Kirtland AFB, New Mexico 87417 Attention: WLPC/Captain C. F. Ellis	1
Aerospace Corporation P. O. Box 95085 Los Angeles, California 90045 Attention: Library/Technical Documents Group	1
Jet Propulsion Laboratory 4800 Oak Grove Drive Pasadena, California 91103 Attention: D. Kerrisk Technical Library	2 1
Electro-Optical Systems, Inc. 300 North Halstead Pasadena, California 91107 Attention: R. C. Speiser	2
TRW Inc. TRW Systems One Space Park Redondo Beach, California, 90278 Attention: D. B. Langmuir E. Cohen	1 1
General Electric Space Flight Propulsion Laboratory Cincinnati, Ohio 45215 Attention: M. L. Bromberg	1
Field Emission Corporation 611 Third Street McMinnville, Oregon 97128 Attention: L. W. Swanson	1
Litton Industries Surface Physics Department Minneapolis, Minnesota Attention: G. K. Wehner	1

	NUMBER OF COPIES NAS3-6270
Varian Associates 611 Hansen Way Palo Alto, California 94304 Attention: Technical Library	1
Battelle Memorial Institute 505 King Avenue Columbus, Ohio 43201 Attention: J. Anno	1
National Aeronautics and Space Administration Ames Research Center Moffett Field, California 94035 Attention: Library	1
Astro Met Associates, Inc. 500 Glendale-Milford Road Cincinnati, Ohio 45215 Attention: J. W. Graham	1
University of California Space Science Laboratory Berkeley, California 94720 Attention: H. P. Smith	1
National Aeronautics and Space Administration Langley Research Center Langley Field Station Hampton, Virginia 23365 Attention: Technical Library	1
Colorado State University Fort Collins, Colorado 80521 Attention: L. Baldwin W. Mickelsen	1 1
U. S. Atomic Energy Commission P.O. Box 62 Oak Ridge, Tennessee 37831 Attention: Technical Information Service Extension	1
Republic Aviation Corporation Plasma Propulsion Laboratory Farmingdale, Long Island, New York 11735 Attention: A. Kunen	1

	NUMBER OF COPIES NAS3-6270
United States Air Force Office of Scientific Research Washington, D. C. 20025 Attention: M. Slawsky	1
Case Institute of Technology 10900 Euclid Avenue Cleveland, Ohio 44106 Attention: Eli Reshotko	1
University of California Lawrence Radiation Laboratory Livermore, California Attention: S. A. Colgate	1
University of Illinois Department of Electrical Engineering Urbana, Illinois 61801 Attention: L. Goldstein A. Chou	1 1
University of Washington Department of Electrical Engineering Seattle, Washington 98105 Attention: H. Golde	1
Rome Air Development Center Headquarters – Air Force Systems Command Griffiss AFB, New York 13442 Attention: RALTP	1
Swiss Federal Institute of Technology Zurich, Switzerland Attention: Library	1
Cornell Aeronautical Lab., Inc. Buffalo, New York 14221 Attention: Prof. A. S. Gilmour, Jr. D. Lockwood	1 1
National Aeronautics and Space Administration Goddard Space Flight Center Greenbelt, Maryland 20771 Attention: William Isley, Code 734	1

NUMBER OF **COPIES**

NAS3-6270

NASA Western Operations
150 Pico Boulevard
Santa Monica, California 90406
Attention: Francis A. DiLorenzo — 1

J. T. Kotnik
16808 Westdale Avenue
Cleveland, Ohio 44135 — 1